Graphene Plasmons in Optically Forged Structure

Master's thesis

University of Jyväskylä

Department of Chemistry

09.12.2019

Suvi-Tuuli Akkanen

Abstract

The goal of this thesis is to use the sub-wavelength features of optically forged blister structures to overcome the large mismatch between the wave vector of the incident light and the wave vector of graphene plasmons. Optical forging is a method where 3D patterns can be irradiated into 2D materials via ultra-short laser pulse introduced strain, which the material tries to overcome by bending, stretching bonds and creating point defects in the structure. Even though these optically forged structures in graphene have point defects, their overall structure is still graphene and thus they should exhibit largely the same electrical properties and be able to support GSPs. Larger structures that resemble graphene nanoribbons were also forged and tested for plasmonic resonances. The plasmon measurements were done with FTIR microscope as plasmons change the light absorption. Possible GSPs were expected to be in the FIR or THz range. As no change in the IR response was detected between unpatterned and patterned areas despite multiple attempts with different structures and parameters, it could be that optically forged structures are not enough to overcome the wavevector mismatch and allow excitation of plasmons in graphene. The plasmons could also be further in the THz region and thus not visible in the measurements or the FTIR laser signal could have been insufficient for any plasmonic response to be detectable. To overrule these possible sources of error, larger structures which allow larger apertures and thus better signal for measurements, or SNOM with sufficient measurement range could be used to perform similar experiments.

Tiivistelmä

Grafeenin plasmoneiden aikaansaamiseksi täytyy jollakin tavoin poistaa virittävän valon fotonien liikemäärän ja grafeenin plasmoneiden aaltovektorin liikemäärän välinen suuri ero. Tämän tutkielman tarkoituksena oli saada aikaan grafeenin plasmoneita hyödyntämällä optisella taonnalla tehtyjen rengasrakenteiden aallonpituutta pienempiä piirteitä, joiden pitäisi teoreettisesti ratkaista tämä liikemääräongelma. Optisella taonnalla voidaan muodostaa 3D kuvioita 2D materiaaliin käyttäen hyväksi ultranopeiden laserpulssien aiheuttamaa jännitettä 2D materiaalin rakenteessa. 2D materiaali pyrkii purkamaan tätä jännitettä venyttämällä ja taivuttamalla sidoksiaan ja muodostamalla pistemäisiä hilavirheitä rakenteeseensa, muodostaen 3D rakenteet. Vaikka optisen taonnan taustalla onkin osittain pistemäisten virheiden muodostuminen materiaalin hilaan, ovat materiaalin tyypilliset rakenteet silti hallitsevia ja säilyttävät materiaalin, tässä tapauksessa grafeenin, elektroniset ominaisuudet. Lisäksi suurempia, nanokaistaleita muistuttavia hilarakenteita kuvioitiin optisella taonnalla grafeeniin, sillä nanokaistaleiden tutkimuksissa on aiemmin onnistuttu havaitsemaan plasmoneita samanlaisin mittausmenetelmin, kuin mitä tässä työssä hyödynnetään. Plasmoneita yritettiin havaita mittaamalla kuvioiduista alueista infrapuna-absorption muutoksia, sillä plasmoneiden oletettiin olevan kaukoinfrapuna- tai terahertsi- alueella. Koska infrapuna-absorptiossa ei havaittu muutoksia, vaikka erilaisia rakenteita ja mittauksia yritettiin, johtopäätöksenä esitetään, etteivät optisesti taotut kuviot ole välttämättä riittäviä liikemääräeron poistamiseen ja täten plasmonien synnyn mahdollistamiseen. On myös mahdollista ettei plasmoneita havaittu, koska ne olivat kauempana terahertsi- alueella kuin mihin laitteen mittausalue yltää, tai laitteen infrapunalähteen signaali näytteestä ei ollut riittävä havaitsemaan plasmonien aiheuttamia muutoksia absorptiossa. Varmistuksen tämän tutkielman tulokselle voisi saada sulkemalla edellä mainitut tekijät pois esimerkiksi mittaamalla samoja asioita asian mukaisen aallonpituusalueen omaavan SNOM:in avulla tai kuvioimalla entistä suurempia optisesti taottuja alueita, jolloin FTIR mittausten signaalia saataisiin parannettua.

Preface

This Master's thesis in its full extent was conducted between May 2019 and December 2019 at the Nanoscience Center for the Department of Chemistry of University of Jyväskylä.

I would like to thank Mika Pettersson for allowing me to continue working on this interesting topic from my Bachelor's thesis to my Master's and for providing motivation and inspiration during the whole process. I would like to thank Kamila Mentel, Pasi Myllyperkiö and Vesa-Matti Hiltunen for using time in their busy schedules to provide me with samples and guidance. Gold nanoparticles used in this work were provided graciously by Ville Saarnio.

I am grateful for the company and reflection that my friend and colleague Johannes Parikka offered me as we shared an office during summer and for all the cheering received and discussions had with Henri Kaaripuro. My gratitude goes to my friend Arttu Lehikoinen, for acting as my peer pressure during the final weeks of writing this thesis. I would like to thank all my friends individually, but as there needs to be some pages left for the actual matter at hand here is a collective thank you! You have kept me sane and helped me relax in my free-time so my time at the university and all the studying has felt like a luxury rather than a chore.

Finally, I would also like to thank my mother for providing me support and encouragement throughout my life, and my father for pushing me to do my best and to be willing to take risks. And to my dear Mikael: Thank you for keeping me grounded and giving me endless support. Your work ethics and professionalism make me strive to be better myself.

Jyväskylä, December 2019

Suvi-Tuuli Akkanen

Contents

Abbreviations

FIR – Far Infrared

THZ - Terahertz

CVD – Chemical Vapor Deposition

OM – Optical Microscopy

AFM – Atomic force microscopy

STM – Scanning tunneling microscopy

GO – Oxidized graphene

SPs – Surface plasmon

SPPs – Surface plasmon polariton

LSPRs – Localized surface plasmon resonances

GSPs – Graphene Surface Plasmons

GNP – Gold Nanoparticle

FTIR – Fourier Transform Infrared

PMMA – Polymethyl Methacrylate

EM – Electro Magnetic

SERS – Surface Enhanced Raman Spectroscopy

SEIRA – Surface Enhanced Infrared Absorption

ICPMS - Inductively coupled plasma mass spectrometry

EELS - Electron energy loss spectroscopy

THEORY

1 Graphene

All life on earth is based on carbon so it is no wonder that its allotropes have a bunch of interesting, even record breaking, properties for all sorts of applications. The best-known allotropes of carbon are diamond and graphite. Diamond consists of carbon atoms covalently bonding to other carbon atoms with all four of its electrons and it is the hardest known material in the world.[1] Graphite carbons are bonding covalently to three other carbon atoms, in plane forming a sheet, and to another sheet with its last electron. The last electron also participates in the sheet formation via weak interactions caused by a delocalized pi-orbital it forms with other electrons that do not participate in the covalent sheet bonds. The sheets stack in ABCABC formation so that every fourth sheet is similar to the first.[2] One of the more interesting carbon allotropes is Buckminsterfullerene or "Buckyball", the football-like spherical compound that consists of sixty graphene atoms. Buckminsterfullerene's neutral form was found in space in 2010 and its ion 2015. It has not been found on earth.[3] Another allotrope that has recently interested many researchers is carbon nanotubes. The carbon nanotubes consist of single layer graphite, which is another carbon allotrope called graphene, forming a tube. Carbon nanotubes are very light, strong and have high thermal conductivity. They have the highest tensile strength of any material.[1] Carbon nanotubes share many of their advantageous properties with graphene, which exhibits phenomenal tunable electrical and optical properties. Graphene can be created simply by peeling graphite with ordinary tape as Konstantin Novoselov and Andre Geim first showed in 2004. They received a Nobel Prize for their work in advancing the knowledge in graphene in 2010.[4] Just like many other allotropes of carbon, graphene is also front runner in one mechanical property as graphene is the strongest material known to man.[5]

1.1 Structure and mechanical properties

As mentioned before, graphene is an allotrope of carbon and can be thought as a single layer of graphite. It is structured in a hexagonal pattern, where each carbon atom forms three σ-bonds with other carbon atoms in the structure. Carbon has four valence electrons and one of them does not take part in forming these covalent σ-bonds. The $2s$, $2p_x$ and $2p_y$

form a sp^2-orbital and these orbitals neighbouring carbon's corresponding orbital and form the in-plane σ-bond. The length of these bonds (a_0) is 1.42 Å and the bond angle is 120°. $2p_z$ orbital is left unbound and it forms π-bond with the neighbouring atom's $2p_z$ orbital. The π-bonds also form double bonds in graphene structure and these π-bonds hybridize together, forming delocalized π-bands on both sides of the sheet, perpendicular to the σ-bonds, essentially forming valence (π) and conducting (π^*) bands.[6]

The mechanical properties of graphene stem from the in-plane σ-bonds. Although single-layer graphene is only one atom thick sheet, it is incredibly strong and elastic. Graphene has the Young Modulus of around 1.0 TPa and ultimate tensile strength of 130 GPa, whereas steel has the Young modulus and ultimate tensile strength respectively around 200 GPa and 400-550 MPa, making graphene mind-bogglingly at least 400 times stronger than steel.[5,7,8]

The geometrical structure can also be a factor when determining the material's conducting properties and for graphene it makes explaining the electrical and thermal properties a lot easier. The unit cell of graphene consists of two carbon atoms that can be thought to be of different types *A* and *B*. The carbons are, of course, indistinguishable but they can be considered to form two dissimilar triangular sublattices that differ from one another on the orientation of the bonds. The lattice vectors, $\overline{a_1}$ and $\overline{a_2}$, of graphene lattice reach from one type A or B to the other similar atoms in the hexagonal structure.[9] This is illustrated in Figure 1 and the lattice vectors in respect of the bond length a_0 are presented in equation 1[10,11]. Also pictured in the Figure 1 is the Brillouin zone of graphene.

$$\overline{a_1} = \frac{a_0}{2}\left(3, \sqrt{3}\right),\ \overline{a_2} = \frac{a_0}{2}\left(3, -\sqrt{3}\right),\ a = \sqrt{3}a_0. \qquad (1)$$

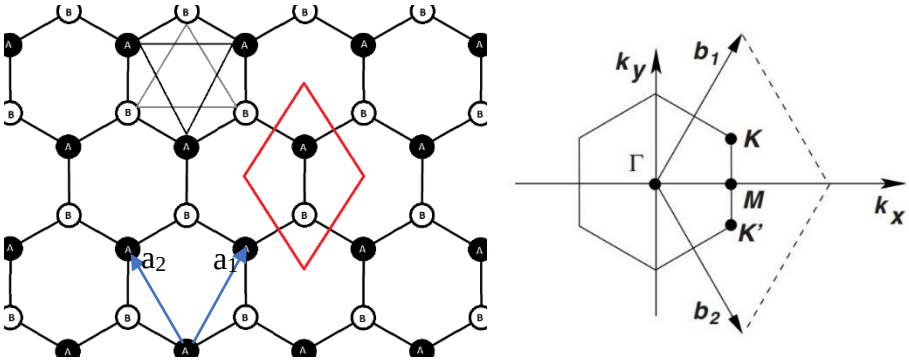

Figure 1. Left: Structure of graphene. The unit cell can be seen inside the rhombus and the sublattices are visualized as triangles between atoms A and B. Right: Brillouin zone of graphene. Reprinted with permission from ref. (10).

The reciprocal lattice vectors visible in the Brillouin zone illustration are:

$$\overline{b_1} = \frac{2\pi}{3a_0}\left(1, \sqrt{3}\right),\ \overline{b_2} = \frac{2\pi}{3a_0}\left(1, -\sqrt{3}\right). \quad (2)$$

And the locations of the three neighbouring atoms δ_j and second-nearest neighbouring atoms δ_j' of one carbon atom can be given by the lattice vectors as:

$$\delta_1 = \frac{a_0}{2}\left(1, \sqrt{3}\right),\ \ \delta_1 = \frac{a_0}{2}\left(1, -\sqrt{3}\right), \delta_1 = -a_0(1, 0), \quad (3)$$

$$\delta_1' = \pm a_1,\ \delta_2' = \pm a_2,\ \ \delta_3' = \pm(a_2 - a_1)\,. \quad (4)$$

The two atom unit cell means that graphene has three acoustic (A) and three optical (O) phonon modes. The dispersion of these modes, as presented in Figure 2, describe the relation between the energy and the wave vector of the phonon. As the phonon wave moves in the matter the atoms can be displaced in the same direction the wave is propagating (L, longitudinal mode) or in the perpendicular direction than the wave is propagating (T, transverse mode). Both of these displacements happen in in-plane direction but for a 2D material such as graphene the displacements can also happen out of plane. This is called a flexural mode (Z).[12] The optical phonons are particularly responsible for graphene vibrations whereas acoustic modes, especially ZA mode, are for thermal properties.

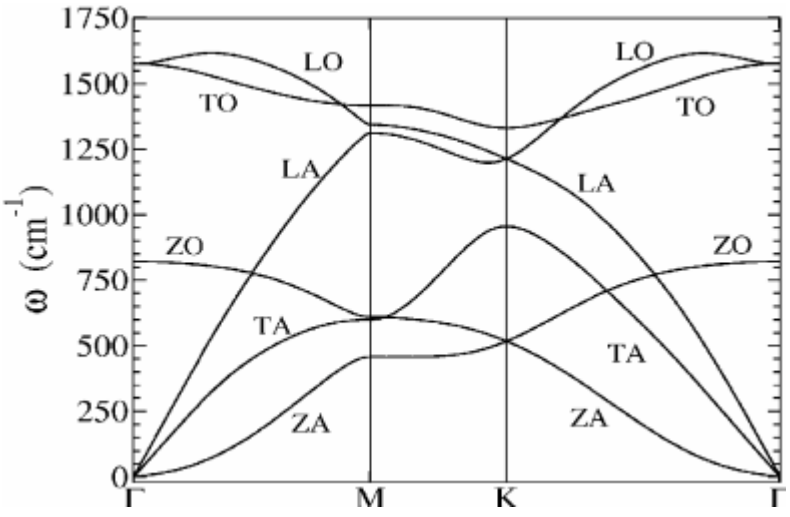

Figure 2. Phonon dispersion of graphene.[13]

Graphene is an excellent thermal conductor. In room temperature, the in-plane thermal conductivity of suspended graphene is[14] around 2000-6000 W/mK, depending on the purity of graphene, and 600 W/mK for graphene on SiO_2 substrate. The great in-plane conductance is due to strong covalent bonds that enable heat-conducting phonons to propagate with almost no losses. The more impurities the graphene has, the higher the losses are as well.[1] The lower thermal conductance of graphene on substrate is due to the weak van der Waals interactions between the sheet and the substrate and in case of SiO_2 is due to the heat conducting phonons scattering and coupling with the vibrational modes of the substrate. Cross-plane thermal conductance of graphene is weak in general due to the weak van der Waals interactions.[12] Temperatures close to the surface of Sun (5000 K) are needed to melt graphene. To highlight the speciality of graphene's thermal properties, steel, for example, has[15] a thermal conductivity of 50.2 W/mK so when put in perspective with other materials, even graphene on substrate has phenomenal heat conductance.

As mentioned before, phonons are also behind molecular vibrations. The point group of ideal single-layer graphene is D_{6h}.[16] After treating the symmetry and point group of graphene according to the group theory, the vibrational, translational and rotational modes of graphene can be accessed. The irreducible representation of graphene is[16]:

$$\Gamma^{graphene} = A_{2u} + B_{2g} + E_{1u} + E_{2g}. \quad (5)$$

The two *u*-terms are translations perpendicular and in graphene plane respectively, and the *g*-terms are vibrations where graphene atoms either move perpendicular to graphene plane or in the plane. The B_{2g} is inactive optical phonon (ZO mode) and E_{2g} is Raman active doubly degenerate vibration (LO & TO modes). Because of this, in first-order Raman measurements of graphene, only one vibration (G-band) should be visible around 1587 cm^{-1}. In practice, four peaks can be seen in Raman spectrum of graphene[16]. The optical phonons are also largely behind this phenomenon. This is discussed in depth later in chapter: Imaging of graphene and plasmons.

1.2 Electrical properties

As mechanical properties derive from the σ-bonds, the electrical properties stem from the π-bonds. The π-bands that uniformly expand over graphene enable all the non-bonding

electrons of graphene to be delocalized over the whole sheet as an electron plasma, similar to that in metals. This enables the electrons to move freely and give rise to the conductive properties in graphene. Usually matter has average electron free path in the range of nanometres but due to the peculiar properties of graphene charge carriers, as described in the following sentences, for graphene the same value is in micrometre range. The Brillouin zone and the unit lattice of graphene are important parameters when determining graphene's electrical properties. The Brillouin zone, presented in Figure 1, is in its simplicity only a rudimentary cell of reciprocal lattice. The *K* and *K'* points of the zone, also called the Dirac points, situated at the positions of type A and B carbons in each unit lattice, have energy that has linear relation to the wave vector. This linear relation leads to the charge carriers (electrons and holes) behaving like massless Dirac fermions, which means that they can travel at the speed of light in certain directions and relativistic theory needs to be considered in their wave functions, hence Dirac notation. The conduction and valence bands of graphene also touch at the Dirac points. This makes graphene a zero band gap material and the band gap is situated at the Fermi level. Doping changes the Fermi level and the band gap of graphene by changing the amount of charge carriers, simultaneously shifting the conductance characteristics.[6] The aforementioned phenomenon of charge carriers acting like quasiparticles also causes graphene to exhibit the anomalous half integer quantum hall effect. In quantum Hall Effect a perpendicular current compared to the main current is formed by strong external magnetic field. The Hall conductivity becomes quantized and is multiplied by a factor, in graphene's case by a half integer. This is anomalous as usually the multiplier is full integer or fraction. Another anomalous factor is that the phenomenon can be observed in graphene also in room temperatures, when it usually requires much lower temperatures.[17]

The theoretical expression for the π-band energies can be obtained by considering tight-binding approach for undoped single-layer graphene. This necessitates involvement of quantum mechanics and even though the charge carriers act like Dirac fermions, necessitating the use of Dirac equation, the tight-binding approach utilizes ordinary Schrödinger equation in lattice potential field $V(\mathrm{r})$[18]:

$$\widehat{H}|\Psi(r)\rangle = \varepsilon|\Psi(r)\rangle, \quad \widehat{H} = -\frac{\hbar^2}{2m}\nabla^2 + V(r), \tag{6}$$

where $\widehat{H}$ is the Hamiltonian, $|\Psi(r)\rangle$ is the wave function, ε is the energy of the system, ħ is reduced Planck's constant and *m* is the mass of the particle. The lattice potential of graphene has a form of $V(r)=V(r - r_j)$, where *j* is A or B type carbon atom. Electrons on $2p_z$ orbitals can also be called Bloch electrons because they reside in periodic structures. The wave function is a linear combination of specific Bloch wave functions. The total wave function $|\Psi(r)\rangle$ and the form of Bloch wave function $|\Phi_j(r)\rangle$ are presented in equation (7)[10,18]:

$$|\Psi(r)\rangle = \sum_j \lambda_j(k)\,|\Phi_j(r)\rangle \;\; ; \;\; |\Phi_j(r)\rangle = \frac{1}{\sqrt{N}}\sum_j e^{i\bar{k}\cdot\bar{r_j}}\,\Phi_j\big(r - r_j\big), \qquad (7)$$

where *k* is the wave vector, *N* is the number of unit lattices and Φ_j is the number of $2p_z$ orbitals. By inserting the wave function in equation (7) into equation (6) and multiplying with bra notation of the wave function the secular equation can be obtained[10,18]:

$$\left|\widehat{H} - \varepsilon\hat{S}\right| = 0, \qquad (8)$$

where $\hat{S}$ is the overlap integral. Now nearest and second nearest neighbour approximation is taken into consideration. This means that we consider for example A-type carbon and its Bloch electron which can jump to all neighbouring B-type atoms and beyond that to the A atoms neighbouring those B-atoms. Due to the symmetrical lattice of graphene all these adjacent hops are identical. The hopping can be expressed by hopping energy *t* for nearest neighbour hopping and *t*' for second nearest neighbour hopping.[18] The Hamiltonian obtains form[11]:

$$\widehat{H} = -t\sum_{\langle i,j\rangle,\sigma}(a^{\dagger}_{\sigma,i}\,b_{\sigma.j} + h.c) - \; t'\sum_{\langle\langle i,j\rangle\rangle,\sigma}(a^{\dagger}_{\sigma,i}\,a_{\sigma.j} + b^{\dagger}_{\sigma,i}b_{\sigma.j} + h.c), \qquad (9)$$

where *h.c* is Hermitian conjugate, σ is spin up or down and the whole term $a^{\dagger}_{\sigma,i}$ means that an electron is created with spin up or down at the neighbouring atom simultaneously removing it from its original location. This can be solved to give the form for the band energy[11]:

$$E_{\pm}(k) = \pm t\sqrt{3 + f(k)} - t'f(k), \tag{10}$$

$$f(k) = 2\cos\left(\sqrt{3}k_y a_0\right) + 4\cos\left(\frac{\sqrt{3}}{2}k_y a_0\right)\cos\left(\frac{3}{2}k_x a_0\right). \tag{11}$$

It can be seen from the equation that both bands are symmetrical if *t*' is near zero. However, if this is not the case, the bands become unsymmetrical.[11] The band structure of graphene is unusual for a semiconductor material. Usually semiconductors have parabolic band structure, but graphene has a very sharp cone structure. This is due to the charge carriers' quasiparticle-like nature. Near the Dirac points the charge carriers can move almost at the speed of light as the 2D energy spectrum is linear.[6,17] The dispersion relation and the speed of the charge carriers, also called as Fermi velocity, can be modelled by expanding equation (10) near the *K* and *K'* points. The second nearest neighbour hopping energy *t*' can be neglected as it generally is rather low, and the wave vector has the form $\bar{k} = \bar{K} + q$, where $\bar{K}$ is the vector of Dirac point position and *q* is the Fermi momentum with form $q = \sqrt{\pi|n|}$, where *n* is the carrier density. The band structure and band energy diagram of graphene is presented in Figure 3. Just put simply the relation becomes[9,19]:

$$E_{\pm}(k) = E_{\pm}(q) = \pm\hbar v_F q \quad ; \quad v_F = \frac{3a_0 t}{2\hbar} \approx 10^6 \ \frac{m}{s}. \tag{12}$$

This relation can also be called the Fermi energy E_F.

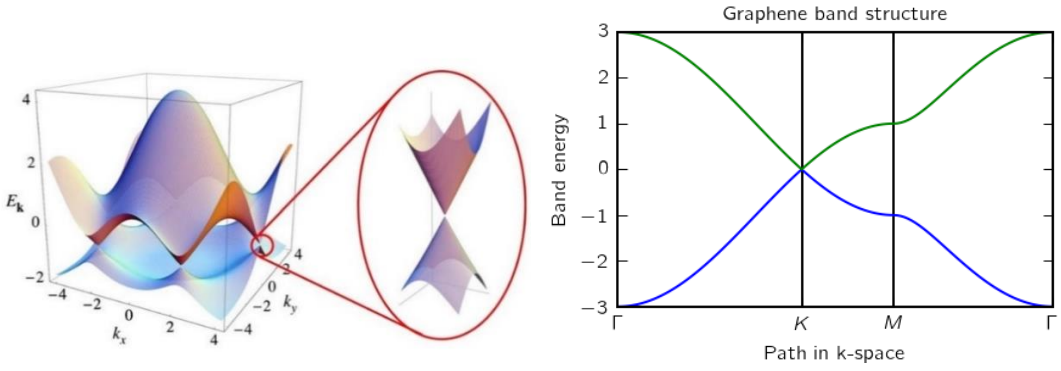

Figure 3. Left: Graphene band structure. Right: diagram of graphene band energy. Reprinted with permission from ref. (11).

1.3 Optical properties

The conductivity of graphene for higher frequencies can be expressed as[20]:

$$\sigma(\omega) = \frac{e^2\omega}{i\pi\hbar}\left[\int_{-\infty}^{+\infty} d\varepsilon \frac{|\varepsilon|}{\omega^2}\frac{df_0(\varepsilon)}{d\varepsilon} - \int_{0}^{+\infty} d\varepsilon \frac{f_0(-\varepsilon) - f_0(\varepsilon)}{(\omega + i\delta)^2 - 4\varepsilon^2}\right], \tag{13}$$

where ω is radian frequency and $f(\varepsilon)$ is Fermi distribution function with form:

$$f_0(\varepsilon) = \left\{exp\left[\frac{(\varepsilon - \mu)}{T}\right] + 1\right\}^{-1}, \tag{14}$$

where T is the temperature and μ is the chemical potential. The first part corresponds with intraband electron-phonon scattering process and the second part is interband electron transition.

The surface conductivity of graphene in the FIR and THz range is dominated by intraband conduction and the interband conduction can be neglected. Now from general conductivity formulation presented in equation (13), a Drude-like conduction can be obtained[21–23]:

$$\sigma(\omega) = \frac{ie^2|E_F|}{\pi\hbar^2(\omega + i\tau^{-1})}, \tag{15}$$

where E_F is the Fermi energy and τ is the relaxation time. In higher frequencies the conductivity depends on previously neglected interband absorption. Single layer graphene has rather universal absorbance of 2.3 % for frequencies from infrared to visible. This depends on the fine structure constant α and optical conductivity σ_0 of graphene. For undoped graphene an universal optical conductivity holds due to the charge carriers behaving like Dirac fermions [23–25]:

$$\sigma_0 = \frac{e^2}{4\hbar}. \tag{16}$$

Only in UV region graphene exhibits slightly higher absorption due to electrons moving between unoccupied π states. The absorbance is determined and calculated with[25]:

$$A(\omega) = \frac{4\pi}{c} \cdot \sigma_0 = \pi\alpha \approx 2{,}3\ \% \tag{17}$$

The absorbance can be altered via doping. Doping increases the chemical potential of graphene and in turn the conductivity of graphene surface increases.[26] The optical properties also depend on the amount of layers of graphene. The absorbance is increased by 2.3 % for each layer.

Several optical processes can affect the absorbance of graphene. The most basic way is for the incident light to excite an electron from the valence band to the conduction band as for most materials. After 10-150 fs these electrons lose excitation gradually via electron-electron scattering, moving down in a pattern that forms the conical Fermi-Dirac distribution distinct for graphene, as they release energy to lower-energy electrons. Now they have formed an electron-hole pair that can possibly block some other interband transitions from occurring, effectively damping the absorption. Because the electrons left the valence band, there is now a shortage of charge carriers in the valence band, and the system stabilizes itself by intraband phonon scattering and electron-hole recombination, until the equilibrium is reached once again. This is only true for low excitation intensities. If the excitation intensity is high, so many electron-hole pairs have been formed by interband excitation and thermally cooling down that the states near the intersection between the conduction and valence bands are completely filled out. No more absorption can happen in this case, due to Pauli blocking. This is called a saturable absorption.[27] Illustration of these events is presented in Figure 4.

These are all linear optical processes but graphene also has several nonlinear optical processes that depend on the photocarrier density. To model nonlinear optical response of graphene a Boltzmann transport equation can be utilized[28]:

$$J_n = \frac{1}{4\pi^2} \int v_g N(p)\ dp, \tag{18}$$

where v_g is the group velocity and $N(p)$ is the carrier population in terms of the momentum space p. As the Schrödinger equation was combined before with the Bloch waves, the same can be done for the Dirac equation and substituting carrier population and group velocity with terms obtained this way yield a model that is rather accurate for electronic dynamics in graphene. The total integrated electric current is[29]:

$$J_n(t) = \frac{g_g g_v e}{(2\pi\hbar)^2} \int j_e(t)\ dp, \tag{19}$$

where g_g and g_v are spin- and valley-degenerancy factors, respectively and j_c is the carrier current in retrospect to the wave vector/momentum components x or y:

$$\begin{aligned} j_{c,x} &= v_F\left[(n+1)\cos\theta + i\sin\theta\{\rho e^{-2i\Omega} - c.c\}\right] \\ j_{c,y} &= v_F\left[(n+1)\sin\theta - i\cos\theta\{\rho e^{-2i\Omega} - c.c\}\right], \end{aligned} \tag{20}$$

where n+1 is the carrier occupation, $c.c$ is the complex conjugate and Ω is the instantaneous temporal phase.

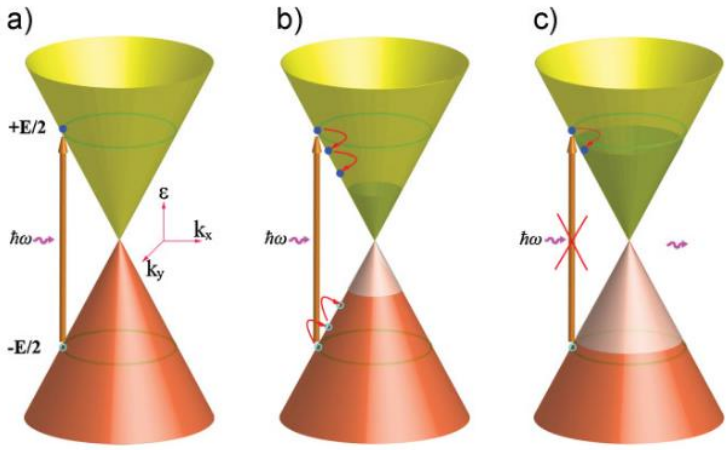

Figure 4. a) Excitation of electrons via external light. b) Thermal cooling and intraband phonon scattering of the formed electron-pair until equilibrium is reached. c) Saturable absorption due to Pauli blocking with higher excitation intensities. Reprinted with permission from ref. (27)

The nonlinear processes in graphene include third-harmonic generation (Figure 5a left), where three similar transitions from valence state to conducting state form a single transition that has 3 times the frequency the original transitions had, and two photon absorption (Figure 5b), where two photons can be absorbed for the same charge carrier leading to higher excitation.[30] As well as few more complex optical processes. All of these linear and nonlinear properties make graphene suitable for a plethora of optical applications.

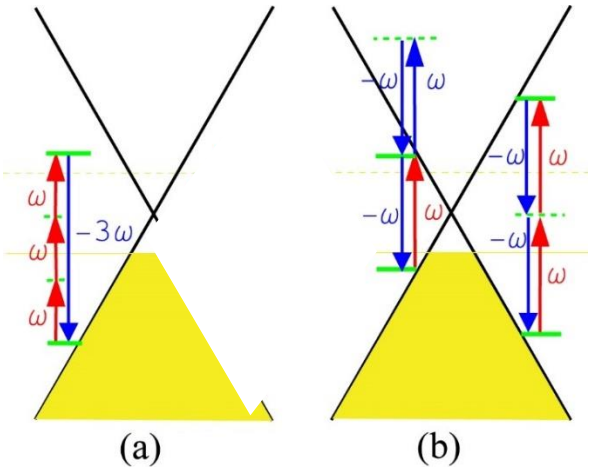

Figure 5. a) Third-harmonic generation of graphene. b) Two-photon absorption mechanisms of graphene. Reprinted with permission from ref. (30).

1.4 The effect of substrate and functionalization on graphene properties

As graphene is extremely thin material it usually needs to be supported by a substrate. The choice of substrate greatly affects the properties of graphene as there are always at least weak chemical forces, such as van der Waals forces, between the substrate and the graphene sheet. As mentioned before at least the thermal conductivity greatly depends on whether the graphene is suspended or deposited on substrate. The differences can also be seen in chemical reactivity and these differences can be probed with Raman spectroscopy and contact angle measurements as chemical reactivity correlates with hydrophobicity. Example Raman spectra of pristine and functionalized graphene on different substrates is presented in Figure 6.[31] The choice of substrate also depends on the desired use of graphene sheet as some applications require graphene to substantially interact with the substrate and some would preferably have no interaction. Unfortunately, the mechanism behind the interaction of graphene and substrate that could explain the differences between different substrates conclusively, has been hiding from the researches despite

numerous efforts. Most often used substrate for single-layer graphene sheets is SiO_2 because of its insulation nature. As mentioned before, it was commonly believed that graphene interacts with SiO_2 with Van der Waals forces, but recently the SiO_2 substrate effect on graphene has been shown to be due to electrostatic interaction between graphene and surface charges that originate from the oxide fabrications and protonation on the surface of SiO_2.[32] Other suitable substrates for graphene are pure silicon, SiC, polymer and metals such as copper. SiC intrinsically *n* dopes the graphene. Two layers of graphene on top of SiC seem to be optimal as the first layer acts as a buffer with untypical properties for graphene, but the second layer acts normally. Graphene can act alike to the freestanding graphene when deposited on top of pure Si surface as it does not necessarily have dangling bonds that could interact with the sheet, modifying its properties.[33]

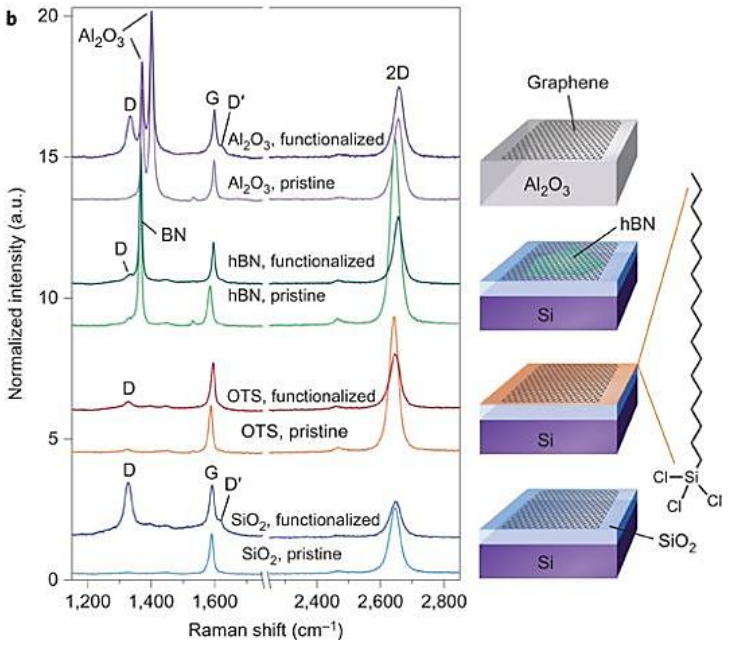

Figure 6. Raman spectrum of pristine graphene and graphene functionalized with 4- nitrobenzenediazonium tetrafluoroborate on different substrates. The used substrates were 300 nm SiO_2 on silicon, previously mentioned substrate with self-assembled monolayer of octadecyltrichlorosilane, a hBN single crystal flake on SiO_2 and polished sapphire (Al_2O_3). Modified with permission from reference (31).

In addition to substrate, functionalization of graphene can also affect its properties. There is plethora of interest and therefore also methods to chemical functionalization of graphene as functionalized graphene could for example act as a small electronic chip with

conducting and non-conducting areas depending on the surface functionalization. The most typical type of functionalized graphene is graphene-oxide (GO), which consists of a graphene sheet covered in different oxygen containing groups such as hydroxyls and carbonyls. Studies show that GO is as strong and stress-bearing as unfunctionalized graphene, which makes sense as the σ-bonds are not changed in the oxygenation even though the hybridization of carbon atoms change from sp^2 to sp^3. Logically this does affect the electrical properties as this hybridization disturbs the uniform π-bands.[34,35] Graphene is generally oxidized unless it has been annealed (reduced GO or rGO) as interaction with air can readily oxidize it. Graphene can also be oxidized in very specific locations with femtosecond laser essentially creating non-conducting areas in graphene.[36] Same method in inert gas environment has also been shown to be able to modify single-layer graphene in three dimensions.[37] This is discussed in depth in chapter 5: Optical forging. In addition to oxidized graphene and specifically to further functionalization from GO, there are several other ways to covalently modify graphene: nucleophilic substitution, normal and electrophilic addition and condensation. GO functionalized via condensation can for example be used as a material for nanocomposites. Graphene can also be functionalized non-covalently by absorbing surfactants or other molecules. This allows interactions with for example biomolecules.[38] In conclusion, hydrophobicity, solubility, surface conductivity and ability to interact with different molecules can be altered with chemical functionalization. In Figure 7, an example of utilization of non-covalent functionalization of graphene with a fluorescent DNA probe is shown.[39]

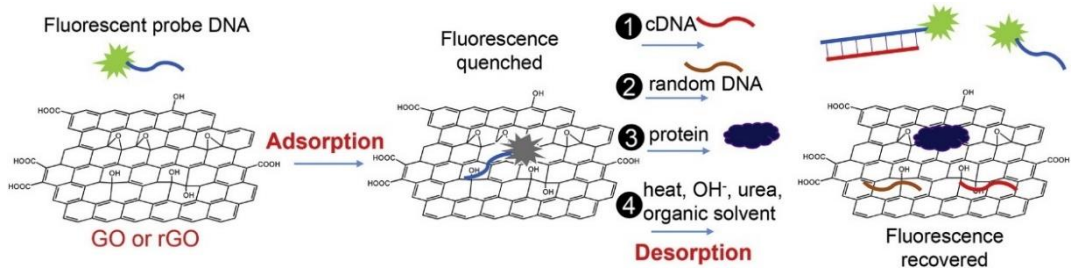

Figure 7. A fluorescent DNA probe is absorbed into graphene via non-covalent functionalization and the fluorescence is quenched. The probe can desorb in presence of certain molecules or conditions regaining the fluorescent ability, making the system a detector for these specific conditions. Reprinted with permission from reference (39). Copyright Elsevier 2019.

1.5 Preparation

As mentioned before, the earliest method of preparation of single-layer graphene was performed by Andre K. Geim and Konstantin S. Novoselov. Their method was rather rudimentary yet effective for its simplicity, as they used scotch tape to mechanically exfoliate graphene from graphite.[40] The problem with this method is that controlling the amount of layers exfoliated is impossible and the result is uneven film of varying amount of graphene layers.[4] This method is also not easy to scale up or to use reliable to produce only one type of graphene. In the scale of this thesis, only preparation methods that result in higher quality devices fit for electronics and photonics are mentioned here.

Aside from the adhesive tape method demonstrated by Novoselov and Geim, also different types of exfoliation methods are used to prepare single-layer graphene. Even though mechanical exfoliation is by far the best method of producing high quality graphene in terms of electrical and optical performance, liquid phase exfoliation has been shown to produce decent quality graphene for example for composites and inks. Liquid phase exfoliation involves dissolving powdered graphite into organic solvents, where it disintegrates into smaller layer with help of sonification, and depositing flakes of graphene by spray coating, vacuum filtration or drop casting.[41] Electrochemical exfoliation sometimes combined with intercalation have been shown to produce high quality graphene. In this method applied voltage drives ions in solution to intercalate into the graphite electrode, forming gas bubbles which can exfoliate layers of graphite apart from one another, forming graphene.[42]

Perhaps the most used and widely regarded as the most promising method to prepare high-quality single-layer graphene is Chemical Vapour Deposition (CVD). In short, CVD is a fabrication method suitable even for nanoscale materials, where a carbon-containing precursor material is used to epitaxially create a graphene layer on top of a catalytic substrate from vapour via chemical reaction.[43,44] Other option is that the carbon atoms form graphene on the substrate by segregating from the substrate itself. These two reaction mechanisms can also happen simultaneously. The occurrence of the surface segregation depends on the substrate used. Nickel, for example, can allow diffusion of carbon atoms enabling the CVD and surface segregation to happen simultaneously but the same does not hold true with copper.[45] Transition metals are great catalysts for graphene synthesis, but copper is most preferable, as it has very low carbon solubility. [46]

Copper also has the advantage of CVD process being self-limiting and stopping at single-layer graphene.[45]

The basis for graphene preparation via CVD is always pretty much the same, transition metal substrate is placed in the CVD oven and different precursors are used in epitaxial synthesis of graphene. Such precursors can be solid carbon, liquid hexane and even solid sucrose. Interestingly, even waste containing carbon, such as insects[47] and plastic waste[48] can be utilized as precursor, resulting in graphene sheets comparable to those produced with common precursors like methane gas. Methane gas, diluted or full-fledged, is an important precursor for graphene CVD as it has been shown to limit the graphene growth to single layer.[49] Most common method for graphene on copper -preparation is decomposition of methane in 1000 °C in low pressure.[46] Hydrogen gas is mixed with the methane and better deposition area is obtained by annealing the copper film in high temperature under hydrogen gas before starting the synthesis.

In order to use CVD graphene for optical or electrical applications, the prepared sheet must be transferred on an insulating or semiconducting surface. This is often done by coating graphene with PMMA or polydimethylsiloxate (PDMS) and etching the copper film away with acid or certain metal-salts. Obtained polymer-graphene sheet mix can be placed on the desired substrate and the polymer can be removed by dissolving it. After this graphene and the surface are annealed to ensure all the solvent and moisture is gone.[49] As mentioned before, the substrate can affect graphene's properties, and the quality of the graphene sheet can also suffer during the transfer as wrinkles, tears or impurities can be introduced.[45] Other issue with CVD is that the graphene does not necessarily have the same orientation in all the areas.[45] Graphene growth process on copper in CVD and a common transfer method[50] are presented in Figure 8.

Graphitization is also a method to create graphene epitaxially by thermal decomposition of SiC crystals. High temperatures anneal the SiC crystal desorbing the Si atom and causing the carbon atoms on the surface to rearrange to graphene layers. The properties of the created graphene layer can be altered by fine-tuning the pressure and used gas. This method has the advantage of easier control on the number of layers as well as uniform orientation of the graphene in wafer-scale. In addition, this method does not necessitate a transfer to another substrate as the layer below the graphene consists of a buffer layer[45] as described in the chapter 1.4: The effect of substrate and functionalization on graphene properties.

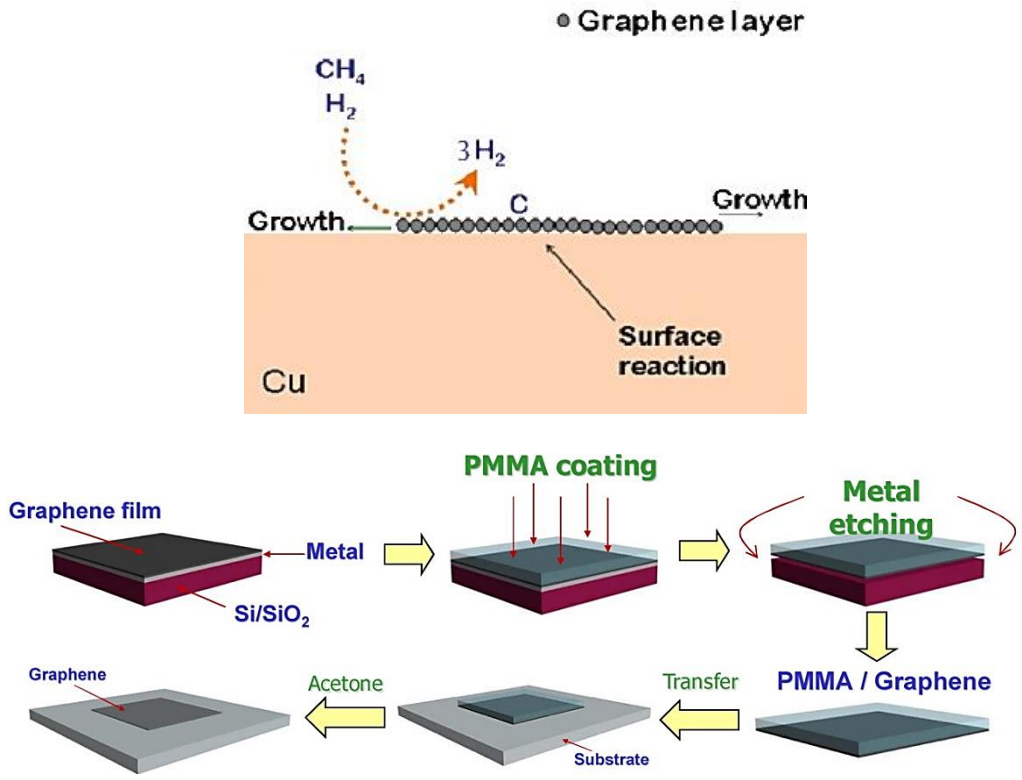

Figure 8**.** Above: CVD graphene growth mechanism on copper. Below: CVD grown graphene transfer method. Reprinted with permission from ref. (50). Copyright 2019 American Chemical Society.

2 Graphene plasmons

Plasmons are oscillations of free charge carriers in materials. Most commonly plasmons are met in metals as their electrons form the freely moving electron sea or plasma hence the word plasmon. The working principle of a surface plasmon is presented[51] in Figure 9. Plasmons can also be generated in other materials with free charge carriers such as some semiconductors and nanoparticles. Plasmons have baffled scientists all the way from the beginning of the 20th century. At first plasmons were seen as anomalies that did not fit the existing physical descriptions for electromagnetic light, even though Maxwell had predicted the existence of EM oscillations already late 19th century.[52] More understanding was gained upon their discovery and numerical modelling in 1952 by Pines and Bohm, whom first defined them as plasmons. Pines and Bohm had modelled the bulk plasmons which differ from the surface plasmons (SPs) discussed in this thesis. Bohm and Pines deduced that these oscillations were quantum mechanically explainable due to long range electronic correlations in the Hamiltonian[53] and they were able to find the resonant frequency of plasmons in bulk plasma.[52] In 1960 Stern and Ferrel modelled and named

the surface plasmons as they were studying oscillations in 2D electron gas, which electron plasma on metallic surface can be thought to be.[54] Plasmons can be excited with quantized energy, usually a photon, but electrons and phonons can also be used to excite the oscillations. This is not as simple as it sounds as there is often a large mismatch between the exciting creature, for example light, and the wave vector of the plasmon.[52] For metals this mismatch can be overcome by prisms or periodic structures or other topological alterations. [55] Plasmons can also couple with these charge or energy carriers in the similar way as they would be excited. In this case the plasmons are called plasmon polaritons (PPs). All of this allows EM energy on the surface to be controlled and confined in the subwavelength scale enabling applications such as enhanced surface sensing- and spectroscopy methods, heat generation and control for example in nanotherapeutics, and in non-linear optics.[56]

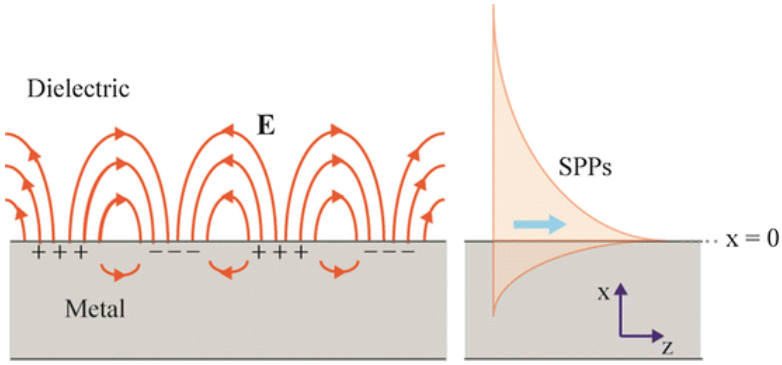

Figure 9. Formation and propagation of a surface plasmon polaritons (SPPs). Reprinted with permission from ref. (51).

Graphene plasmons are an anomaly in the plasmonic world and are of great interest to researchers in both the field of plasmonics and graphene. This is because graphene surface plasmons (GSPs) have vastly different properties and many advantages compared to the plasmons in metals. GSPs appear in the far infrared to terahertz range, whereas metal plasmons are usually in the visible region. Graphene's extreme electrical properties are a great tool, as high carrier mobility indicates lower losses and the tunability of graphene allows the amount of charge carriers and the Fermi level to be altered.[57] Graphene plasmons have even greater mismatch between the plasmons and the exciting light than metals do, but as with metals, this can be overcome by using nanostructures in graphene to excite localized surface plasmon resonances (LSPRs)[58], use gratings or prism[59] as with metals or use a metallic tip to excite the plasmons directly[22]. Illustration of the mismatch differences are presented in Figure 10. Important parameters for plasmonics both for

metals and graphene are presented in table 1. The parameters and equations are introduced in the following chapters.

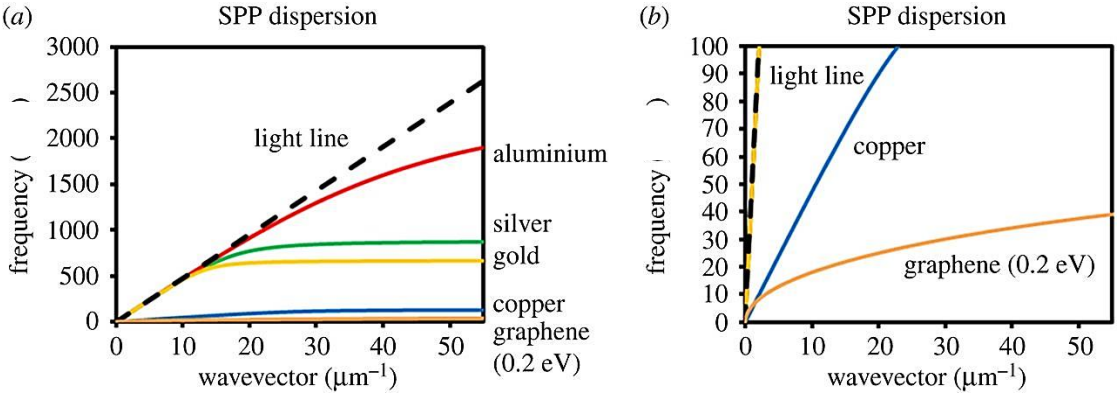

Figure 10. Wave vector momentum mismatch of metals and graphene. Reprinted with permission from ref. (28).

Table 1. Parameters of graphene and metal plasmonics

Parameter	Graphene	Metal
$\boldsymbol{\lambda_{SP}}$	$\lambda_0(4\alpha E_F)/\hbar\omega(\varepsilon_r+1)$	$\lambda_0[(\varepsilon_d+\varepsilon_m')/\varepsilon_d\varepsilon_m']^{1/2}$
$\boldsymbol{\delta_{SP}}$	$\lambda_0(\tau\alpha E_F)/\hbar\omega(\varepsilon_r+1)$	$\frac{\lambda_0(\varepsilon_m')\left[\frac{(\varepsilon_d+\varepsilon_m')}{\varepsilon_d\varepsilon_m'}\right]^{\frac{3}{2}}}{2\pi\varepsilon_m''}$
$\boldsymbol{\sigma_i}$	$\lambda_{SP}/2\pi$	$\frac{\lambda_0\left[\frac{(\varepsilon_d+\varepsilon_m')}{\varepsilon_m'^2}\right]^{\frac{1}{2}}}{2\pi}$

2.1 Basic parameters of plasmons

Maxwell's equations are the very primary theoretical basis for plasmons. When modelling surface plasmons, the interface between semi-infinite metal medium with permittivity ε_m and a dielectric medium with permittivity ε_d, as seen in Figure 9, is considered and under certain boundary conditions the dispersion relation for SPs is[55]:

$$k_{SP} = k_0 \sqrt{\frac{\varepsilon_d \varepsilon_m}{\varepsilon_d + \varepsilon_m}}, \tag{21}$$

where k_{sp} is the wave vector of the SP and k_0 is the wave vector of the free-space photon. When considering the interaction between the electron plasma at the surface and the EM field of light, two important conclusions can be drawn:

1) The momentum of the SPs are greater than that of the free-space photon. This is illustrated in Figure 11.
2) The near field (field perpendicular to the surface) decays exponentially as distance from the surface grows.

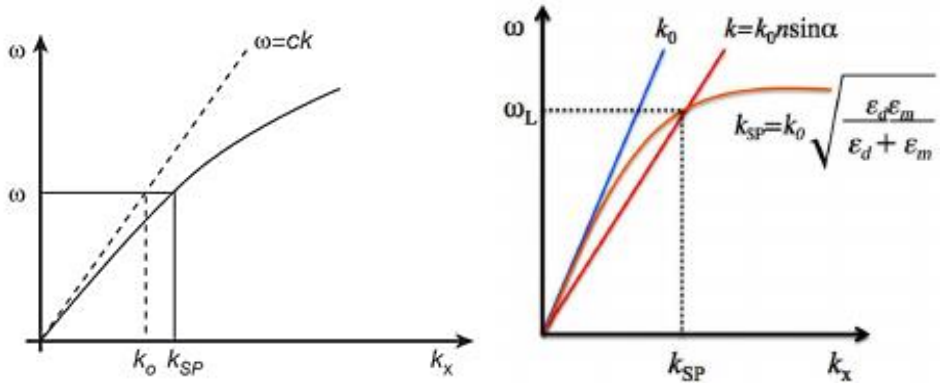

Figure 11. On the left: The linear frequency of free-space photon (dashed line) and the non-linear frequency of the SP clearly demonstrate the momentum mismatch preventing the coupling. Modified with permission from ref. (55). On the right: The momentum of free-space photon k_0, photon that has passed a prism k and the plasmon wave vector k_{sp}. Reprinted with permission from ref. (60).

The mismatch could be overcome, as presented in the introductory chapter, with for example a prism. An illustration of how a prism can transform the momentum of the incident light to match the momentum of the SPs[60] is also presented in Figure 10. The decay of the near field prevents the plasmons from propagating off the surface.

For a surface to be able to support plasmons, the permittivities of the different media must have opposite signs. It is also important to note that the dielectric function (of metal) as well as the wave vector of SPs are complex with real and imaginary parts:

$$k_{SP} = k_{SP}{}' + ik_{SP}{}''$$
$$\varepsilon_m = \varepsilon_m{}' + i\varepsilon_m{}''. \quad (22)$$

The wavelength[61] of a plasmon depends on the real part of the wave vector, which depends itself on the real an d imaginary parts of the metal's dielectric constant as well as the dielectric constant of the dielectric material.[62] The presentation for SP wavelength is:

$$\lambda_{SP} = \frac{2\pi}{k_{SP}{}'} \approx \sqrt{\frac{\varepsilon_m{}' + \varepsilon_d}{\varepsilon_m{}'\varepsilon_d}}\lambda_0, \quad (23)$$

where the λ_0 is the wavelength of the exciting light. The imaginary part of the wave vector, or rather the ratio between the imaginary and real part[22] factors in with the exponential damping of the plasmons. The imaginary part also affects the propagation distance of the SPs. Propagation distance describes the length that the SP travels until the intensity of its mode reaches 1/*e* of its initial value and is considered dampened:

$$\delta_{SP} = \frac{1}{2k_{SP}{}''} = \frac{c}{\omega}\left(\frac{\varepsilon_m{}' + \varepsilon_d}{\varepsilon_m{}'\varepsilon_d}\right)^{\frac{3}{2}}\frac{(\varepsilon_m{}')^2}{\varepsilon_m{}''} \quad (24)$$

Other important plasmon parameter is the penetration depth δ_i. Penetration depth is an important parameter to consider when SP confinement is considered. It is considered separately for both the dielectric and metallic medium and has the form[63]:

$$\delta_i = \frac{\lambda_0}{2\pi}\left(\frac{|\varepsilon_m{}'| + \varepsilon_d}{\varepsilon_i^2}\right)^{1/2} ; \; i = d, m. \quad (25)$$

For the dielectric this is roughly half of the incident wavelength and for the metal it depends on the skin depth.

Confinement of light or SPs and how good material is for it can be expressed as effective SP index λ_0/λ_{SP}. The SP indexes for metals are small compared to that of graphene.

Graphene can have effective index as high as 70, whereas metals usually have indexes under 10.[64] Aforementioned penetration depth is vital in determining SPP index of material and as graphene is very thin, it also has larger confinement of light.[52]

Silver is considered to be the top option for metallic SPs as it has low optical losses in vis and NIR resulting in propagation distances ranging from 10-100 µm.[55] The drawback with silver is it affinity for oxidation resulting in surface roughness, which causes more losses for plasmons. Metallic nanoparticles in different shapes can also be used to produce a variety of different plasmonic response. Metals are not the only possible media for the plasmons and heavily doped semiconductors can work in this role as they exhibit metal-like properties. For example telluride or some nitride materials can be highly doped and support plasmons in NIR and vis regions. Semiconductor plasmons, unlike metal SPs, are tunable, which gives significant advantage. Semiconductor SPs have relatively low losses and their anisotropic crystalline structure can cause plasmonic response in different crystal axes.[56]

2.2 Electro-Magnetic waves in graphene

The SPs in 2D materials differ from the conventional surface plasmons as they are highly confined and their dispersion relation is more separated from that of the incident light, which means that the wave vector momentum mismatch is larger.[56] In addition to all this, graphene had low losses due to the high carrier speeds and its plasmons could be tuned. Graphene has two types of electrons, those on the σ-orbitals and those on π-orbitals. Both of the electron types can support plasmons. Low energy 2D plasmons, with energies below 3 eV, are created by intraband transitions only exist in highly doped graphene. The other types of plasmons also present in pristine graphene are π and $\pi + \sigma$ plasmons.[65] These plasmons are presented in function of their energy compared to Brillouin zone directions (wave vector) in Figure 12. The 2D plasmons are the actual plasmons in the THz and IR range which is also the area of interest in this thesis.

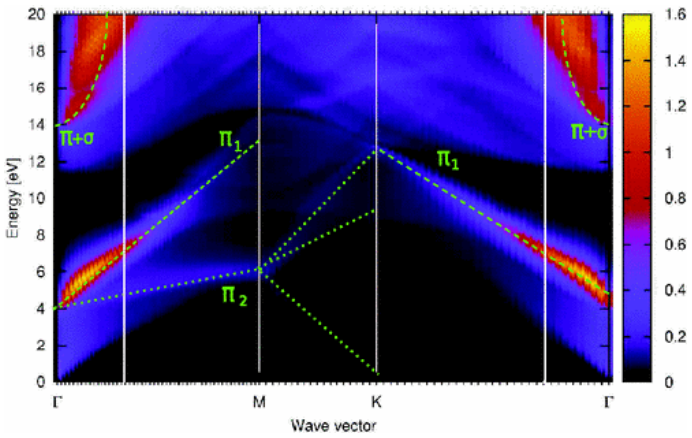

Figure 12. Electronic excitations of pristine graphene.
Reprinted with permission from ref. (65)

Both transverse electronic (TE) and transverse magnetic (TM) electromagnetic waves can propagate in graphene. In addition to wave vector and dielectric function in equation (19), also the conductivity has a complex form. The imaginary term of conduction regulates which mode is supported so that if the term is more than zero, TM waves are supported, and if it less, TE waves are. The TM modes are often located around THz and far-infrared (FIR) regions and TE modes around FIR and near-infrared regions (NIR). However, mainly the TM mode is relevant in graphene plasmonics and will solely be considered here, as the TE mode suffers from damping more at higher temperatures.[66]

This means that graphene may not be the best option for plasmonics in visible or NIR applications. The better option for this range is, for example, a thin gold film. This is due to gold and other noble metals having increased real and imaginary parts of dielectric constant in this range. In the FIR and THz range, the loss in metal plasmons is much stronger due to the imaginary part of dielectric constant increasing over the real part, turning the tables in favour of graphene. The imaginary part of dielectric constant is not as large for one atom thick graphene, so it withstands these low frequency plasmons a lot better than noble metals or metals in general. In addition, graphene has lower optical relaxation time compared to metals, which is beneficial to the dissipation of SPs in materials. Another attribute that is beneficial to lower losses in graphene is the fact that for lower frequencies, the plasmon Landau damping will also lessen. Of course, with higher doping even lower losses of SPPs can be obtained.[52] Landau damping is introduced a bit later in depth.

To obtain a description for dispersion relation for graphene surface plasmons (GSPs), the earlier model for surface plasmons with the metal and dielectric interface can be expanded so that there would be an infinite layer of graphene sandwiched between these two media. The two media t can be noted as (μ_{r1}, ε_{r1}) and (μ_{r2}, ε_{r2}), where μ_r is relative permeability and ε_r is dielectric constant. If magnetism is not considered the relative permeability can be assumed to be 1 in both media. For a typical graphene device with SiO_2 layer below graphene and air above the dielectric constants would be 4 and 1 respectively.[67]

Applying Maxwell's equations and Dyadic Green's function, a dispersion relation can be obtained. Assuming that the graphene sheet is infinitely thin the TM modes dispersion relation is[67,68]:

$$\frac{\varepsilon_{r1}}{\sqrt{k_{TM}^2 - \frac{\varepsilon_{r1}\omega^2}{c^2}}} + \frac{\varepsilon_{r2}}{\sqrt{k_{TM}^2 - \frac{\varepsilon_{r2}\omega^2}{c^2}}} + \frac{i\sigma}{\omega\varepsilon_0} = 0, \tag{26}$$

where the wave vector for the TM modes k_{TM} behaves as the wave vector in equation (21). More comparable to previous equation (21) form and perhaps more intuitive form of dispersion relation is obtained when thickness of graphene t_g is considered by changing the dielectric into form:

$$\varepsilon = \varepsilon_0 + \frac{i\sigma}{\omega t_g}, \tag{27}$$

and now the dispersion relation for graphene plasmons has the form[22]:

$$k_{GSP} = \frac{\hbar^2(\varepsilon_{r1} + \varepsilon_{r2})}{4e^2 E_F}\omega\left(\omega + \frac{i}{\tau}\right). \tag{28}$$

This is a direct result of assuming that the conductivity of graphene has a Drude-like form, as was done in equation (15). The wavelength of graphene plasmons is given similarly as in equation (23), with the k_{SP} being of course k_{GSP}. As frequency of the plasmons depends inversely of the wavelength and the wavelength depends on the Fermi energy ($E_F = \hbar v_F\sqrt{\pi|n|}$), it can be noted that the frequency has the dependence of $n^{1/4}$ of the charge carrier density. For normal semiconductors this dependence is $n^{1/2}$. This is the factor which gives access to the tunability of the plasmon frequency[22].

Exciting the plasmons in graphene can largely be done in the same way as plasmons in metals. Other possibilities for this are carefully designed geometries i.e. nano-disks and corrugations. A good example of how size and geometry can affect SPs are graphene nanoribbons. Their limited width reduces the possible degrees of freedom for GSPs, effectively acting as wave guides. The frequency of the SPs depends on the width of these nanostructures *w* and the density of charge carriers[58]:

$$\omega_{GSP} \propto n^{\frac{1}{4}} \cdot w^{-\frac{1}{2}}. \tag{29}$$

The narrower the ribbons are, higher in frequency they appear, enabling SPs even in MIR region. The edge-conformations (zigzag/armchair) also affect the SPs. Zigzag- form broadens the resonances and causes them to propagate at higher energies. If graphene is undoped, only armchair ribbons can support plasmons, this is due to damping affecting zigzag-mode more as they have electronic edge states.[21,69] Images which displays the GSP frequency dependence on the charge carrier density and nanoribbon width as well as the edge conformation are presented in Figure 13.

Nano-disks are a great way to capture LSPRs. In the case of the nano-disks, the EM field would act as a dipole and the finite-size would once again cause frequency broadening for GSPs. LSPRs could also be created on graphene by introducing controlled defects on graphene in form of for example ripples or corrugations. Such shaped can be obtained by altering the substrate[70–72] or patterning graphene directly via optical forging, a method introduced later in its own chapter. Several theoretical studies suggest that these geometrical subwavelength structures would trap the plasmons creating LSPRs, however, analytical results of this are scarce and hard to come by.

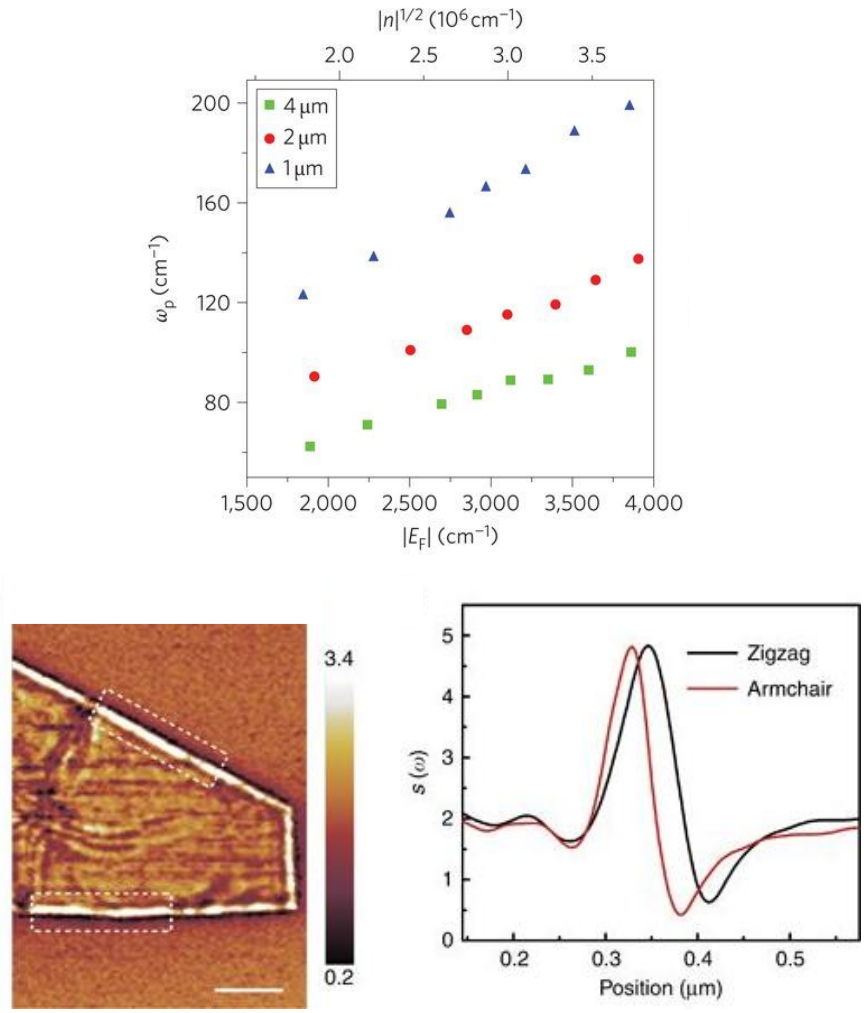

Figure 13. Above: The frequency of graphene plasmons for three different nanoribbon widths as a function of changing charge carrier concentration. Reprinted with permission from ref. (58). Below: Scattering frequency in function of 20 averaged positions inside white rectangles. Reprinted with permission from ref. (69).

Graphene plasmons can also be tuned and introduced via external nanoantennas. Metallic nano- and microstructures can be used to overcome the mismatch between the momenta of the graphene plasmons. For example, gold rods can act as dipole antennas so that the near field at the ends of the rod match the wave vector of the graphene plasmons. The size of these antennas is an important factor, as too short or long antennas are off resonance. The optimal length for the antennas is around half of the wavelength of the incident light.[73] An image illustrating this effect is shown in Figure 14. It has also been observed that the wavelength of the GSP:s launched by these metallic nanoantennas differ slightly from those launched by for example the tip in scanning optical near-field microscopy. Also the temperature and bias-voltage tune the plasmons. With lower

temperature and higher voltage (up to a point) the propagation length of graphene plasmons grows longer.[74]

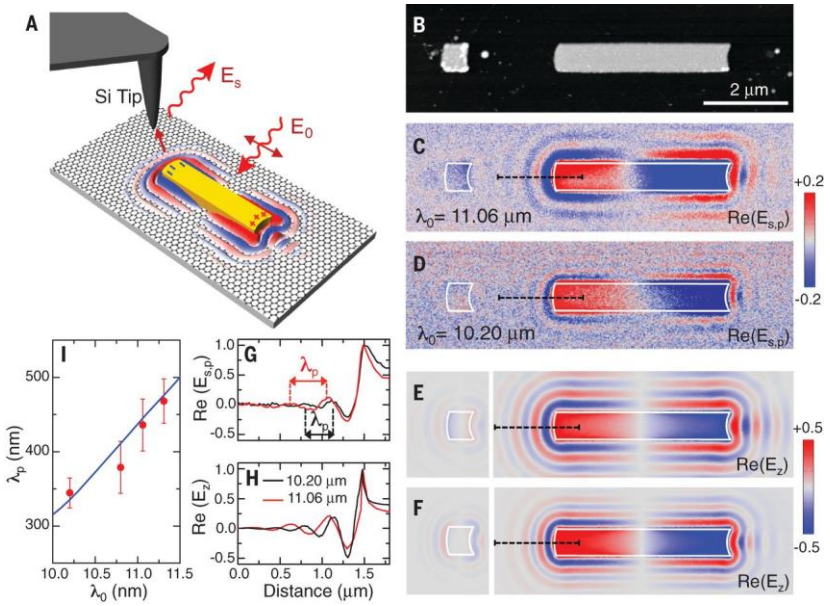

Figure 14. A) Illustration of gold nanorod and SNOM tip. B) Topography image of two different antennas. (Small off resonance, large on resonance). C and D experimental images illustrating real vertical near-field component of the antennas. E and F are the same but theoretical values. G experimental near-field profile along the dashed line in C & D. H is the theoretical version for E & F. I is experimental (dots) vs theoretical (line) GSp wavelength as a function of incident light.
Reprinted with permission from ref. (73)

2.3 Damping of plasmons

A considerable obstacle between realising GSPs and using them in photonics is plasmon damping. Even though the graphene plasmons have lower losses and not as high damping they still encounter some damping. The dominant damping mechanism for graphene plasmons is Landau damping.[75] In the Landau damping the EM wave interacts with charge carriers, and accelerates them to move at the same velocity as the wave. This requires energy from the wave itself, effectively damping it.[76] In case of GSPs, the plasmons decay as they excite an electron-hole pair through inter- and intraband scattering. An illustration of this is presented in Figure 15. In the phenomenon, plasmon wave excites one electron or hole from valence band to conduction band and one

electron/hole from conducting band to pair with it. This damping can once again be eliminated by doping graphene as larger charge carrier concentration makes taking Pauli principle into account necessary, and transitions needed for the phenomenon are no longer allowed.[67] This was also discussed in the optical properties section.

Impurities and many-body effects can also cause damping of the GSPs. Many-body effects that may be the source of damping include electron-electron scattering and optical phonons. These effects can be neglected by improving the sample quality, and studying plasmon frequencies that are lower than that of optical phonons (1580 cm^{-1}) as frequencies higher than that will exhibit considerable losses due to simultaneous emission of phonon and an electron-hole pair.[75]

As mentioned before the plasmon damping rate depends on both the real and imaginary parts of the wave vector and for graphene plasmons it is[22]:

$$\gamma_{GSP} = \frac{k''_{GSP}}{k'_{GSP}} \tag{30}$$

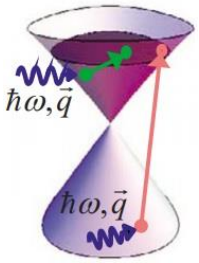

Figure 15. Interband and intraband scattering as a phenomenon behind Landau damping. Reprinted with permission from ref. (75)

2.4 Tuning of GSPs

Because the frequency of plasmons depends on carrier density as can be seen in equation (29), the plasmons can be tuned via bias voltage or with doping. Applying gate voltage may either decrease or increase the amount of charge carriers in the material, usually lower voltages correspond with more hole charge carriers and result in longer wavelengths as well as higher amplitude. Using bias voltage also enables complete suppressing of graphene plasmons even though the damping of plasmons stays roughly same.[22] Image of bias voltage effect on graphene plasmon frequency is presented in Figure 16. Doping can also be chemically done by replacing atoms in the graphene by

boron (one less electron) or nitrogen (one more electron). Placing graphene on a substrate intrinsically dopes graphene via interactions.

Similar nanoantennas as mentioned before can also be utilized in electrical tuning of GSPs. Or vice versa, graphene plasmons can be used to tune the resonance of antennas. Graphene situated in a gap between two elongated antennas will blue-shift the resonance of the antennas when electrostatic doping (bias voltage) is introduced so that the charge carrier concentration increases. The smaller the gap where the graphene lies is, more tunable the resonances become. The amount of interlocked antennas also increases the tuning range.[77]

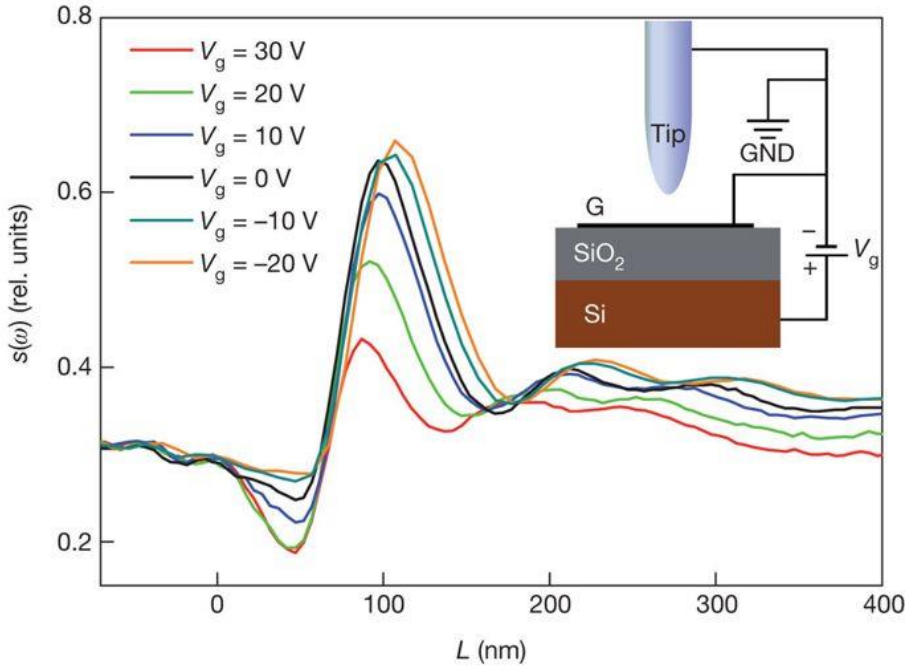

Figure 16. GSP frequency dependence on bias-voltage measured with SNOM setup. Each line corresponds with certain bias voltage, ranging from 30 V to -20 V. Reprinted with permission from ref. (22).

3 Imaging of graphene and GSPs

The characterization of the sample is always necessary to provide comparable and trustworthy scientific data. For graphene interesting properties characterization-wise are the purity and quality of graphene as well as how many layers are present in the sample. The amount of layers in graphene can change the properties drastically so it is important

to make sure that most of the sample has the desired amount of layers before further modification and measurements are done. Since graphene had rather a universal absorption with absorbance depending on amount of the layers measurement with UV-visible spectroscopy can provide information about the amount of layers. UV-vis can also provide information about functionalization of graphene as oxidized graphene (GO) has higher transmittance than reduced graphene. Similar information can be obtained via x-ray diffraction as oxidized and multilayer graphene provide noticeable changes in the basal diffraction reflection.[38] Other interesting properties that could be mapped is for example the amount of doping. Useful methods to determine purity and quality are AFM and Raman spectroscopy.

It is no easy task to image plasmons as the wave vector of the plasmon waves has a large mismatch to that of free-space photons. Spectroscopic methods such as electron energy loss spectroscopy (EELS) have been utilized to overcome this task but the real-space imaging has proven rather difficult for GSPs due to their frequency being in THz range. At least scanning-type near-field optical microscopy and FTIR microscopy have been utilized to overcome this problem.

3.1 Scanning tunnelling microscopy STM and AFM

STM provides information specifically about the electronic states and structuring of graphene. For example, the Dirac points of graphene can be examined via scanning tunnelling spectroscopy, which is a variation of STM which measures changes in the tunnelling current between the tip and the sample as well as the usual topographical data STM provides. The problem with STM is that measuring properties of freestanding graphene is very tricky and usually a substrate is needed but as noted before, the substrate can easily affect the properties. STM is particularly excellent in imaging heteroatomic doping, where electrons are increased or decreased by substituting carbon atoms by nitrogen or boron atoms.[78]

AFM is originally based on scanning tunnelling microscopy (STM) and can be used to map mechanical properties of various types of nanomaterials just like STM. It is particularly handy in imaging graphene, as it can detect ripples and other defects as well as impurities on top of graphene with a very good resolution. In addition to topographical

mapping AFM is a versatile tool to study all kinds of physical properties for example the thickness of the graphene layers and Young's modulus provided that a specific tip is used.

In contrast to STM, AFM measures the interaction between a probing tip and sample. A very sharp tip is attached to a cantilever and positioned above the sample. The tip moves according to the interacting force between sample and the tip. If tip is too close, the force is repulsive and if it is at a sufficient distance, the force is attractive, in accordance with Pauli repulsion. Repulsive force pushes the cantilever upwards, this is the working-principle of contact mode AFM, and attractive force bends the cantilever towards the sample, which works for non-contact AFM measurements. These slight changes in position in turn affect the reflectance of a laser beam pointed directly at the cantilever. A detector measures even the smallest changes of position in the reflected beam path and amplifies them. Either the tip or the sample can be moved in regards to one another, providing a force map for the area the tip/sample moves. This movement is done via piezo-electric scanner that can move the tip or the sample in all three dimensions. All measured data is fed to a feedback loop that assures that the cantilever follows predestined set points. This can for example, protect the tip from crashing the sample which destroys the tip and can harm the sample.[79] The working principles of AFM are presented[80] in Figure 17.

The tip and cantilever material as well as the measurement type should be carefully chosen for each measurement specifically.

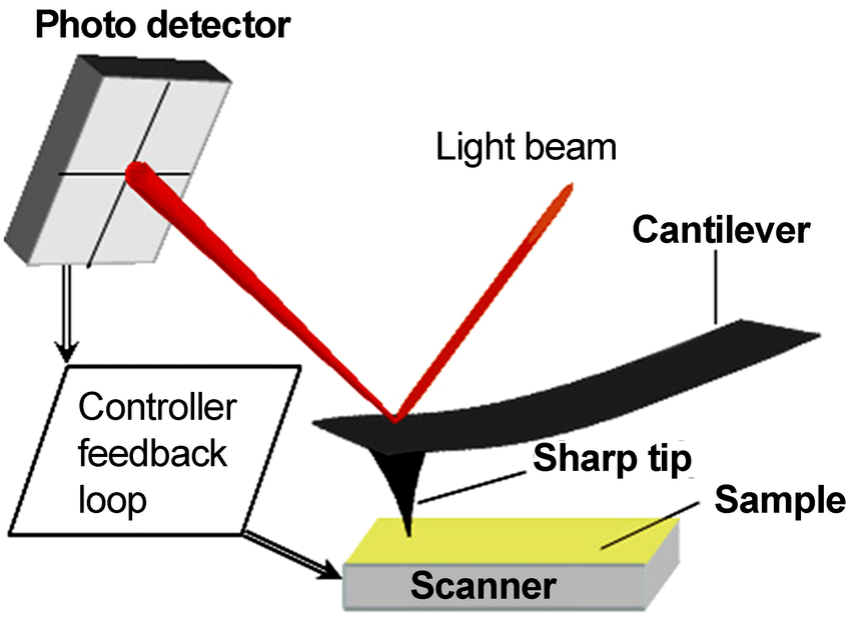

Figure 17. Schematic of AFM working principle. Reprinted with permission from ref. (80).

3.2 Raman spectroscopy

Raman spectroscopy as well as IR-spectroscopy in the next chapter, study and probe the molecular vibrations of matter. Raman spectroscopy measures the energy of the light that hits the sample and the energy of light after it has interacted with the sample. In Raman scattering the photons scatter inelastically, which means that energy is either gained or lost in the scattering event. If the photon emitted in the relaxation of molecule from its excited state has more energy than the exiting photon, the phenomenon is called Anti-Stokes scattering. When the exciting photon has more energy than the emitted photon, the phenomenon is called Stokes scattering. In Raman scattering the exiting photon excites the molecule to a virtual state, which is a quantum mechanical undetectable intermediate state. In Stokes scattering, as the energy of emitted photon is lower than the exciting photon, the system relaxes from a virtual state to a vibrational state above the ground state. In Anti-Stokes scattering the excitation starts from an excited vibrational state and relaxation ends in the ground state. All this alone is not enough for the vibrations to be detectable. A dipole moment is induced in the molecule by the electric field of the exciting light. The dipole moment depends on the polarizability of the molecule and the dipole moment deforms the electron cloud of the molecule so that it vibrates in a characteristic frequency for either Stokes- or Anti-Stokes scattering. There is also a third type of scattering called Rayleigh scattering, which is elastic scattering. The intensity of measured scattered light depends on the differential scattering cross section, which highly depends on the incident light and Boltzmann factor. It also depends on the polarizability as the molecules with high polarizability have higher scattering intensity.[81]

For graphene Raman is mainly used to study the purity of manufactured graphene and to determine the amount of layers. As mentioned before, graphene has four vibrations, only one of which is Raman active and none IR active. The Raman active vibration is a double degenerate optical vibration, consisting of transverse and longitudinal optical modes, situated in the centre of the Brillouin zone, in which the carbon atoms of the graphene sheet move in graphene plane. This vibration is expected to be visible near 1587 wavenumbers for single-layer graphene. This is called the G-band. For multi-layer graphene the G-band location red shifts slightly to 1581 wavenumbers and the intensity increases.[16,82] G-band is the only band that comes from first-order Raman scattering and all the other come from second order Raman scattering. In first order Raman a photon excites an electron to excited state and a phonon scatters it to the virtual state from which it decays emitting a photon characteristic to Raman scattering. In second order Raman the

excited electron is scattered twice before decaying either by two phonons or a phonon and a defect.[83]

Other prominent features in the graphene Raman spectra are G'-band around 2700 wavenumbers and D-band around 1350 wavenumbers. As can be seen, the frequency of G' –band is approximately double of that of the D-band. That is why sometimes the G'-band is also called the 2D-band. The *K* point of the Brillouin zone and phonons in its vicinity are especially important for D- and G'-band formation. The G'-band stems from two in-plane transverse optical phonons scattering the excited electron near the *K* point in the Brillouin zone and the D-band from one in-plane transverse optical phonon and a defect scattering the electron. The frequency of both G'-band and D-band changes as a function of the incident light. One more peak can be visible in the Raman spectra of graphene but is often nearly undetectable. This peak is called the D'-band which is around 1620 wavenumbers and can often be overshadowed by the G-band. As per the notation D, the origin of this band is also in defects in the graphene. D'-band is created by intra-valley double resonance which connects two points in the same circle around the *K* point of the Brillouin zone, one being a defect and one being in-plane longitudinal optical phonon.[82] The mechanism behind the creation of each band and a typical Raman spectrum of graphene is presented in Figure 18.

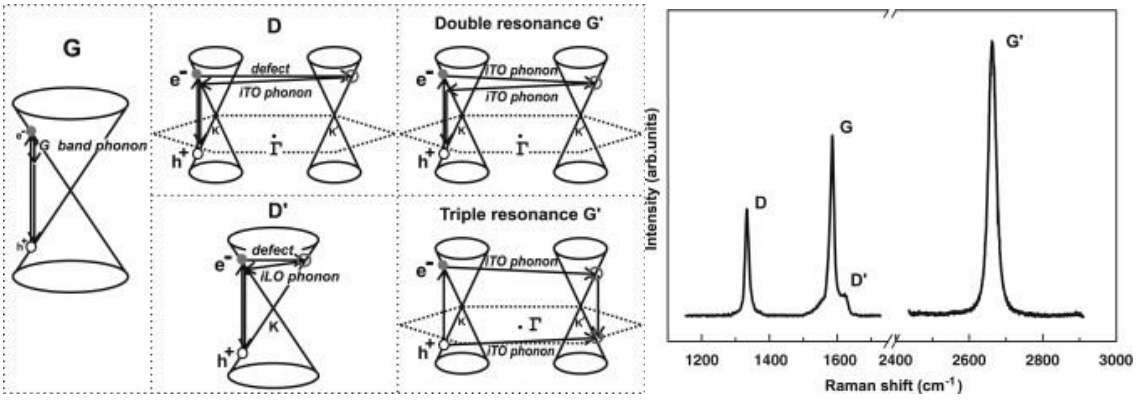

Figure 18. Above: Mechanism behind creation of all band in graphene Raman spectrum. Below: Typical Raman spectrum of graphene. Reprinted from reference (51). Copyright 2019, with permission from Elsevier.

3.3 FTIR microscopy

FTIR-microscopy is a variation of FTIR spectroscopy, which utilizes IR-lamp to study the vibrations in molecules. Molecular vibrations that include a change in dipole moment are infrared active and can be detected with IR-spectroscopy as they vibrate in the same frequency as IR radiation. FTIR microscopy differs from normal FTIR spectroscopy as a microscope is used to focus the laser beam in a desired area. Apertures are used to limit the measurement area and two kinds of measurement modes: transmission and reflectance can be utilized. FTIR devices exploit interferometry, most often the Michelson interferometer, where a laser beam is split into two beams that travel through their own movable mirrors until they meet again at one point and interfere with one another.[84] The working principle of FTIR microscope is presented[85] in Figure 19.

As mentioned before, graphene has rather universal absorption of 2.3 % for EM-radiation, so it does not really absorb any IR radiation and symmetrically the only active vibration is Raman active. Therefore, the IR spectrum of pure graphene is rather redundant to measure. This is problematic, as many auspicious applications of graphene plasmonics require higher absorption. However, with introduction of plasmons in graphene, the IR-absorption changes. The plasmons can tap into the molecular vibrations sort of like a harmonic oscillator and enhance them. Plasmons can also be detected on their own as they interact with light when they are excited. The problem with this method is that graphene plasmons are supposed to be in the THz region, which is hard to reach as feasible measurement range often goes only to 650-700 cm^{-1}.[86]

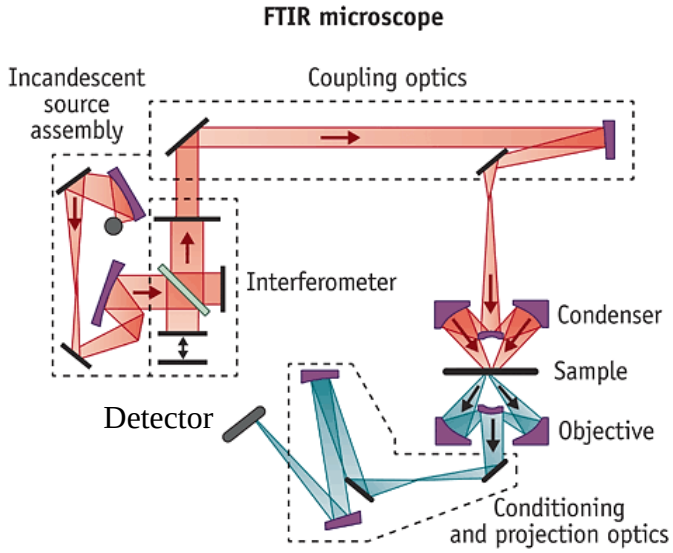

Figure 19. Working principles of FTIR microscopy. Modified with permission from ref. (85).

3.4 SNOM

Scanning near-field optical microscopy or SNOM is also a prominent tool in graphene plasmon characterization. Near-field optics in general are a solution to diffraction limitations of conventional microscopy methods. Sub-wavelength aperture or scatterer, such as nanoparticle is used to interact with passing EM-radiation, which results in evanescent waves confined in sub-wavelength distance. In near-field range these waves can give highly resolved spatial, spectral and temporal information. Therefore, the resolution depends on the size of the aperture/scatterer instead of the wavelength of the light used, as it does in conventional and far-field microscopy. This allows resolution of only tens of nanometres instead of that of 200 nm in conventional light microscopy.[87]

Just like in AFM, SNOM also requires a piezo-electric scanner that moves the sample or the light source in order to scan the whole sample. In fact, AFM can be used as a basis for SNOM or with it as a combination. A tip, similar or identical to those used in AFM measurements, is used as a scatterer for incident laser beam. The tip scatters the light enhancing the local field to be about 10-100 times stronger. Now the tip functions like the aperture, determining the resolution and being the source of the near-field evanescent waves that are scanned over the whole sample. This method is also called scattering type SNOM or s-SNOM.[88] Schematic of both aperture and tip configurations for SNOM are presented in Figure 20.

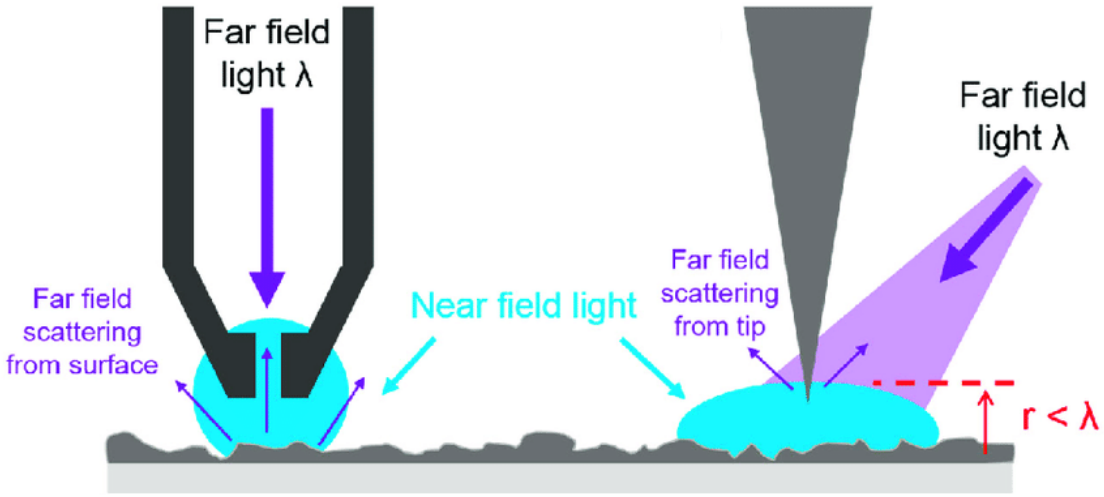

Figure 20. Near-field effect and configuration both from the aperture and tip configuration of SNOM measurements. Modified with permission from ref. (88)

The advantage of SNOM is that it can both induce and detect plasmons in graphene even without any introduced structure such as corrugation. When scattering amplitude is measured in a s-SNOM experiment and normalized, the near-field amplitude is obtained. Plasmons can now be detected as they change the local electric field under the scanning tip and this changes the near-field amplitude.[22] As Plasmons reflect from the edges of the structured or impurities, they interfere with the field producing fringes in the measurements.[68] An image of graphene plasmons measured with SNOM[89] is presented in Figure 21.

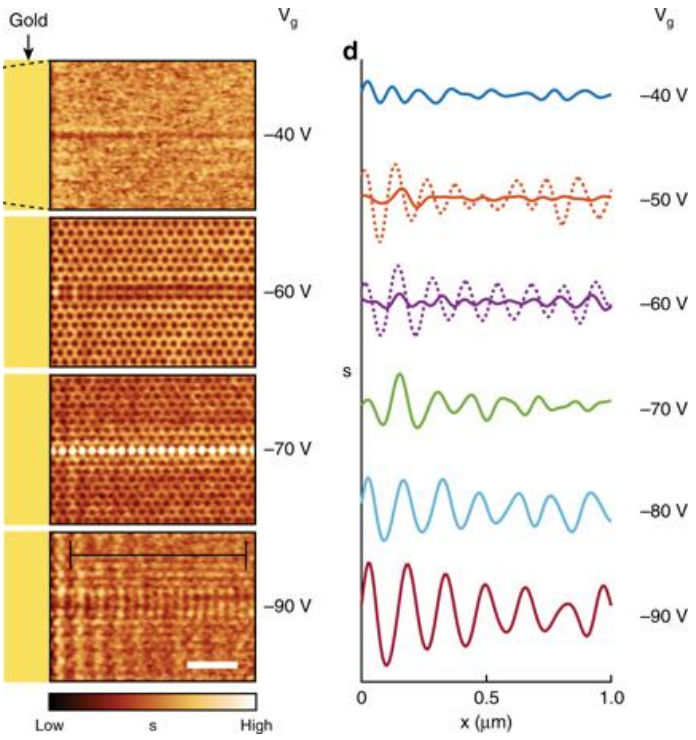

Figure 21. On the right: Experimental near field amplitude SNOM images at different gate-voltages at 60 K temperature. Plasmons are launched by gold bar on the left. On left: Line profiles from the images on the right.
Modified with permission from ref. (92).

4 Applications of graphene plasmonics

Terahertz gap is a term coined for the lack of electronics and optics in the terahertz spectral range situated between infrared and radio waves. There are practically no devices capable of producing or detecting terahertz radiation even though there is a large demand. Terahertz detectors would be particularly useful in biological and medical applications as it is not intrusive or harmful for tissue and the field of telecommunication could benefit

from the applications as well. [90] Graphene is a promising matter for terahertz applications because its plasmons are located in the FIR and terahertz region, making their applications work in this range as well. Other promising aspects of GSP applications lie in medicine and security as THz radiation is non-destructive for biological systems.

4.1 Optics

Graphene could, in theory, be used as a medium for terahertz lasers as population inversion can be achieved either via optical pumping, carrier injection or plasmons. Plasmonic population inversion happens almost exactly as stimulated emission normally works with photons. A plasmon travels on a graphene sheet and couples to an interband transition. A population inversion happens and as a result, two plasmons of equal properties are emitted. This results in large gain in the plasmons, even larger than stimulated emission of photons for normal laser could achieve, due to strong confinement of light in 2D materials.[91] An image depicting the phenomenon is presented in Figure 22. However, as more plasmon gain is achieved, the plasmon mode dephases more strongly eventually disabling the method from being used for THz lasing.

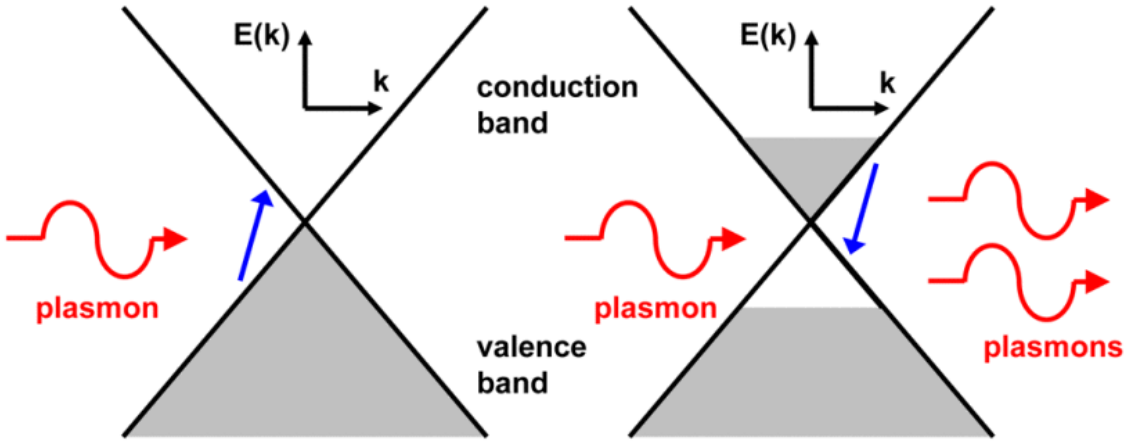

Figure 22. Stimulated emission of plasmons in graphene. Reprinted with permission from ref (91).

Graphene plasmons can also be used to tune existing terahertz lasers. By modifying the Fermi energy of graphene, the round-trip gain inside already existing laser cavity can also be tuned. The plasmonic structure inside the cavity tunes the frequency and can amplify

the resonant modes, therefore affecting the emission exiting the laser cavity. Adding the plasmonic structure has also been shown to increase the amount of lasing modes compared to conventional gain modulators.[92] Image of these effects are presented in Figure 23. GSPs in population inverted graphene can experience large gain because of the stimulated emission affecting the plasmons in the terahertz range as previously mentioned. Because of this, very compact terahertz amplifiers or resonators can be created.[93]

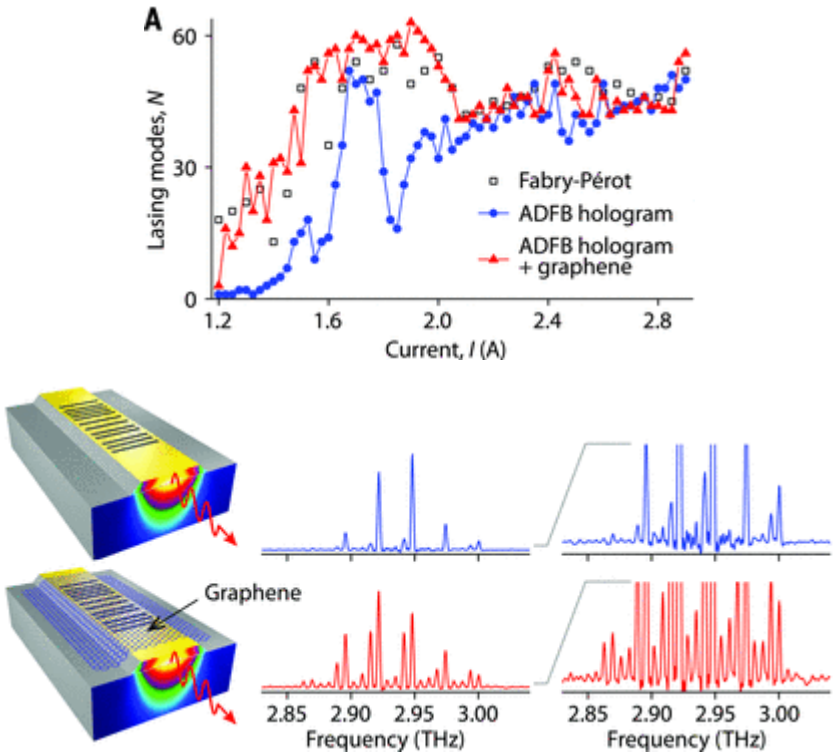

Figure 23. The effect of GSP gain modulator on the amount and the frequency of the lasing modes. Modified with permission from ref. (92)

The high confinement and tunability of GSPs make them a prime material for wave-guiding, as the wave propagation can be modified simply by applying gate voltage or changing the structure of the graphene, as it the whole goal in this thesis. One application for such shaped waveguides is a Luneburg lens, which is a 2D lens that changes its refractive index radially from centre to the edge of the lens. Such lenses can be used for example in radar technology.[94] The same property of being electrically tunable makes GSPs good material for optical modulators and polarizers. Theoretically with all of these component, a completely plasmonic graphene circuit could one day be realized.[52] Graphene supports several nonlinear optical processes as mentioned in the optical properties chapter. Graphene can be used as a saturable absorber, a device which filters

out weaker intensity modes from the round-trip inside the laser cavity, for mode-locking in ultrafast lasers.[95] Image of such absorber and its effect on the laser beam is presented in Figure 24.

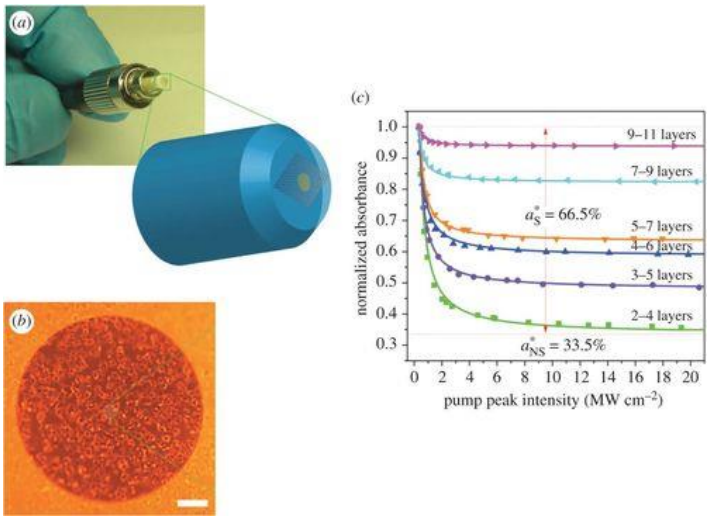

Figure 24. A GSP saturable absorber. Reprinted with permission from ref. (95).

4.2 Sensors and detectors

Surface enhanced Raman spectroscopy or SERS is a version of Raman spectroscopy that tries to overcome all the typical disadvantages or faults of ordinary Raman spectroscopy by introducing an enhancement substrate that can enhance the Raman scattering either chemically, usually via charge transfer, or electromagnetically. SERS is also capable of detecting even trace amounts of compounds and the enhancement factor compared to the basic Raman spectroscopy can be as high as 10^8. Graphene is an ideal material for SERS due to its large surface area and good ability to absorb molecules. Several graphene SERS applications are based on the chemical enhancement of the scattering but via LSPRs the option of EM enhancement becomes available as well. The EM enhancement for SERS in graphene works best when combined with metallic nanoparticles. This is due to graphene being able to protect the nanoparticles from oxidation while eliminating the fluorescent background and providing a large flat area capable to support more nanoparticles and enhance their plasmonic modes.[96] An image of a realized application[97] of GSP nanoparticle hybrid SERS is presented in figure 25. Carbon based enhancement substrate could be integral for biological applications such as cancer cell detection as carbon is not toxic.[96]

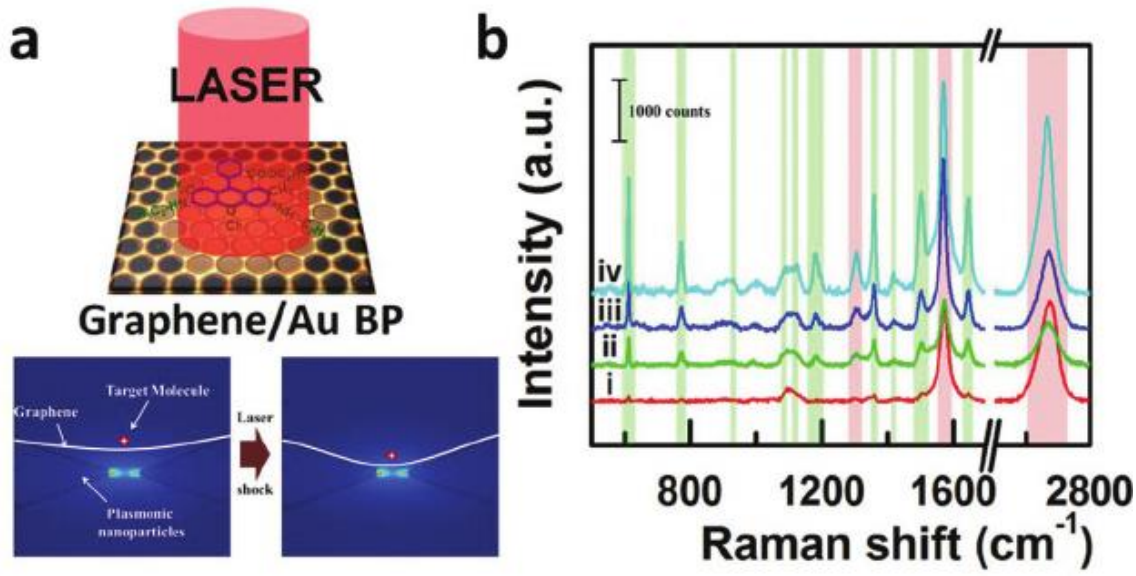

Figure 25. a) Schematic of label free detection of molecule with graphene plasmonic SERS. b) Detected changes in graphene's Raman spectra corresponding to the target molecule. (Green markings) Reprinted with permission from ref. (97).

IR measurements can also be improved via surface-enhanced infrared absorption or SEIRA. Usual FTIR measurements are very handy and non-intrusive way to detect molecules and compounds via their vibrational data but as IR light used is several orders larger than the diameter of the most common molecules, the interaction cross-section between the light and the molecule for low concenctrations is very small and thus the sensitivity rather low. SEIRA uses surface plasmons that couple with the infrared active vibrations in molecules like a harmonic oscillator.[98] This allows even traces amounts of molecules to be detected in the plasmonic field completely label free, which enables a variety of applications for example once again in biomedical field. Trace amounts of gases can be detected with SEIRA from breath which could reveal underlying diseases.[99] Graphene is optimal material for SEIRA applications as it can support tunable plasmons with high mobility and low losses and has large surface area.[98] An image of graphene plasmonic gas detector is presented in Figure 26.

As known by now, graphene has poor optical absorbance on its own but it can be enhanced with plasmons. Nanoribbons, hybrid-structures or small periodic structures can support LSPRs which have increased absorption. Similar effect can be achieved also by different substrates and electrical gating. This careful engineering of GSP structures can increase the absorbance all the way to full absorbance at least in the IR region, making graphene plasmonic devices a good candidate for THz detection.

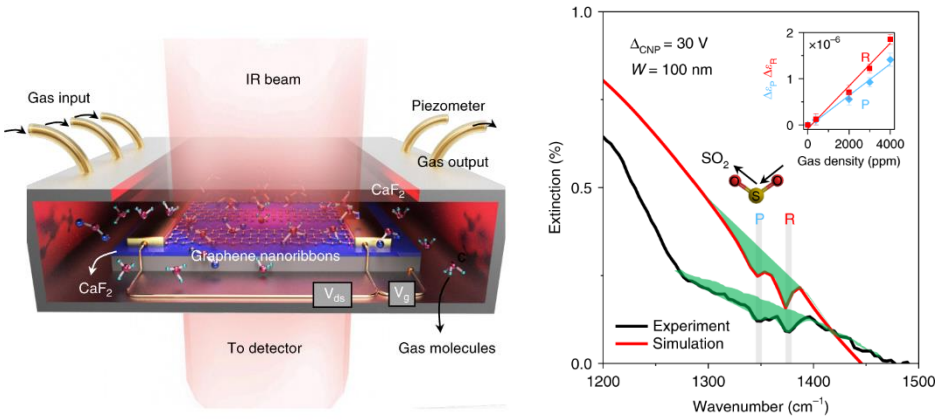

Figure 26. Left: A schematic of GSP gas detector. Right: Detected and theorized gas Raman spectrum with the device. Reprinted with permission from ref. (99)

4.3 Metamaterials

Metamaterials are carefully designed and build materials that consist of preordained building blocks which have been fitted together to form an elaborate structure. The physical properties of metamaterials do not depend on the material of the building blocks but of the structure they have been placed at. By controlling separation and periodicity of these building blocks, the behaviour of light inside the metamaterial can be tuned. Metamaterials with negative refractive index or negative phase velocity can be created by carefully planning the structure.[100] Many periodic graphene plasmon applications can be thought as metamaterials. Often GSP metamaterials consist of alternating layers of graphene and some dielectric material on top of each other or periodic gratings of graphene nanoribbons and some other material. By tuning the width of the nanoribbons, the plasmonic properties can be tuned as well, which is essentially metamaterial like behaviour.[58] Combining layered graphene-dielectric material metamaterial with periodic grid formation can be utilized to absorb unpolarized light in a wide range of angles which is essential for example for thin film photovoltaics or thermal emitters.[101] Other applications for GSP metamaterials are waveguides, and optical switches.

5 Optical forging

Graphene is a promising material for plasmonic applications due to its 2D nature, but it often needs to be restricted i.e. in forms of nanoribbons to overcome the momentum mismatch between the light and the plasmon wave vector. One other way to do this was to introduce corrugations and structures in graphene, usually by altering the substrate. Direct patterning methods are often difficult or non-reproducible particularly due to the interactions between the substrate and the graphene introducing surface adhesion that is hard to break.

Optical forging is a patterning method for two-dimensional materials that allows stable three-dimensional structures to be created on the material with high definition. The method includes using a femtosecond pulse laser in an inert gas environment. If air is used as the environmental gas, oxidation of graphene surface can happen instead of optical forging. Overlapping many small blisters enables more complex structures such as pyramids, lines and squares to be generated. This is illustrated in Figure 27. Interestingly, the first patterned points introduce strains and constraints for the following patterning blisters. If a square is produced by going spirally from inside out, the first point in the middle is whole and most visible, whereas the other overlapping blisters are not complete and seem to be affected from previous patterning.[37]

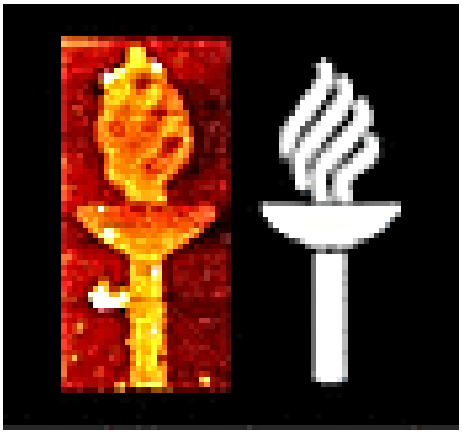

Figure 27. A 3D rendering from AFM image of optically forged torch-logo of the University of Jyväskylä next to the bitmap it was referenced by. Structure is made by overlapping single blisters. Modified with permission from ref. (37). American Chemical Society.

A radius dependent linear expansion of these structures can be given by[102]:

$$\epsilon(r) = \epsilon_0 e^{\frac{-4r^2\log(2)}{\text{fwhm}^2}}, \tag{31}$$

where ϵ_0 is the maximal expansion and fwhm is the full width at half-maximum of this laser beam. The laser is assumed to have a Gaussian intensity profile and the phenomenon to be single photon process. In the second study made on the topic of optical forging, Koskinen *et al.* (ref. 92) measured the resulted blister profiles with AFM and transformed the data into the radius dependent linear expansion and gained an expansion rate of approximately 1.5 x 10^{-3} %/s which corresponds to 22 nm^2/s growth. Plots illustrating this are presented in Figure 28. The irradiation time also affects the shape of the blisters. With short irradiation time, less than 0.4 s, structures stay flat but detectable. With irradiation times from 0.4 s to 2 s, blister-like formations with one distinct circle as formed. With even longer irradiation times several rings form until a central dome forms and the blister can completely transform into a bump. These circles have features significantly smaller than the laser beam size meaning that the optical forging is *not diffraction limited* patterning method.

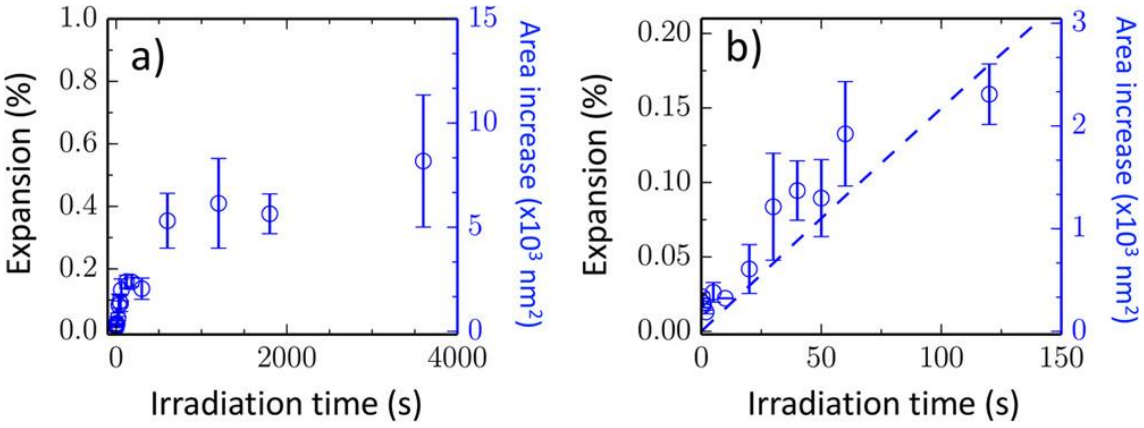

Figure 28. a) Increased area from optical forging, measured from experimental data with AFM. b) A zoom from the plot in a) for irradiation times below 150 s. The linear fit gives the expansion rate. Reprinted with permission from ref. (92).

The blister growth was simulated with classical thin sheet elasticity model to obtain more information about the factors and phenomena behind it. The model takes into account in-plane strain, out-of-plane bending and surface adhesion. Graphene sheet tries to always

minimize its energy and it seems that first thing it does to do so under irradiation is to introduce strain in the sheet. This likely results in stretched bonds and breaking some of the hexagonal structures, forming larger structures that can also be understood as point defects. After that the graphene wants to bend out of plane which creates a perfectly round ripple. The kink is circular, because creating the kink is energetically most favourable at the maximum slope $r_0 = fwhm/2\sqrt{\ln 2}$. The adhesion then pulls the sheet back towards the substrate causing ripples to be narrower and higher until it is no more energetically favourable to grow this ripple and another ripple is formed. As the adhesion depends on the interactions between substrate and the 2D material, optical forging works for other 2D materials as well, but results in ripples of different height.[102]

As this was theoretical modelling, it was necessary also to confirm that graphene actually stays mostly graphene despite some of the hexagonal structures breaking. Raman experiments on the irradiated areas reveal G- and D-band broadening and broadened background response, but the typical graphene characteristics still remain, which proves that the structures are indeed graphene. The D-band does not significantly grow higher, which would indicate graphene to be defected in larger scale. Unpatterned areas remain identical to flat graphene Raman spectra so no graphene is surely not ablated or any other materials are not deposited on top of it.[37] An illustration of the Raman spectra and a bitmap of Raman signal integrated over 2D band is shown in Figure 29.

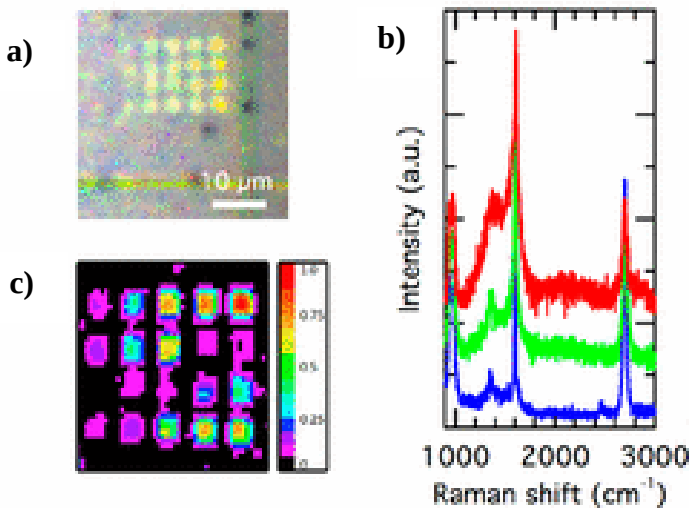

Figure 29. a) OM image of optically forged square patterns. b) Raman spectra of pristine graphene (lowest) and optically forged areas with two different irradiation times. c) Bitmap of Raman spectras integrated of the D-band. Modified with permission from ref. (37). Copyright (2019) American Chemical Society.

EXPERIMENTAL PART

6 Methods

The experimental section of this work consists of patterning, characterization, and FTIR measurements to detect the plasmons. The patterning was conducted via optical forging. Characterization was done with optical microscopy and AFM and the SP measurements were conducted with FTIR microscopy. The used optical microscope was Olympus BX51M. The AFM device was Bruker Dimension Icon AFM Device 2016. The AFM measurements were conducted with the NanoScope 9.1/9.4 program in mechanical properties mode with quantative nanomechanical mapping in air. The optically forged areas were also compared with oxidized areas done with the same setup as optical forging but without inert gas environment. These structures were also characterized with AFM and Raman. Used Raman device was Thermo scientific DXR Raman microscope.

Optical forging was done with home-built femtosecond setup that consists of amplified femtosecond laser (Pharos-10, 600 kHz, Light Conversion Ltd.), optical microscope with camera for navigating and nano-positioning system (Nanomax 300, Thorlabs Inc.) and two non-collinear optical parametric amplifiers (NOPA, Orpheus-N, Light Conversion Ltd.). Sample was placed in an airtight chamber and inert gas, in this case nitrogen, was lead to the chamber. Inert gas environment prevents sample from oxidizing instead of optical forging. The femtosecond beams were focused on the sample with microscope objective (Nikon Lu Plan ELWD 100x/0.80).

The FTIR measurements were performed with Nicolet iS50 FT-IR spectrometer that was combined with Spectrum Spotlight IR-Plan Advantage Imaging System microscope. The system was able to measure 4000-700 cm^{-1} with good resolution. Nitrogen gas was used to purge the system and the microscope detector was cooled with liquid nitrogen. Measurements were conducted in the reflectance mode. A gold mirror was used as a background for all measurements. Measurements were done with Omnic program.

6.1 Sample preparation

A few differently prepared samples were used in the experiments of thesis. The main sample (sample id. VMH395) was a single-layer sheet of graphene deposited on Si/SiO_2 substrate. Ingrained in the substrate was also a metal (30 nm chrome) grid, which makes navigating in the sample easier. The graphene sheet was fabricated with CVD on top of a copper sheet which was evaporated on top of a sapphire crystal. This sort of CVD substrate or catalyst ensures optimal copper and graphene seed generation during CVD. PMMA was deposited on the graphene sheet by spin-coating and baking on hotplate and it was used to transfer the graphene sheet from copper by etching the copper away. The PMMA with graphene was deposited on Si/SiO_2 substrate and the PMMA was removed with acetone and isopropyl alcohol and the sample was dried with N_2 gas. Finally, the sample was annealed again to ensure the purity of the surface. An OM image of the sample is presented in Figure 30. The substrate was manufactured by Jyrki Manninen and the graphene was grown by Vesa-Matti Hiltunen. CVD parameters and after-transfer annealing parameters are presented in table 2.

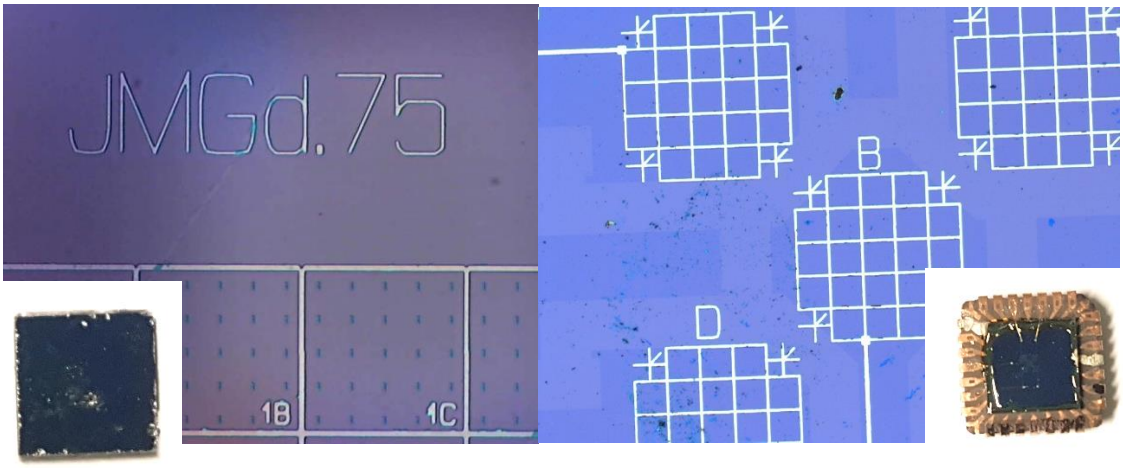

Figure 30. Left: Image and an OM image of sample VMH395. Right: Image and an OM image of sample GNR PLM A4.

Table 2. CVD and annealing parameters for the main sample (VMH395)

CVD	
Temperature (°C)	1090
H_2 gas flow (cm^3/min)	30
Ar gas flow (cm^3/min)	470
Ar/CH_4 mix gas flow (cm^3/min)	2
CVD annealing time (min)	43
Growth time (min)	7
ANNEALING	
Temperature (°C)	300
H_2 gas flow (cm^3/min)	30
Ar gas flow (cm^3/min)	400
O_2 gas flow (cm^3/min)	400
Time (min)	60+60

The main sample was used for optical forging and the gold nanoparticle (GNP) deposition. One similarly prepared sample with rather bad quality graphene sheet was used to test different conditions for the GNP deposition before the optimal method was found. Another type of sample with electrodes was used for oxidization of graphene for reference measurements. This sample (sample id. GNR PLM A4) was prepared for Alexander Plyushch, who tried to detect plasmons with bias-voltage dependent FTIR from graphene nanoribbons milled with helium ion microscope. The sample was meant to be used for bias voltage measurements of the IR response for the optically forged areas as well. This was not done as Alexander could not detect plasmons in his structures even though this was already predicted by literature[103] and the conditions for optical forging were suboptimal. This sample was also single layer graphene grown via CVD on top of copper on sapphire. The transfer was done with PMMA similarly as with the main sample to Si/SiO_2 substrate. This sample has different sort of grid-system as it was divided into 5 smaller grids as the sample has electrodes. OM image of the grid formation is presented in Figure 30. The grid consisted of 5 nm titanium as adhesion layer with 95 nm of palladium on top. After PMMA was removed new layer of PMMA was added and the

graphene sheet was patterned with oxygen plasma etch so that the 5 different grids were not connected to one another. PMMA was once again removed and the sample was annealed. This sample was prepared by Jyrki Manninen. The CVD and annealing parameters are presented in table 3.

Table 3. CVD and annealing parameters for GNR PLM A4

CVD	
Temperature (°C)	1060
H_2 gas flow (cm^3/min)	30
Ar gas flow (cm^3/min)	470
Ar/CH_4 1% mix flow (cm^3/min)	5
CVD annealing time (min)	30
Growth time (min)	10
ANNEALING	
Temperature (°C)	300
H_2 gas flow (cm^3/min)	30
Ar gas flow (cm^3/min)	470
Time (min)	120

Both samples were inspected with OM and AFM to determine optimal forging/oxidizing areas inside the reference grids. For VMH395 squares 2B, 3F, 4E and 4F were chosen for optical forging. The best areas for oxidization in GNR PLM A4 were grid B row 2 squares 4 and 5. OM and AFM images of 3F square are presented in Figure 31. AFM images all of the chosen squares before patterning are presented in appendix 1.

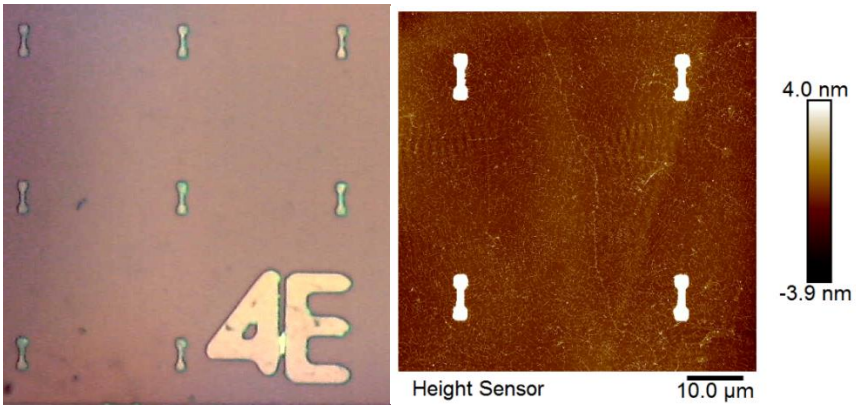

Figure 31. On the left: OM image of square 4E, on the right: AFM image of square 3F.

6.2 Optical forging and oxidizing

Two blister matrices with different irradiation times and a line grid was patterned on VMH395 square 2B. In addition, three higher blisters were inscribed near the corners of the patterned areas to help navigation in FTIR measurements. These blisters were irradiated for 900 s per each spot. Illustrations of patterned areas are show on Figure 32. Irradiation parameters are presented in table 4.

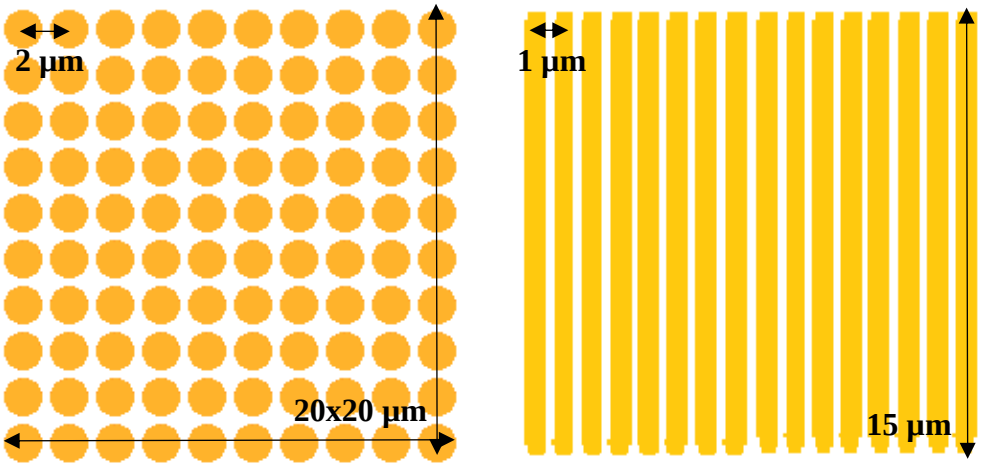

Figure 32. Left: Illustration of the blister matrix on VMH395 square 2B. Right: Illustration of the line grid on square 2B.

Table 4. Optical forging parameters for structures in VMH395 square 2B

General info	
Laser pulse energy (pJ)	60
Atmosphere	N_2
Blister matrix 1	
Irradiation time (s/spot)	10
Separation between spots (µm)	2
Blister matrix 2	
Irradiation time (s/spot)	30
Separation between spots (µm)	2
Line grid	
Irradiation time (s/spot)	10
Separation between spots (nm)	250
Separation between lines (µm)	1

During patterning the sample was slightly drifting which can be seen in the structures as the blisters all look to be slightly slanting to one direction and the lines are not evenly spaced. Also, during the patterning of the line grid an electric break occurred and momentarily disturbed the atmospheric control in the room, which resulted in two higher lines. Patterned areas were characterized with AFM microscope. An AFM image of the line grid is presented in Figure 33. The rest of the AFM images of the optically forged areas are in the appendix 2. Obtained AFM images were adjusted with NanoScope 1.9 program. Flattening was used to emphasize the difference of the background to the actually desired higher areas. Similar manipulation was done to all AFM images in this thesis. A cross-section of each structure is presented in Figure 34. The height of the 10 s blisters was around 4.9 nm and the 30 s blisters were around 6.5 nm. The general height of the lines was divided into three parts. The three lines before the two higher lines were around 10 nm tall, the two tall lines were 12 nm tall and the rest of the lines were about 8.8 nm tall.

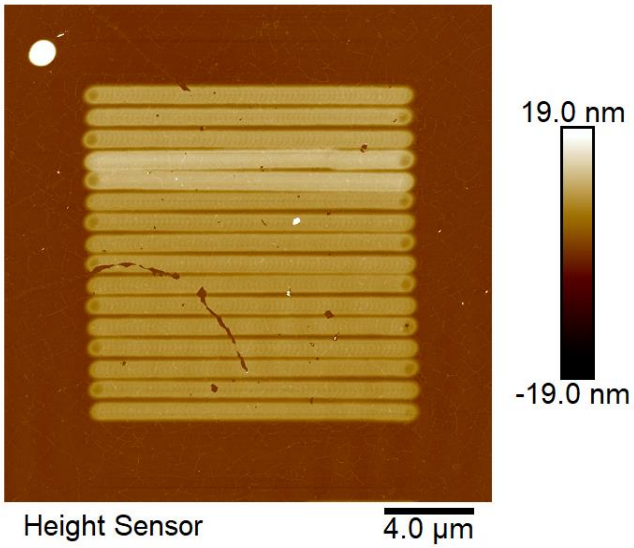

Figure 33. AFM image of optically forged line grid in VMH395 square 2B.

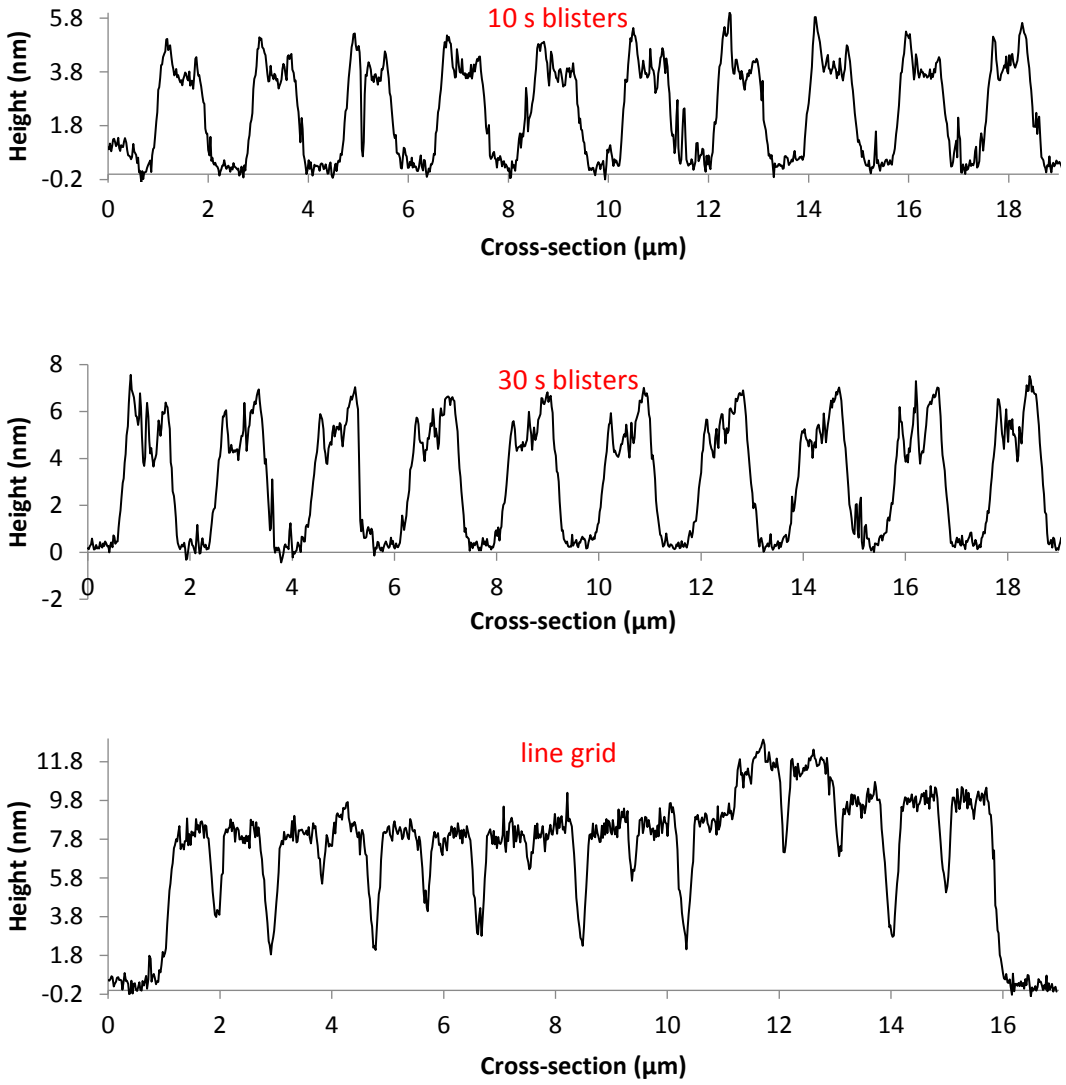

Figure 34. Cross section of structures in the VMH295 square 2B.

After several calibration measurements with the FTIR microscope, it was determined that the smallest aperture size that still produces feasible signal for measurements is 30x30 µm. Therefore, larger patterns than those irradiated on square 2B were needed to fill the full aperture area. Previously selected squares 3E, 4E and 4F were patterned with 30 x 30 µm blister matrix, 30 x 30 µm line grid and 30 x 30 µm frames. The frames were done because the corners could have interesting geometries and symmetries for plasmons. As the patterns were so large, they needed to be inscribed in four parts, which made fitting the four parts into each other rather tricky. Patterns were divided into four parts by dividing it from the middle from up to down and from left to right. Schematics of these patterns as well as their division to 4 areas are presented in Figure 35 and the AFM image of blisters in square 3F is presented as an example in Figure 36. Conditions for each pattern are presented in table 5. The height of blisters in square 3F was about 3.5 nm, the

lines were about 4.2 nm and the frames were around 4.4 nm, although the upper right corner was slightly higher than the other areas in the pattern (5.5 nm). Cross sections are presented in Figure 37.

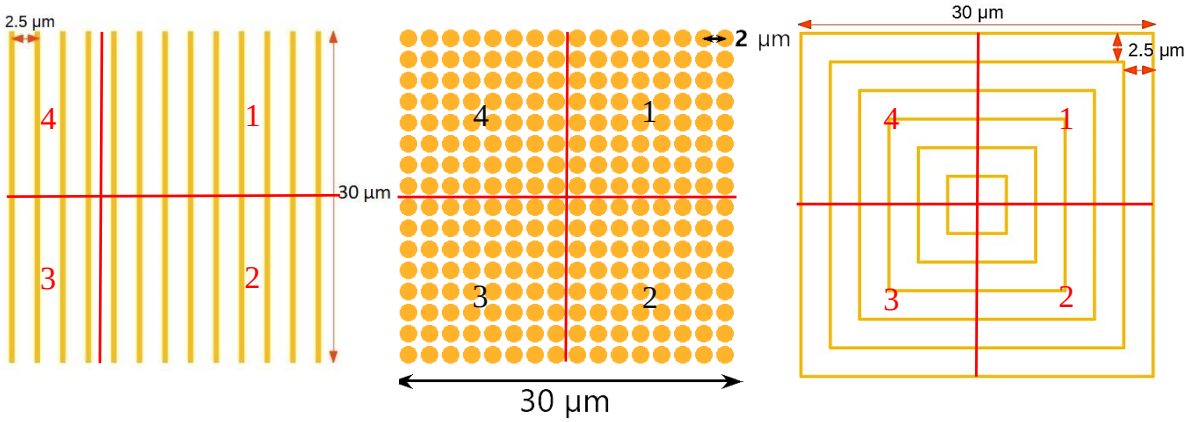

Figure 35. Inscribed patterns from left to right: 3E line grid, 3F blister matrix and 4F frames.

Table 5. Optical forging parameters for structures in VMH395 squares 3F, 4E and 4F

General info	
Laser pulse energy (pJ)	50
Atmosphere	N_2
Blister matrix (3F)	
Irradiation time (s/spot)	60
Separation between spots (µm)	2
Line grid (4E)	
Irradiation time (s/spot)	10
Separation between spots (nm)	250
Separation between lines (µm)	2.5
Frames (4F)	
Irradiation time (s/spot)	10
Separation between spots (nm)	250
Separation between frames (µm)	2.5

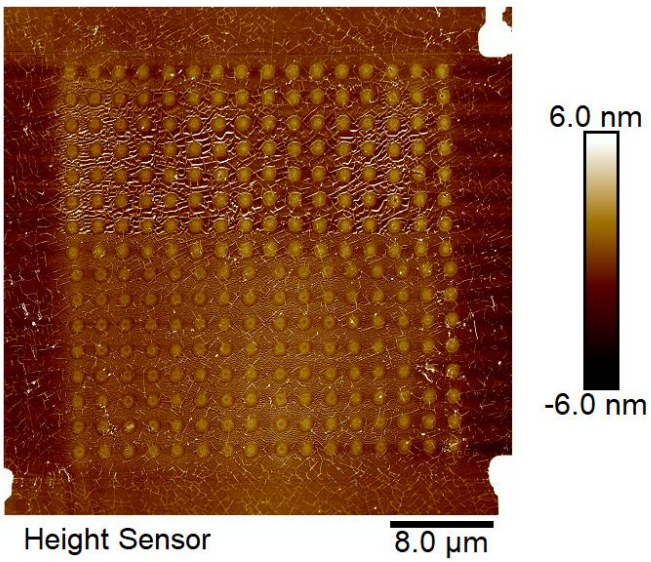

Figure 36. AFM image of optically forged blister matrix in VMH395 square 3F.

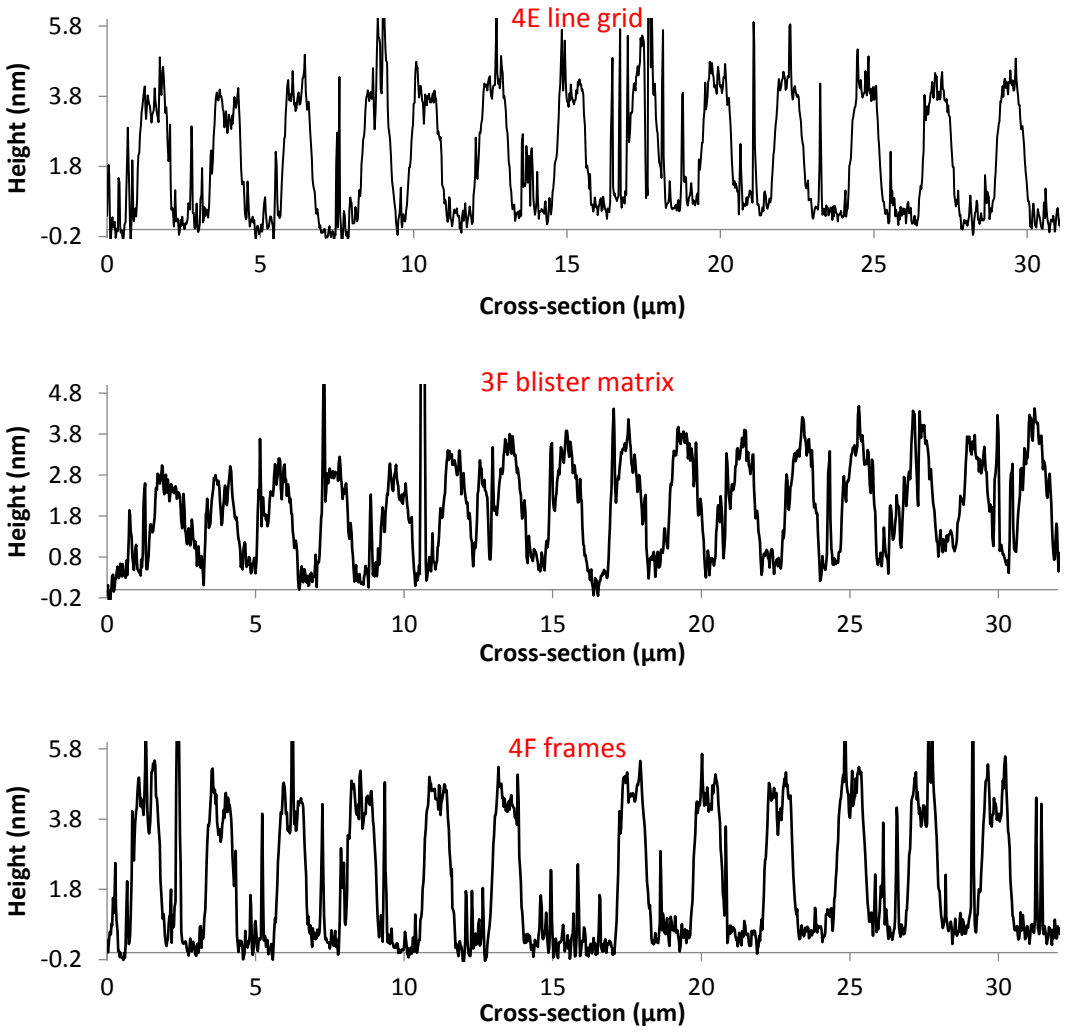

Figure 7. Cross sections of structures in VMH395 squares 3F, 4E and 4F.

There seemed to be a slight issue with optical forging. The structures do not seem to rise high enough or at least did not rise as they had in previous experiments. The problem with this is that the patterns may not be high enough to trap plasmons or enable their introduction in FTIR microscopy experiments. Obtained structures only rose to 5-10 nm in all structures, excluding the marker points in corners of structures in square 2B. Their heights were around 30 nm but patterning a whole blister matrix let alone the line grid with the same intensity and irradiation time per blister would take far too long to be sensible. Longer patterning time also enhances the possibility of shifting. In previous experiments, the structures[37] were 20 nm and in my bachelor's thesis as high as 24 nm in one of the blisters. A picture and cross-section of the highest pattern in my bachelor's thesis is presented in Figure 38. The most likely cause of dwarfism of the patterns is air humidity. Although the patterning room is temperature and humidity controlled there seems to be correlation with the time of the year the patterns are made. In the winter and spring, when the air is dryer, patterns can rise as high as in Figure 38, but during hot and humid summer/autumntime they do not.

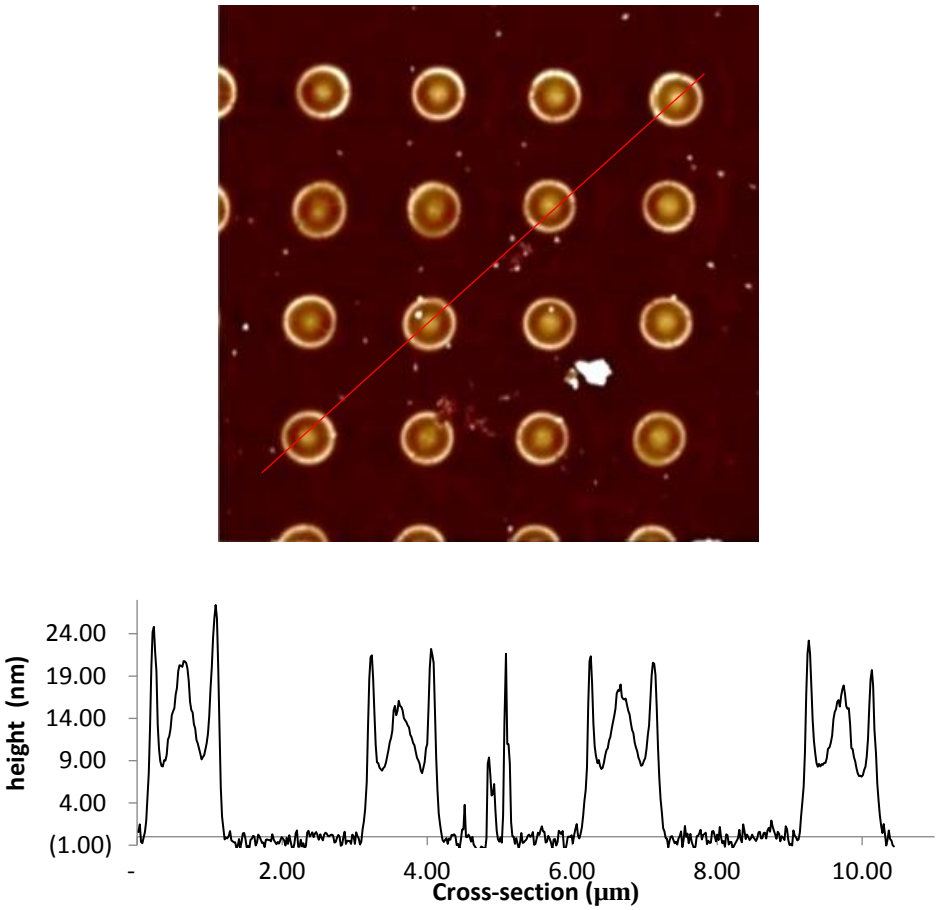

Figure 38**.** Above: Reference blisters from one of the best structures in my bachelor's thesis. Below: Cross-section of the reference blisters.

The oxidized areas were 15x15 µm, therefore they are not expected to have a different signal in FTIR due to insufficient measuring area. Two different areas were patterned, and both could be seen with AFM although measuring them was rather tough as GNR PLM A4 sample had a lot of impurities and trash on top of it, which affected the adhesion. AFM images showing the difference of the oxidized areas between normal graphene are presented in Figure 39 and oxidization parameters are presented in table 6. The oxidized areas can nevertheless clearly be seen in the AFM images as slightly higher areas that seem to be covered in some small fuzz. This is also clearly visible in the images presented. The areas are not high enough to be decisively measured from the AFM images. The longer irradiation time has produced more uniform covering of the sample, where as the smaller irradiation time seems to have produced lines and islands of these oxidized areas, which is to be expected.[36] AFM images of the oxidized areas are in appendix 3.

Table 6. Oxidization parameters for structures in GNR PLM A4 row 2 squares 4 and 5

Row 2 square 4	
Irradiation time (s/spot)	0.3
Separation between spots (µm)	0.1
Laser energy (pJ)	25
Row 2 square 5	
Irradiation time (s/spot)	0.2
Separation between spots (nm)	0.1
Laser energy (pJ)	30

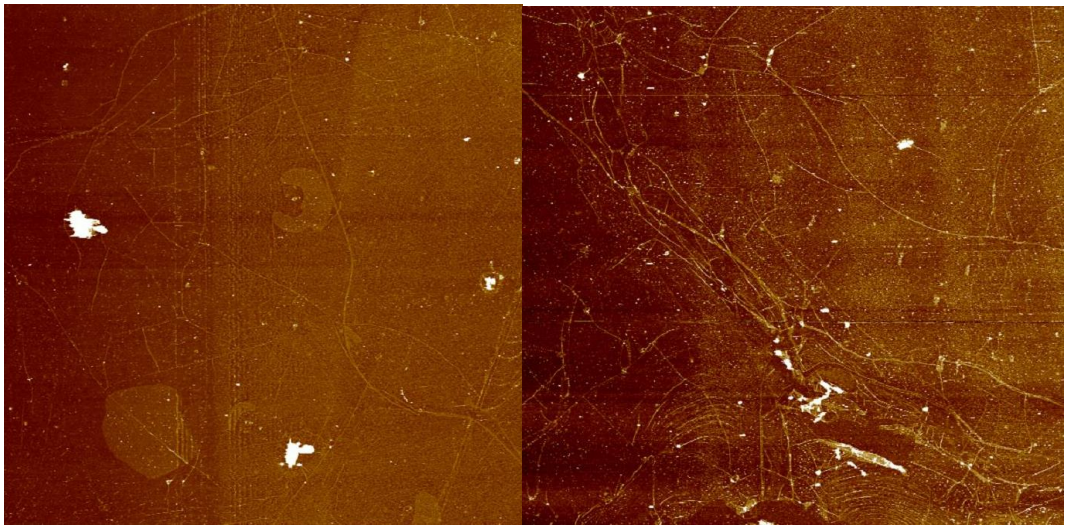

Figure 39. A closed up of AFM images taken of oxidized areas in row 2 squares 4&5 of sample GNR PLM A4. On the left 0.3 irradiation time and on the right 0.2 s.

Oxidized areas were also characterised with Raman spectroscopy, used resolution was 3 µm, to verify that the D-band rises in the graphene Raman spectra, which is a tell-tale sign of oxidization. This is indeed the case as can be seen from the Raman spectra presented in Figure 40. Heat maps of the Raman spectra integrated over D-band for the whole measurement area are presented in Figure 41. Oxidized areas have same shape and slightly lower overall signal all the way in the spectra, but the D-band response is significantly higher at least for the 0.3 s irradiation time. Both of the oxidized areas can also be seen in the Raman heat maps as slightly larger concentration of blue squares. All Raman data of oxidized areas is presented in appendix 7.

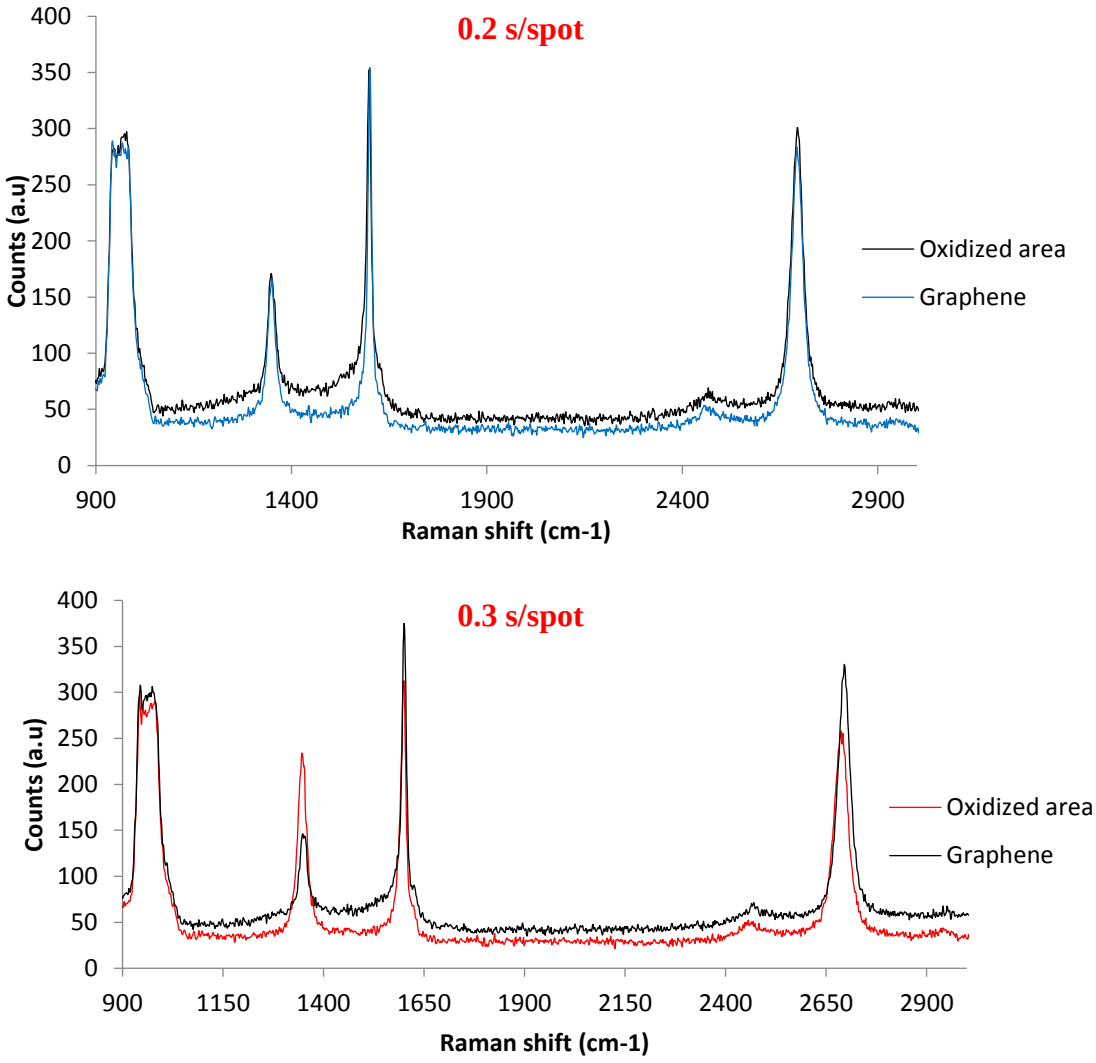

Figure 40. Raman spectra of 0.2 and 0.3 s irradiation time oxidised areas.

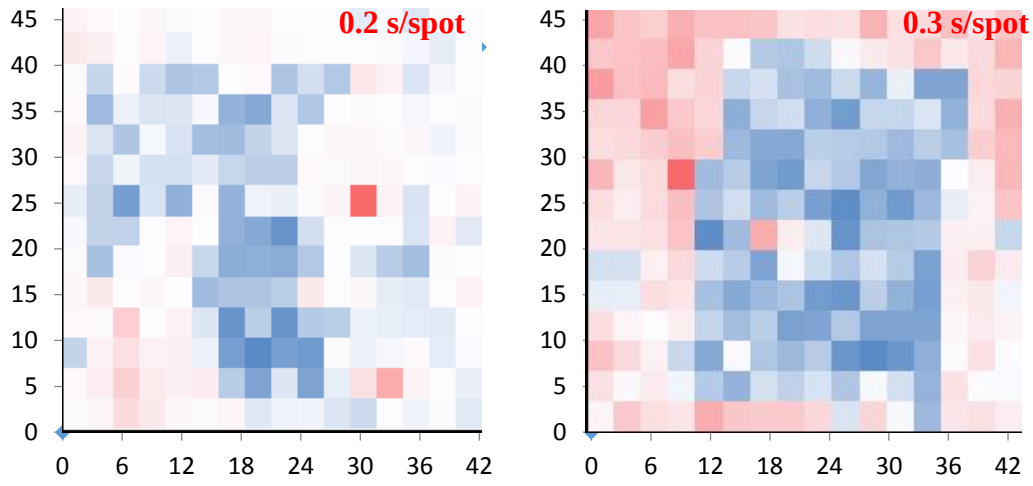

Figure 41. Heatmaps of Raman spectra of every pixel on measurement area integrated over the D-band.

6.3 Gold nanoparticle deposition

Citrate covered GNPs were deposited on patterned chips to see if they could act as antennas for plasmonic resonances in graphene. Before the actual samples were coated, several different methods of deposition were tested on unpatterned samples (VMH497 and VMH498) to ensure optimal coating. These chips were chosen for testing due to their unwanted characteristics for optical forging. Ville Saarnio provided the gold nanoparticles and ICPMS data on the nanoparticles. This data is presented in table 7.

Table 7. ICPMS data on GNPs used to coat the chips

Measurement Date
26.09.2018
Most common diameter (nm)
52 ± 1
Average diameter (nm)
55 ± 1
Particle concentration (1/g)
$(9.5 \pm 0.4) \cdot 10^{10}$

VMH498 was first spin-coated once for 120 seconds at 2000 rpms with few drops of gold nanoparticle solution. As nothing was visible with OM a different approach was taken. Few drops of GNP solution were placed on the chip and it was left to dry overnight. After examining the results with OM, it became clear that there were some impurities in the GNP solution and deposition via this method resulted in too thick layer of GNPs, as crystalline structures were visible via OM and the surface was sort of rainbow-coloured, oil-slick-like layer. The chip was washed with deionized water to get rid of the salt-crystals and excess dried GNP solution, but this seemed to destroy the graphene and was therefore deemed unfit method for deposition. OM images of the chip after drying overnight and after the wash are presented in Figure 42.

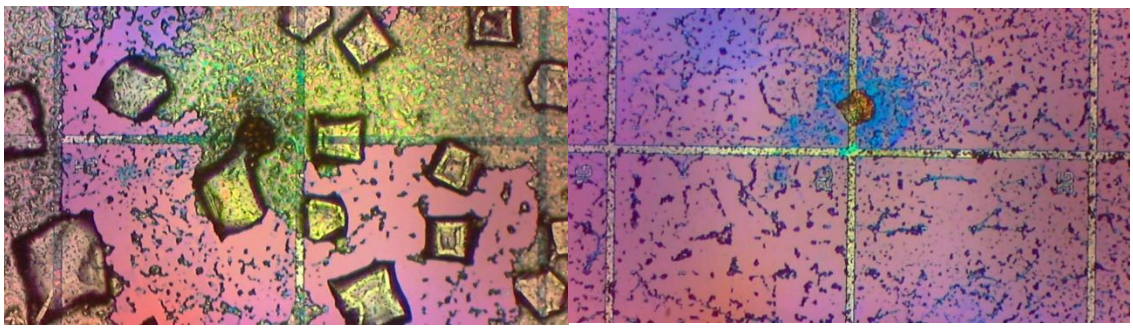

Figure 42. On the left: sample surface after letting the GNP solution dry on it overnight and on the right: sample surface after washing.

Spin-coating was attempted again on VMH397 in a similar manner as before (120 s, 2000 rpm), but this time the spinning was repeated five times. This seemed to coat the chip rather evenly and something was clearly on the surface and visible even with OM. The chip was also characterized with AFM to determine that the black spots visible in OM were indeed the GNPs. OM image and AFM image of the results of this coating are presented in Figure 43.

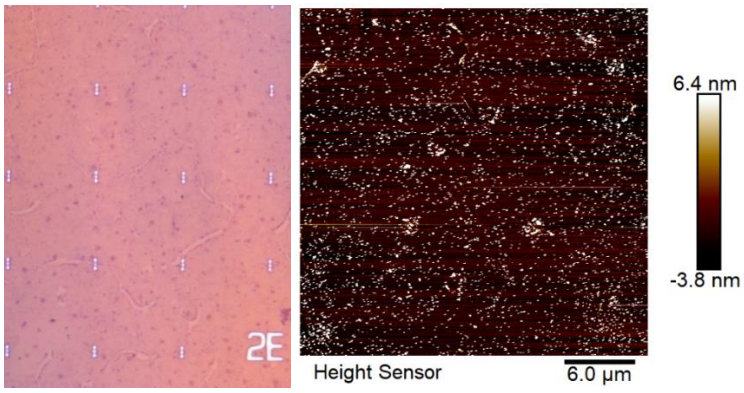

Figure 43. On the left: OM image of the sample surface after 5 spin-coatings, on the right: AFM image of the sample surface after 5 spin-coatings.

This method was chosen to coat VMH395 with optically forged patterns and it seemed to result in rather even coating, even though a drop seemed to be stuck in the middle of the sample at the end of the spin-coatings, which resulted in the oil-slick like surface, fortunately, outside the metal grid. However, after AFM measurements, it became clear, that the coating was not as even as hoped, but could be sufficient for the antenna-effect, should that be detectable. OM and AFM images of the optically forged lines in grid 4E after GNP deposition are presented in Figure 44. All the AFM images of the optically forged areas with GNPs deposited are presented in appendix 4. A cross- section of nanoparticles on the sample is presented in Figure 45.

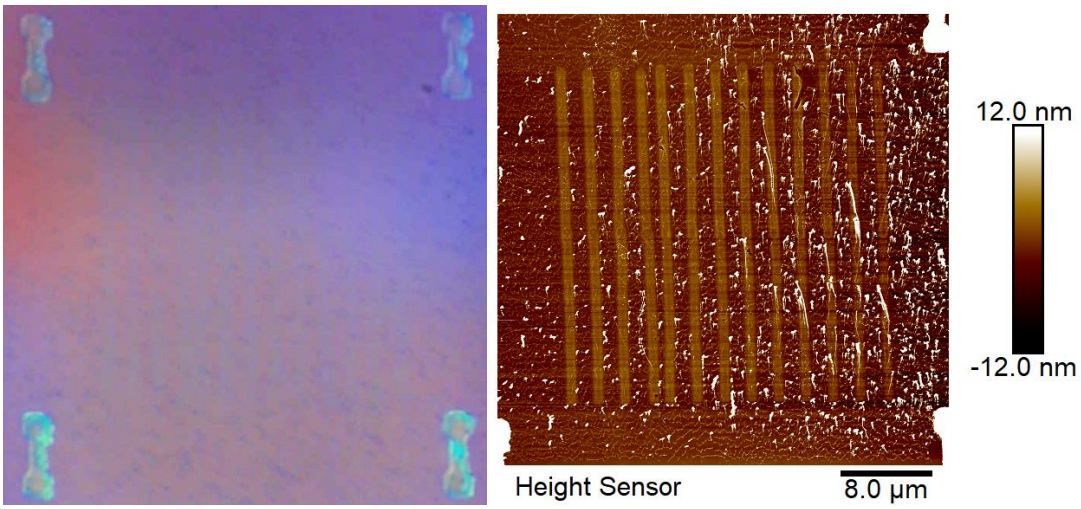

Figure 44. On the left: OM image of grid 4E lines after GNP deposition, on the right: AFM image of grid 4E lines after GNP deposition.

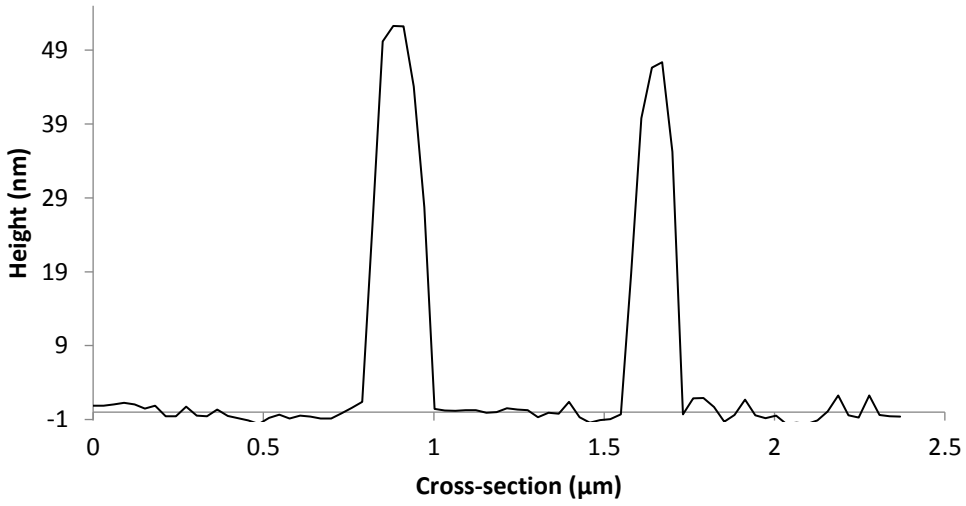

Figure 45. Cross-section of GNP:s on lines of square 4E.

The height of white specs that are assumed to be GNP in the cross-section varies from 40 nm to almost 100 nm. The average diameter of the nanoparticle in the solution was 50 nm, so having white specs with heights (diameters) in the both sides of that and around double that makes sense. It can be said that the white specs are indeed the deposited nanoparticles and not impurities, although those undoubtedly are present in the sample as well.

As mentioned before, the gold nanoparticle deposition was not as even as was hoped due to a drop not being propelled off the sample surface during spin-coating. This was fortunately the most visible in square 2B that had the structures not big enough to fill the whole aperture in FTIR measurements. An example AFM image of the uneven coating and even some left-over solution residue over the line-grid of square 2B is presented in Figure 46. From the image it is clear that something has scratched the grid somewhere on the way as well as a large scar of missing graphene is visible at the top of the structure compared to Figure 33.

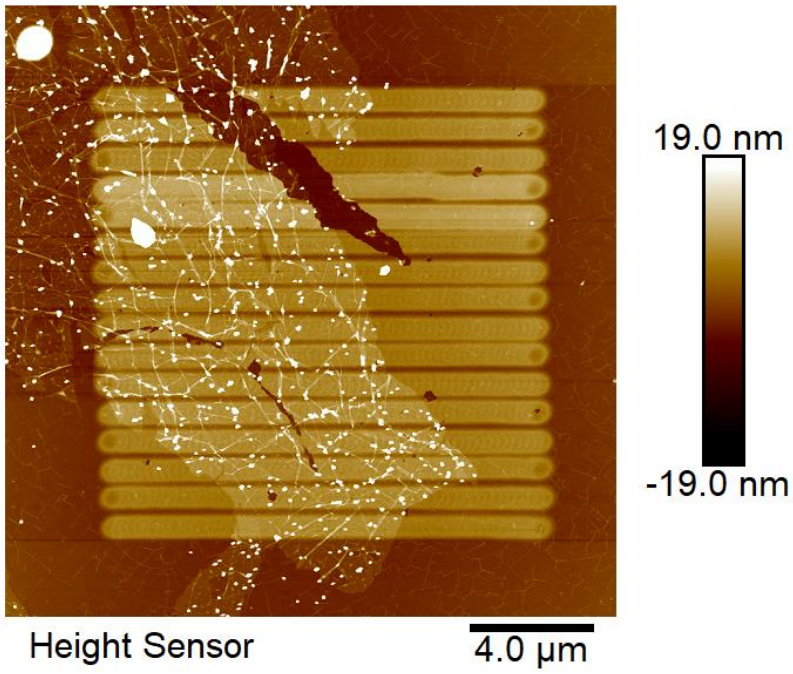

Figure 46. Uneven GNP coating, some solution left-over and a scratch on a line-grid 2B.

6.4 FTIR measurements

The used microscope is rather old, and the alignment is no easy task. It was deemed early on that something is wrong with the objective-turret of the microscope as the location of

the crosshair in the microscope changed rather drastically between different objectives. Re-alignment of the microscope was attempted but when this did not fix the problem the whole microscope was taken apart and all the mirrors were cleaned also in the process. This did not fix the problem either and it seemed that the screws where objectives are connected are slightly different, which causes the objectives to be in slightly different angles. How this has never been noticed before is unclear. Having to only use the IR-objective, which is not optimal for optical microscopy and only has 15x magnification, made navigation in the sample difficult. Luckily the metallic reference grid was easy to see but for example 2B blisters were not intense enough to be visible and could not therefore be measured. This was not an issue since the patterns in 2B were too small to measure anyways as explained later below.

Multiple measurements were done to examine best measurement conditions and settings. It was determined that resolution 4 cm^{-1} was best as better resolution resulted in a messy graph and less was not defined enough. Best scanning rate ergo how many scans per measurement are made, was determined to be 64 as it did not differ much from scanning rate of 120 but was still noticeably better than any scanning rate lower than the chosen 64. Different aperture sizes were tested as well to see how small area could be measured with reasonable signal to noise ratio. 30x30 µm aperture was chosen to be the smallest possible aperture, as mentioned before, but measurements with 40x40 µm aperture size were conducted as well. An example of why the 30x30 µm objective is the smallest feasible one can be seen as the characteristic signal (dip around 1100 wavenumbers) for SiO_2 disappears.

In addition to these difficulties the Omnic program that was used in measurements demands a new background measurement every 120 s. There was even an option to use previously saved background for measurements for other measurements, but it couldn't be done in practice as the whole program crashed. Also, the gold mirror used as a background was very scratched and it was difficult to find the same position every time, so the intensity of the background absorbance changed drastically between measurements conducted on different days. A spectra that shows the difference between the measured backgrounds for 2B patterns, 3E, 4E and 4F patterns and all the patterns after GNP depositions, all of these measurements being done in different occasions, is shown in Figure 47. It is clearly visible that the background for 3F, 4F and 4E has drastically higher absorbance than any other background. This affects the comparison of data measured on

different days but the shape of the spectra should still show signs if there would be any plasmonic resonances.

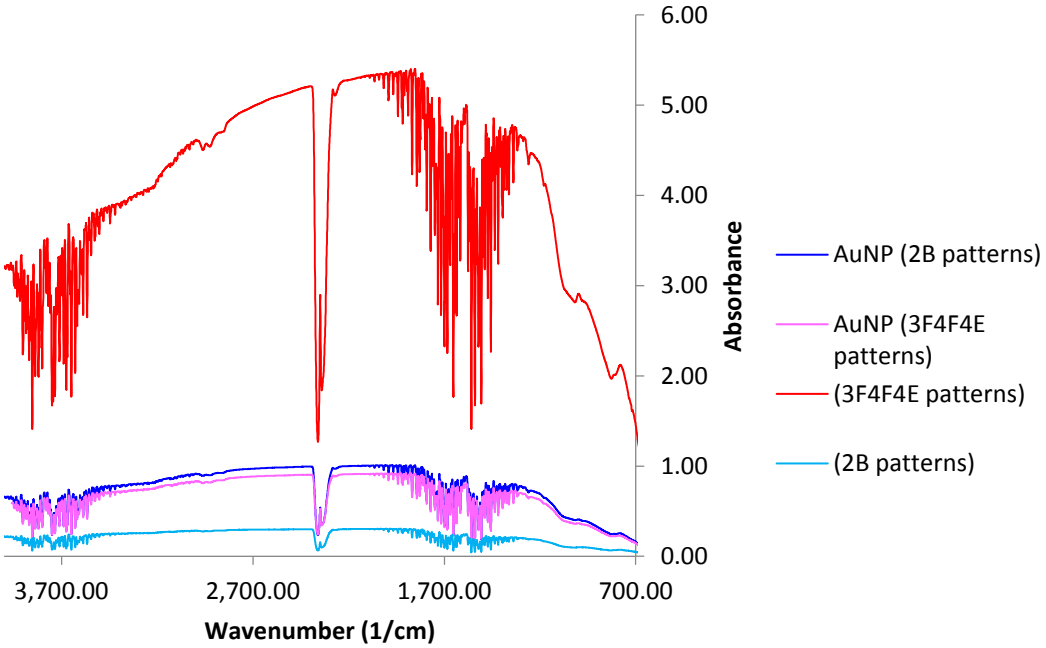

Figure 47. Difference in intensity of different background measurements.

6.4.1 FTIR measurements of the optically forged areas

The IR response was measured for each area patterned area separately by focusing optical microscope and limiting the field of view to only the patterned area with the aperture. The IR response for the smaller patterned areas in VMH395 square 2B was also measured but as that included a lot of pristine graphene as well the data was not determined to be reliable and was excluded. In addition to the patterned areas, signal from unpatterned parts of graphene was measured as well to act as reference point. A picture of measured IR spectra in full range and zoomed to relevant spectral area for 3F, 4E and 4F patterns for both 30x30 and 40x40 µm aperture sizes is presented in Figure 48.

The absorbance does not really differ between different structures with the same aperture. There is slight difference in the shape of the spectra between two aperture sizes. While the shape of the spectra stays relatively the same, the bigger aperture has more defined features. This is due to the signal being better with bigger aperture. The 40x40 µm unpatterned spectrum has slightly lower overall absorbance compared to other measurements with that aperture, but as the shape of the spectrum is similar to the others this is not because of the structures. Graphene plasmonics should anyway not raise the

whole absorbance, but only the absorbance in FIR region, more specifically below 100 wavenumbers. The slight noise around 2350 cm^{-1} is due to presence of carbon dioxide despite the purge. This is likely due to the microscope not being completely air-proof. The slight dip around 800 cm^{-1} and the large dip around 1100 cm^{-1} are characteristic IR absorptions for stretching and bending of silicon dioxide film on top of silicon chip.[104] In the results of this work they are indeed negative changes in absorption, even though in normal FTIR spectroscopy they are positive. This is due to the gold mirror used as a background.

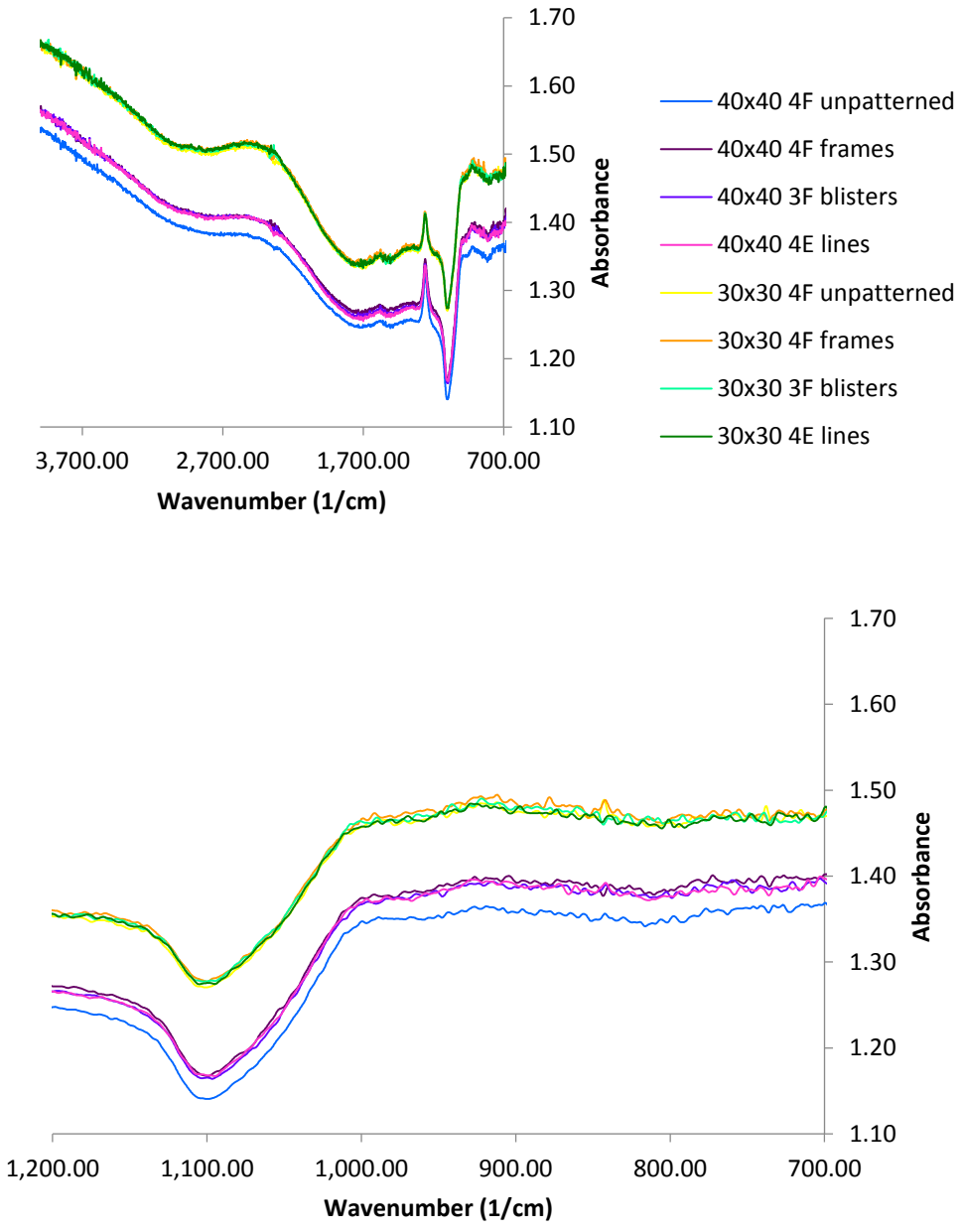

Figure 48. Above: Full range measured IR absorbance from reflection measurement of patterns in squares 3F, 4E and 4F. Below: Zoom on the plasmonically relevant area of the spectra.

Obtained FTIR spectra were compared to the IR-absorbance spectra of unpatterned regions of graphene. A difference between the patterned areas 3F, 4E and 4F and unpatterned area in grid 4F for aperture size 40x40 µm is presented in Figure 49 both in full range and zoomed to relevant area. All similar spectra are presented in appendix 5.

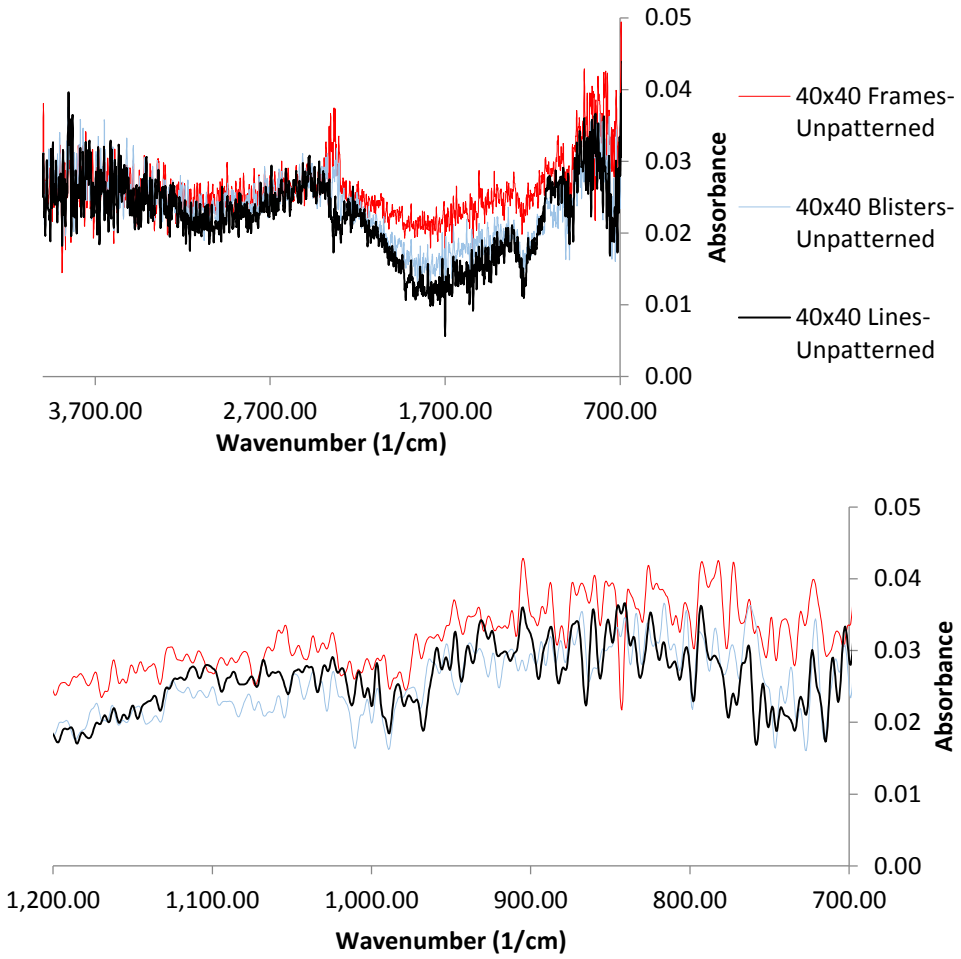

Figure 49. Above: Difference between IR-absorption in patterns 3E, 4E and 4F and unpatterned graphene for aperture sizes 30x30 µm and 40x40 µm in full measurement range. Below: Same zoomed to relevant spectral area.

The whole absorption seems to be elevated slightly so even though there is change in absorption, no conclusive evidence of plasmons can be detected. The peak around 2500 cm^{-1} is once again due to components of air (carbon dioxide and water vapor) absorbing some of the IR radiation even though the purge is present in the measurements and had been running for several hours before measurements. The dip in the 40x40 aperture size spectra around 1200 cm^{-1} is characteristic to Si/SiO_2 chip but the higher part below 1000 cm^{-1} could be due to plasmonic resonances. It should however be rather different

between the lines and the blisters as the blisters should support LSPRs and the features are much smaller.

6.4.2 FTIR measurements of the optically forged areas with GNPs

FTIR measurements of all the patterned areas were performed with aperture sizes 30x30 and 40x40 µm under purge. Obtained FTIR spectrum was compared to the FTIR spectrums measured before GNP deposition. The comparison and the difference between coated and uncoated spectra for grid 4E lines are presented in Figures 50 and 51 respectively. All the comparisons for all the patterns are presented in appendix 6.

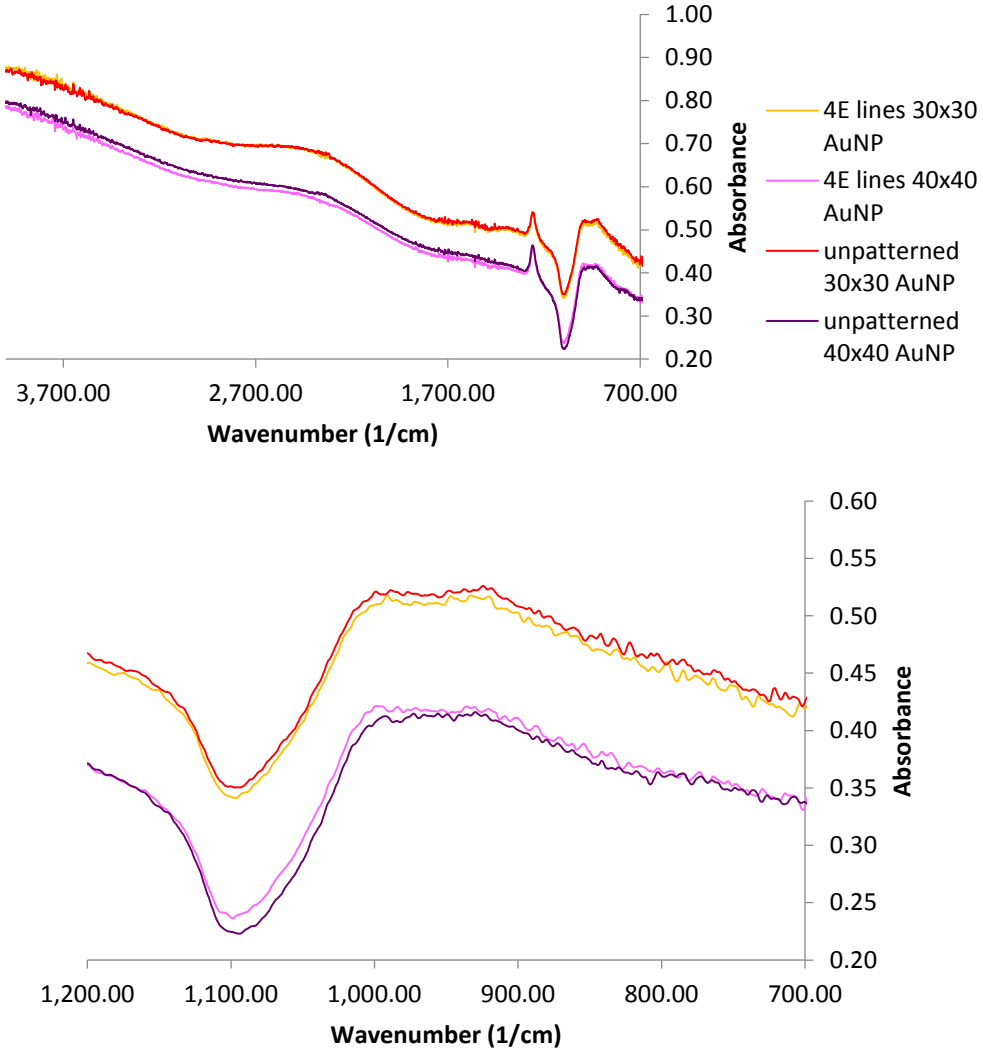

Figure 50. Comparison of FTIR spectrum of lines in grid 4E before GNP deposition and after. Full range and zoom to relevant spectral area.

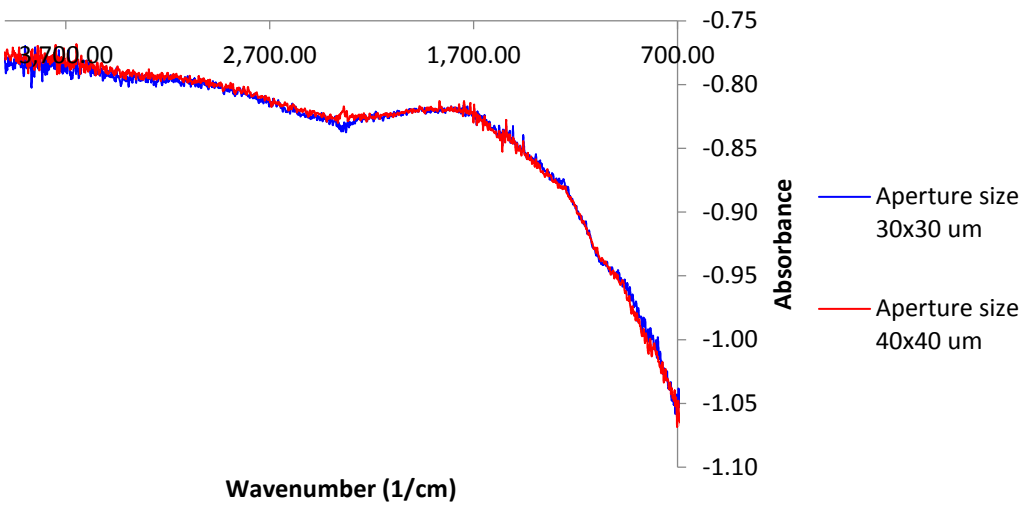

Figure 51. Subtraction of the uncoated spectra from the coated spectra of lines in 4E.

None of the comparison spectra where the uncoated spectra has been subtracted from the coated spectra show any signs of rise in absorbance. In fact, almost all of them show a drop in absorbance as the subtraction is negative all through the comparison spectra. The most extreme change in absorption is below 1700 cm^{-1} where a steep drop is observed. This could be an actual artefact of the gold nanoparticles, but as 2B line-grid had different background measurement than 3E, 4E and 4F before GNP deposition and the subtraction for this structure resulted in positive change in absorbance, it is more likely that the differences in background intensities are behind the phenomena. In addition, as concluded before, square 2B pattern results are not as reliable anyways as they do not completely fill the aperture size. The subtraction of uncoated spectra of 4F frames from the GNP coated spectra at aperture size 40x40 µm shows interesting behaviour around 1200 cm^{-1}. Image of the subtraction spectra is presented in Figure 52. This behaviour is unique and could not be reproduced with more FTIR measurements. So, while exciting and promising, it is regarded to an erroneous result. It can therefore be concluded that gold nanoparticles do not seem to change the IR absorbance in the desired manner, so they do not seem to be acting as antennas at least in the measurable region.

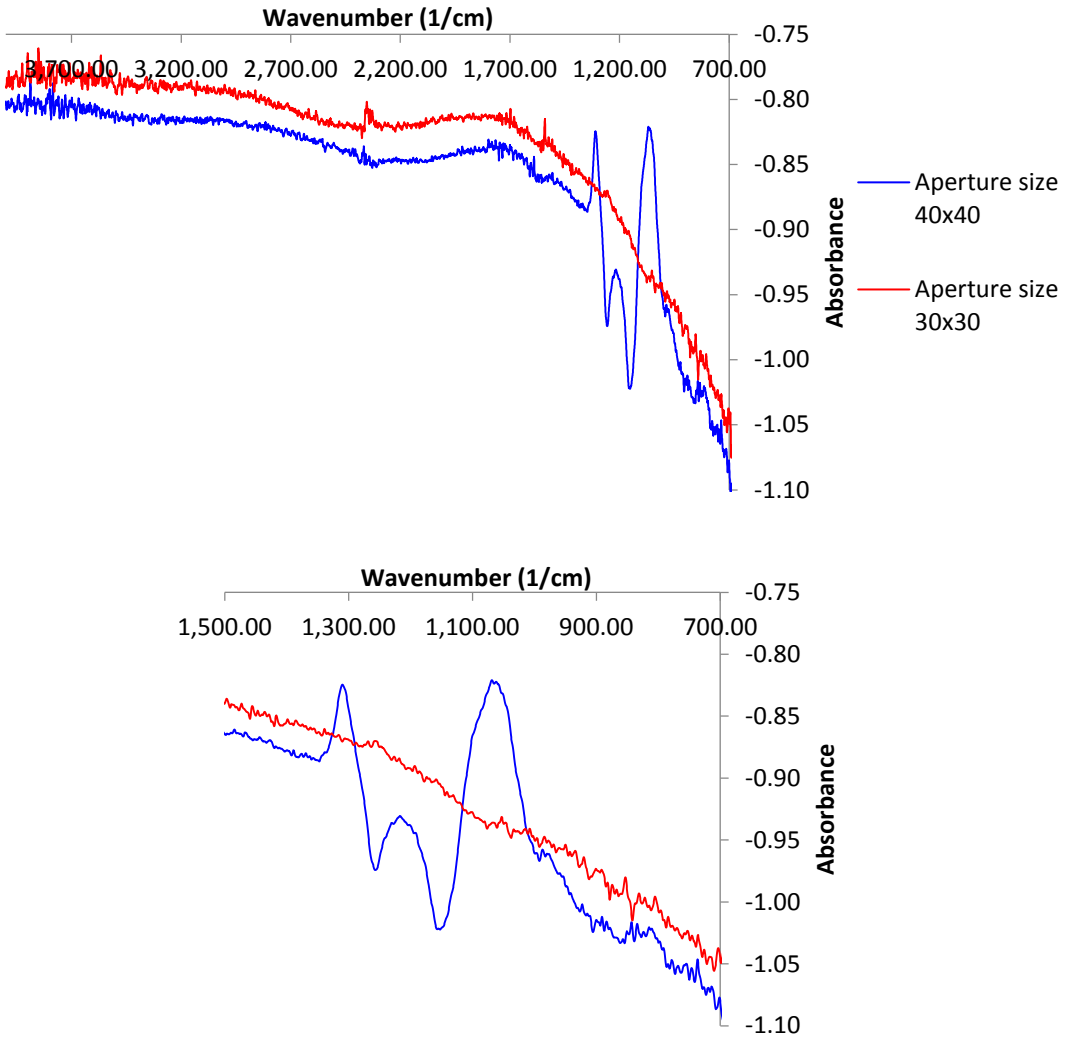

Figure 52. Comparison spectra for 4F frames for both aperture sizes and in full spectral range and zoomed to relevant spectral range.

7 Discussion

The highest obtained structures were in the 2B line-grid but as it was done before discovering the aperture limitations of the FTIR microscope (30x30 µm) and they could not be considered reliable enough to give real plasmon FTIR signal from the patterned parts as it did not fill the aperture completely. The highest patterns used in the actual measurements were all generally less than 5 nanometers, which could be an issue in trapping the LSPRs. Annealing before patterning could be a solution, as that would ensure moisture or impurities on top of graphene would not factor negatively on optical forging.

The aperture was chosen to be 30x30 µm (and 40x40 µm) as it produced a feasible measurement signal when compared to normal graphene IR spectra without the aperture. However, the signal from this area was still incredibly low and this could also be a factor in the absence of GSPs on the forged structures. Larger aperture sizes would mean larger oxidized patterns, which would be very time consuming and hard to produce in consistent quality, as can already be seen from having to separate larger structures into four areas and manually fit them before patterning (see appendix 2 figure 6).

Another issue with large patterned areas are the unpatterned areas in between the patterned structures. As the structures are only 1 µm wide with subwavelength features, it is impossible to focus on only one structure and thus many small structures are used. Perhaps this large average of small structures is not enough to overcome the wave vector momentum mismatch and other means such as SNOM could be attempted to launch the plasmons and see their behavior in the forged structures. This would however negate the whole idea of the thesis, which was to use small optically forged areas to overcome the mismatch.

Aside from aperture possibly being too small, the background also changed between measurements conducted on different days, meaning that the data is incomparable, even though some comparison was done in this work.

There is also a possibility that there are plasmons in these structures, but they are beyond the spectral range of the measurement devices used. They could perhaps be slightly shifted towards the visible change, or they could better be detected with a bias-voltage, which changes the plasmon frequency, but this was not done due to inability to detect plasmons with the equipment used in HIM milled graphene nanoribbons, despite experimental results being produced previously on similar setups.

8 Conclusions

Graphene is a two-dimensional material with exceptional electrical properties due to its charge carriers behaving like Dirac fermions. Graphene can also be doped by changing the amount of charge carriers either chemically or with an electrical nias. Graphene has been shown to support plasmons that usually are detected in far infrared and terahertz ranges, making graphene a promising material for optics and sensors in the infrared region. Graphene plasmons exhibit many advantageous properties compared to metal plasmons, as graphene plasmons are highly confined due to graphene's thinness and they also propagate longer distances with lower losses. Aforementioned tunability also applies to graphene plasmons.

The largest obstacle between graphene plasmonics is the large mismatch between the momentum of the exciting light and graphene plasmons, meaning that some additional steps needs to be taken for light to excite plasmons in graphene. Such steps can be cutting graphene into smaller strips or introducing corrugations or subwavelength structures in graphene. This could be done with for example with optical forging.

In this work, optically forged structures with sub-wavelength features as well as structures resembling graphene nanoribbons were tested under FTIR microscope for changes in the infrared absorption, which would indicate presence of plasmons. Despite the many reasons to speculate why no change in signal is detected, according to this experiment, the optically forged structures are not sufficient to overcome the mismatch and allow excitation of plasmons in graphene.

This could be studied further by scattering near field optical microscopy measurements of bias voltage measurements, but this experiment does not really provide a strong motive to do so.

References

1. Phiri, J.; Gane, P. and Maloney, T. C., General overview of graphene: Production, properties and application in polymer composites, *Mater. Sci. Eng. B Solid-State Mater. Adv. Technol.*, **2017**, *215*, 9–28.

2. Bird, J. O. and Chivers, P. J., The structure of materials. In: Bird, J. O. and Chivers, P. J. B. T.-N. E. and P. S. P. B. (eds.), , Newnes, 1993, pp. 493–503.

3. Campbell, E. K.; Holz, M. and Maier, J. P., C60+ IN DIFFUSE CLOUDS: LABORATORY AND ASTRONOMICAL COMPARISON, *Astrophys. J.*, **2016**, *826*, L4.

4. The Royal Swedish Academy of Sciences, Graphene: Scientific background on the Nobel Prize in Physics 2010, *R. Swedish Acad. Sci.*, **2010**, *50005*, 0–10.

5. Lee, C.; Wei, X.; Kysar, J. W. and Hone, J., Measurement of the Elastic Properties and Intrinsic Strength of Monolayer Graphene, **2008**, *321*, 385–388.

6. Wang, J.; Ma, F.; Liang, W. and Sun, M., Electrical properties and applications of graphene, hexagonal boron nitride (h-BN), and graphene/h-BN heterostructures, *Mater. Today Phys.*, **2017**, *2*, 6–34.

7. Pugno, N. M., The elasticity and strength of graphene, **2009**, *661*, 101–103.

8. Memarian, F.; Fereidoon, A. and Darvish Ganji, M., Graphene Young's modulus: Molecular mechanics and DFT treatments, *Superlattices Microstruct.*, **2015**, *85*, 348–356.

9. Naumis, G. G.; Barraza-Lopez, S.; Oliva-Leyva, M. and Terrones, H., Electronic and optical properties of strained graphene and other strained 2D materials: A review, *Reports Prog. Phys.*, **2017**, *80*.

10. Kundu, R., Tight-binding parameters for graphene, *Mod. Phys. Lett. B*, **2011**, *25*, 163–173.

11. Castro Neto, A. H.; Guinea, F.; Peres, N. M. R.; Novoselov, K. S. and Geim, A. K., The electronic properties of graphene, *Rev. Mod. Phys.*, **2009**, *81*, 109–162.

12. Pop, E.; Varshney, V. and Roy, A. K. a. K., Thermal properties of graphene: Fundamentals and applications, *MRS Bull.*, **2012**, *37*, 1273–1281.

13. Marquina, J.; Power, C.; González, J. and Broto, J.-M., Ab Initio Study of the Electronic and Vibrational Properties of 1-nm-Diameter Single-Walled Nanotubes, *Adv. Mater. Phys. Chem.*, **2013**, *03*, 178–184.

14. Chen, S.; Moore, A. L.; Cai, W.; Suk, J. W.; An, J.; Mishra, C.; Amos, C.; Magnuson, C. W.; Kang, J.; Shi, L. and Ruoff, R. S., Raman measurements of thermal transport in suspended monolayer graphene of variable sizes in vacuum and gaseous environments, *ACS Nano*, **2011**, *5*, 321–328.

15. Young, H. and Freedman, R., *University physics with modern physics*, 2007.

16. Kostić, R.; Mirić, M.; Radić, T.; Radović, M.; Gajić, R. and Popović, Z. V., Optical characterization of graphene and highly oriented pyrolytic graphite, *Acta Phys. Pol. A*, **2009**, *116*, 718–721.

17. Jiang, Z.; Zhang, Y.; Tan, Y.; Stormer, H. L. and Kim, P., Quantum Hall effect in graphene, **2007**, *143*, 14–19.

18. Suzuki, A.; Tanabe, M. and Fujita, S., Electronic Band Structure of Graphene Based on the Rectangular 4-Atom Unit Cell, *J. Mod. Phys.*, **2017**, *08*, 607–621.

19. Xu, Q.; Luo, J. W.; Li, S. S.; Xia, J. B.; Li, J. and Wei, S. H., Chemical trends of defect formation in Si quantum dots: The case of group-III and group-V dopants, *Phys. Rev. B - Condens. Matter Mater. Phys.*, **2007**, *75*, 1–6.

20. Falkovsky, L. A., Optical properties of graphene, *J. Phys. Conf. Ser.*, **2008**, *129*, 12004.

21. García de Abajo, F. J., Graphene Plasmonics: Challenges and Opportunities, *ACS Photonics*, **2014**, *1*, 135–152.

22. Fei, Z.; Rodin, A. S.; Andreev, G. O.; Bao, W.; Mcleod, A. S. and Wagner, M., Gate-tuning of graphene plasmons revealed by infrared nano-imaging.

23. Low, T. and Avouris, P., Graphene plasmonics for terahertz to mid-infrared applications, *ACS Nano*, **2014**, *8*, 1086–1101.

24. Grigorenko, A. N.; Polini, M. and Novoselov, K. S., Graphene plasmonics - optics in flatland., *arXiv.org, e-Print Arch. Condens. Matter*, **2013**, 1–25, arXiv:1301.4241v1 [cond-mat.mes-hall].

25. Mak, K. F.; Ju, L.; Wang, F. and Heinz, T. F., Optical spectroscopy of graphene:

From the far infrared to the ultraviolet, *Solid State Commun.*, **2012**, *152*, 1341–1349.

26. Chen, J.; Zeng, Y.; Xu, X.; Chen, X.; Zhou, Z.; Shi, P.; Yi, Z.; Ye, X.; Xiao, S. and Yi, Y., Plasmonic absorption enhancement in elliptical graphene arrays, *Nanomaterials*, **2018**, *8*.

27. Bao, Q.; Zhang, H.; Wang, Y.; Ni, Z.; Yan, Y.; Shen, Z. X.; Loh, K. P. and Tang, D. Y., Atomic-layer craphene as a saturable absorber for ultrafast pulsed lasers, *Adv. Funct. Mater.*, **2009**, *19*, 3077–3083.

28. Ooi, K. J. A. and Tan, D. T. H., Nonlinear graphene plasmonics, *Proc. R. Soc. A Math. Phys. Eng. Sci.*, **2017**, *473*.

29. Ishikawa, K. L., Nonlinear optical response of graphene in time domain, *Phys. Rev. B - Condens. Matter Mater. Phys.*, **2010**, *82*, 3–6.

30. Cheng, J. L.; Vermeulen, N. and Sipe, J. E., Third order optical nonlinearity of graphene, *New J. Phys.*, **2014**, *16*.

31. Wang, Q. H.; Jin, Z.; Kim, K. K.; Hilmer, A. J.; Paulus, G. L. C.; Shih, C. J.; Ham, M. H.; Sanchez-Yamagishi, J. D.; Watanabe, K.; Taniguchi, T.; Kong, J.; Jarillo-Herrero, P. and Strano, M. S., Understanding and controlling the substrate effect on graphene electron-transfer chemistry via reactivity imprint lithography, *Nat. Chem.*, **2012**, *4*, 724–732.

32. Pantano, M. F.; Iacob, E.; Picciotto, A.; Margesin, B.; Centeno, A.; Zurutuza, A.; Galiotis, C.; Pugno, N. M. and Speranza, G., Investigation of charges-driven interaction between graphene and different SiO 2 surfaces, *Carbon N. Y.*, **2019**, *148*, 336–343.

33. Kang, Y.; Kang, J. and Chang, K. J., Electronic structure of graphene and doping effect on SiO 2, **2008**, 1–5.

34. Warner, J. H.; Schäffel, F.; Bachmatiuk, A. and Rümmeli, M. H., Chapter 5 - Characterisation Techniques. In: Warner, J. H.; Schäffel, F.; Bachmatiuk, A. and Rümmeli, M. H. B. T.-G. (eds.), *Graphene: Fundamental and emergent applications*, Elsevier, 2013, pp. 229–332.

35. Chakraborty, M. and Hashmi, M. S. J. B. T.-R. M. in M. S. and M. E., Graphene as a Material – An Overview of Its Properties and Characteristics and

Development Potential for Practical Applications. Elsevier, 2018.

36. Johansson, A.; Tsai, H.; Aumanen, J.; Koivistoinen, J.; Myllyperkiö, P.; Hung, Y.; Chuang, M.; Chen, C.; Woon, W. Y. and Pettersson, M., Chemical composition of two-photon oxidized graphene, *Carbon N. Y.*, **2017**, *115*, 77–82.

37. Johansson, A.; Myllyperkiö, P.; Koskinen, P.; Aumanen, J.; Koivistoinen, J.; Tsai, H. C.; Chen, C. H.; Chang, L. Y.; Hiltunen, V. M.; Manninen, J. J.; Woon, W. Y. and Pettersson, M., Optical Forging of Graphene into Three-Dimensional Shapes, *Nano Lett.*, **2017**, *17*, 6469–6474.

38. Kuila, T.; Bose, S.; Mishra, A. K.; Khanra, P.; Kim, N. H. and Lee, J. H., Chemical functionalization of graphene and its applications, *Prog. Mater. Sci.*, **2012**, *57*, 1061–1105.

39. Liu, B.; Salgado, S.; Maheshwari, V. and Liu, J., DNA adsorbed on graphene and graphene oxide: Fundamental interactions, desorption and applications, *Curr. Opin. Colloid Interface Sci.*, **2016**, *26*, 41–49.

40. Novoselov, K. S.; Geim, A. K.; Morozov, S. V.; Jiang, D.; Zhang, Y.; Dubonos, S. V.; Grigorieva, I. V. and Firsov, A. A., Electric field effect in atomically thin carbon films., *Science (80-.).*, **2004**, *306*, 666–669.

41. Hernandez, Y.; Nicolosi, V.; Lotya, M.; Blighe, F. M.; Sun, Z.; De, S.; Mcgovern, I. T.; Holland, B.; Byrne, M.; Ko, Y. K. G. U. N.; Boland, J. J.; Niraj, P.; Duesberg, G.; Krishnamurthy, S.; Goodhue, R.; Hutchison, J.; Scardaci, V.; Ferrari, A. C. and Coleman, J. N., High-yield production of graphene by liquid-phase exfoliation of graphite, 563–568.

42. Achee, T. C.; Sun, W.; Hope, J. T.; Quitzau, S. G.; Sweeney, C. B.; Shah, S. A.; Habib, T. and Green, M. J., High-yield scalable graphene nanosheet production from compressed graphite using electrochemical exfoliation, *Sci. Rep.*, **2018**, 1–8.

43. Carlsson, J.-O. and Martin, P. M., Chapter 7 - Chemical Vapor Deposition. In: Martin, P. M. B. T.-H. of D. T. for F. and C. (Third E. (ed.), *Handbook of Deposition Technologies for Films and Coatings (Third Edition)*, William Andrew Publishing, Boston, 2010, pp. 314–363.

44. Lee, H. C.; Liu, W.-W.; Chai, S.-P.; Mohamed, A. R.; Lai, C. W.; Khe, C.-S.; Voon, C. H.; Hashim, U. and Hidayah, N. M. S., Synthesis of Single-layer

Graphene: A Review of Recent Development, *Procedia Chem.*, **2016**, *19*, 916–921.

45. Avouris, P. and Dimitrakopoulos, C., Graphene: synthesis and applications, *Mater. Today*, **2012**, *15*, 86–97.

46. Mattevi, C.; Kim, H. and Chhowalla, M., A review of chemical vapour deposition of graphene on copper, *J. Mater. Chem.*, **2011**, *21*, 3324–3334.

47. Ruan, G.; Sun, Z.; Peng, Z. and Tour, J. M., Growth of Graphene from Food, Insects, and Waste, *ACS Nano*, **2011**, *5*, 7601–7607.

48. Sharma, S.; Kalita, G.; Hirano, R.; Shinde, S. M.; Papon, R.; Ohtani, H. and Tanemura, M., Synthesis of graphene crystals from solid waste plastic by chemical vapor deposition, *Carbon N. Y.*, **2014**, *72*, 66–73.

49. Lee, H. C.; Liu, W. W.; Chai, S. P.; Mohamed, A. R.; Aziz, A.; Khe, C. S.; Hidayah, N. M. S. and Hashim, U., Review of the synthesis, transfer, characterization and growth mechanisms of single and multilayer graphene, *RSC Adv.*, **2017**, *7*, 15644–15693.

50. Zhang, Y.; Zhang, L. and Zhou, C., Review of chemical vapor deposition of graphene and related applications, *Acc. Chem. Res.*, **2013**, *46*, 2329–2339.

51. Kumar, G. and Sarswat, P. ., Interaction of Surface Plasmon Polaritons with Nanomaterials. In: Geddes, C. (ed.), *Reviews in Plasmonics 2015*, SPringer, Cham, 2016, pp. 103–129.

52. Luo, X.; Qiu, T.; Lu, W. and Ni, Z., Plasmons in graphene: Recent progress and applications, *Mater. Sci. Eng. R Reports*, **2013**, *74*, 351–376.

53. Bohm, D. and Pines, D., A Collective Description of Electron Interactions: III. Coulomb Interactions in a Degenerate Electron Gas, *Phys. Rev.*, **1953**, *92*, 609–625.

54. Stern, E. A. and Ferrell, R. A., Surface Plasma Oscillations of a Degenerate Electron Gas, *Phys. Rev.*, **1960**, *120*, 130–136.

55. Barnes, W. L.; Dereux, A. and Ebbesen, T. W., Surface plasmon subwavelength optics, *Nature*, **2003**, *424*, 824–830.

56. Yu, H.; Peng, Y.; Yang, Y. and Li, Z. Y., Plasmon-enhanced light–matter

interactions and applications, *npj Comput. Mater.*, **2019**, *5*, 1–14.

57. Huang, S.; Song, C.; Zhang, G. and Yan, H., Graphene plasmonics: physics and potential applications, *Nanophotonics*, **2016**, *0*, 1–14.

58. Ju, L.; Geng, B.; Horng, J.; Girit, C.; Martin, M.; Hao, Z.; Bechtel, H. A.; Liang, X.; Zettl, A.; Shen, Y. R. and Wang, F., Graphene plasmonics for tunable terahertz metamaterials, *Nat. Nanotechnol.*, **2011**, *6*, 630–634.

59. Sreekanth, K. V.; Zeng, S.; Shang, J.; Yong, K. T. and Yu, T., Excitation of surface electromagnetic waves in a graphene-based Bragg grating, *Sci. Rep.*, **2012**, *2*, 1–7.

60. Syahir, A., Label-free photonics biosensor transducing nano-biological events, *J. Biochem. Microbiol. Biotechnol.*, **2014**, *2*, 32–38.

61. Klimov, V., Surface Plasmons, *Nanoplasmonics*, **2014**, 63–90.

62. Raether, H., *Surface Plasmons on Smooth and Rough Surfaces and on Gratings*, 1st edition, Springer-Verlag Berlin Heidelberg, Berlin, 1988.

63. Homola, J., *Surface Plasmon Resonance Based Sensors*, 1st edition, Springer-Verlag Berlin Heidelberg, Berlin, 2006.

64. Vakil, A. and Engheta, N., Transformation Optics Using Graphene, *Science (80-.).*, **2011**, *332*, 1291 LP – 1294.

65. Despoja, V.; Novko, D.; Dekanić, K.; Šunjić, M. and Marušić, L., Two-dimensional and π plasmon spectra in pristine and doped graphene, *Phys. Rev. B - Condens. Matter Mater. Phys.*, **2013**, *87*, 1–10.

66. Mikhailov, S. A. and Ziegler, K., New electromagnetic mode in graphene, *Phys. Rev. Lett.*, **2007**, *99*, 1–4.

67. Jablan, M.; Buljan, H. and Soljačić, M., Plasmonics in graphene at infrared frequencies, *Phys. Rev. B - Condens. Matter Mater. Phys.*, **2009**, *80*, 1–7.

68. Xiao, S.; Zhu, X.; Li, B. H. and Mortensen, N. A., Graphene-plasmon polaritons: From fundamental properties to potential applications, *Front. Phys.*, **2016**, *11*, 1–13.

69. Xu, Q.; Ma, T.; Danesh, M.; Shivananju, B. N.; Gan, S.; Song, J.; Qiu, C.-W.; Cheng, H.-M.; Ren, W. and Bao, Q., Effects of edge on graphene plasmons as

revealed by infrared nanoimaging, *Light Sci. Appl.*, **2017**, *6*, e16204–e16204.

70. Smirnova, D.; Mousavi, S. H.; Wang, Z.; Kivshar, Y. S. and Khanikaev, A. B., Trapping and Guiding Surface Plasmons in Curved Graphene Landscapes, **2016**.

71. Valle, G. Della; Longhi, S.; Valle, G. Della and Geometric, S. L., Geometric potential for plasmon polaritons on curved surfaces, **2011**.

72. Slipchenko, T. M.; Nesterov, M. L.; Hillenbrand, R.; Nikitin, A. Y. and Martín-Moreno, L., Graphene Plasmon Reflection by Corrugations, *ACS Photonics*, **2017**, *4*, 3081–3088.

73. Alonso-González, P.; Nikitin, A. Y.; Golmar, F.; Centeno, A.; Pesquera, A.; Vélez, S.; Chen, J.; Navickaite, G.; Koppens, F.; Zurutuza, A.; Casanova, F.; Hueso, L. E. and Hillenbrand, R., Controlling graphene plasmons with resonant metal antennas and spatial conductivity patterns, *Science (80-.).*, **2014**, *344*, 1369 LP – 1373.

74. Ni, G. X.; McLeod, A. S.; Sun, Z.; Wang, L.; Xiong, L.; Post, K. W.; Sunku, S. S.; Jiang, B. Y.; Hone, J.; Dean, C. R.; Fogler, M. M. and Basov, D. N., Fundamental limits to graphene plasmonics, *Nature*, **2018**, *557*, 530–533.

75. Buljan, H.; Jablan, M. and Soljačić, M., Damping of plasmons in graphene, *Nat. Photonics*, **2013**, *7*, 346–348.

76. Herr, W., Introduction to Landau damping, *Proc. CAS-CERN Accel. Sch. Adv. Accel. Phys.*, **2013**, *009*, 377–404.

77. Yao, Y.; Kats, M. A.; Genevet, P.; Yu, N.; Song, Y.; Kong, J. and Capasso, F., Broad electrical tuning of graphene-loaded plasmonic antennas, *Nano Lett.*, **2013**, *13*, 1257–1264.

78. Bottari, G.; Herranz, M. Á.; Wibmer, L.; Volland, M.; Rodríguez-Pérez, L.; Guldi, D. M.; Hirsch, A.; Martín, N.; D'Souza, F. and Torres, T., Chemical functionalization and characterization of graphene-based materials, *Chem. Soc. Rev.*, **2017**, *46*, 4464–4500.

79. Kyeyune, B., *Atomic Force Microscopy*, 2017.

80. Pletikapia, G. and Ivoševi Denardis, N., Application of surface analytical methods for hazardous situation in the Adriatic Sea: Monitoring of organic matter dynamics and oil pollution, *Nat. Hazards Earth Syst. Sci.*, **2017**, *17*, 31–44.

81. Worsfold, P. J., Molecular Spectroscopy - Raman spectroscopy, *TrAC - Trends Anal. Chem.*, **1987**, *6*, X.

82. Malard, L. M.; Pimenta, M. A.; Dresselhaus, G. and Dresselhaus, M. S., Raman spectroscopy in graphene, *Phys. Rep.*, **2009**, *473*, 51–87.

83. Siregar, S., *Double resonance Raman spectra of G' and G* bands of graphene*, Tohoku University, 2015.

84. Berthomieu, C. and Hienerwadel, R., Fourier transform infrared (FTIR) spectroscopy, *Photosynth. Res.*, **2009**, *101*, 157–170.

85. Rowlette, J.; Bird, B.; Weida, M.; Barre, M.; Arnone, D. and Day, T., High-confidence, high-throughput screening with high-def IR microspectroscopy, *BioOptics World*, **2014**, *7*, 34–37.

86. Zhu, X.; Yan, W.; Uhd Jepsen, P.; Hansen, O.; Asger Mortensen, N. and Xiao, S., Experimental observation of plasmons in a graphene monolayer resting on a two-dimensional subwavelength silicon grating, *Appl. Phys. Lett.*, **2013**, *102*.

87. Kirstein, S., Scanning near-field optical microscopy, **1999**, *4*, 256–264.

88. Wang, L. and Xu, X. G., Scattering-type scanning near-field optical microscopy with reconstruction of vertical interaction, *Nat. Commun.*, **2015**, *6*, 1–9.

89. Xiong, L.; Forsythe, C.; Jung, M.; McLeod, A. S.; Sunku, S. S.; Shao, Y. M.; Ni, G. X.; Sternbach, A. J.; Liu, S.; Edgar, J. H.; Mele, E. J.; Fogler, M. M.; Shvets, G.; Dean, C. R. and Basov, D. N., Photonic crystal for graphene plasmons, *Nat. Commun.*, **2019**, *10*, 1–6.

90. Sirtori, C., Applied physics: Bridge for the terahertz gap, *Nature*, **2002**, *417*, 132–133.

91. Rana, F., Graphene terahertz plasmon oscillators, *IEEE Trans. Nanotechnol.*, **2008**, *7*, 91–99.

92. Chakraborty, S.; Marshall, O. P.; Folland, T. G.; Kim, Y. J.; Grigorenko, A. N. and Novoselov, K. S., Applied optics: Gain modulation by graphene plasmons in aperiodic lattice lasers, *Science (80-.).*, **2016**, *351*, 246–248.

93. Rana, F.; George, P. A.; Strait, J. H. and Dawlaty, J., Graphene terahertz sources and amplifiers, *33rd Int. Conf. Infrared Millim. Waves 16th Int. Conf. Terahertz*

Electron. 2008, IRMMW-THz 2008, **2008**, 5–7.

94. Luneburg, R. K. and King, A. L., Mathematical Theory of Optics, *Am. J. Phys.*, **1966**.

95. Bao, B. Q.; Zhang, H.; Wang, Y.; Ni, Z. and Yan, Y., Atomic-Layer Graphene as a Saturable Absorber for Ultrafast Pulsed Lasers, **2009**, 3077–3083.

96. Lai, H.; Xu, F.; Zhang, Y. and Wang, L., Recent progress on graphene-based substrates for surface-enhanced Raman scattering applications, *J. Mater. Chem. B*, **2018**, *6*, 4008–4028.

97. Hu, Y.; Lee, S.; Kumar, P.; Nian, Q.; Wang, W.; Irudayaraj, J. and Cheng, G. J., Water flattens graphene wrinkles: Laser shock wrapping of graphene onto substrate-supported crystalline plasmonic nanoparticle arrays, *Nanoscale*, **2015**, *7*, 19885–19893.

98. Yang, X.; Sun, Z.; Low, T.; Hu, H.; Guo, X.; García de Abajo, F. J.; Avouris, P. and Dai, Q., Nanomaterial-Based Plasmon-Enhanced Infrared Spectroscopy, *Adv. Mater.*, **2018**, *30*, 1–23.

99. Hu, H.; Yang, X.; Guo, X.; Khaliji, K.; Biswas, S. R.; García de Abajo, F. J.; Low, T.; Sun, Z. and Dai, Q., Gas identification with graphene plasmons, *Nat. Commun.*, **2019**, *10*, 1–7.

100. Aznakayeva, D., *Graphene-based active metamaterials*, The University of Manchester, 2018.

101. Lin, H.; Sturmberg, B. C. P.; Lin, K. Te; Yang, Y.; Zheng, X.; Chong, T. K.; de Sterke, C. M. and Jia, B., A 90-nm-thick graphene metamaterial for strong and extremely broadband absorption of unpolarized light, *Nat. Photonics*, **2019**, *13*, 270–276.

102. Koskinen, P.; Karppinen, K.; Myllyperkiö, P.; Hiltunen, V. M.; Johansson, A. and Pettersson, M., Optically Forged Diffraction-Unlimited Ripples in Graphene, *J. Phys. Chem. Lett.*, **2018**, *9*, 6179–6184.

103. Ju, L.; Geng, B.; Horng, J.; Girit, C.; Martin, M.; Hao, Z.; Bechtel, H. A.; Liang, X.; Zettl, A.; Shen, Y. R. and Wang, F., Graphene plasmonics for tunable terahertz metamaterials, *Nat. Nanotechnol.*, **2011**, *6*, 630–634.

104. Lucovsky, G., Low-temperature growth of silicon dioxide films: A study of

chemical bonding by ellipsometry and infrared spectroscopy, *J. Vac. Sci. Technol. B Microelectron. Nanom. Struct.*, **1987**, *5*, 530.

Appendix

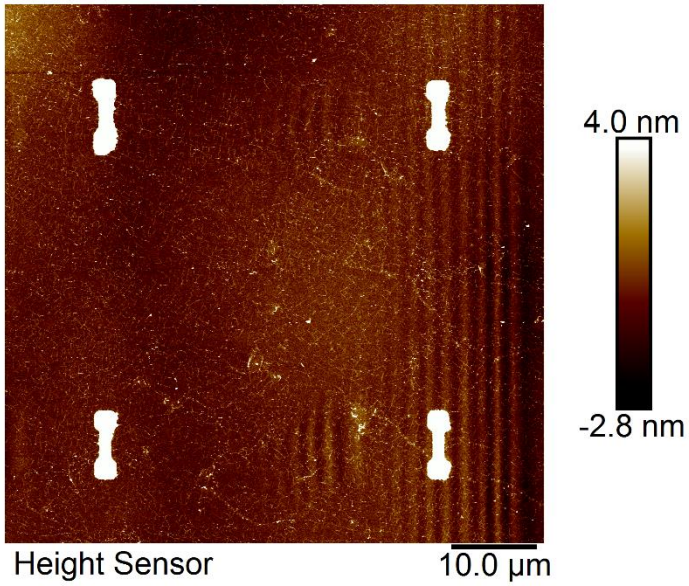

Figure 1. AFM image of unpatterned graphene in square 3F.

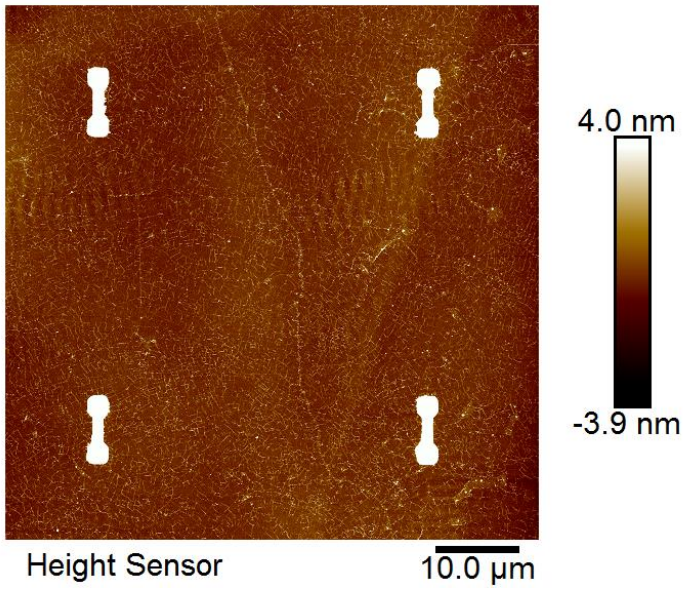

Figure 2. AFM image of unpatterned graphene in square 4E.

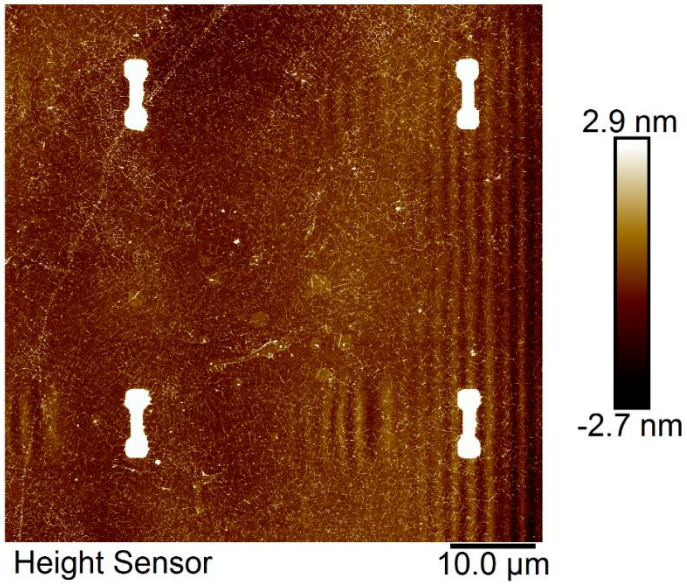

Figure 3. AFM image of unpatterned graphene in square 4F.

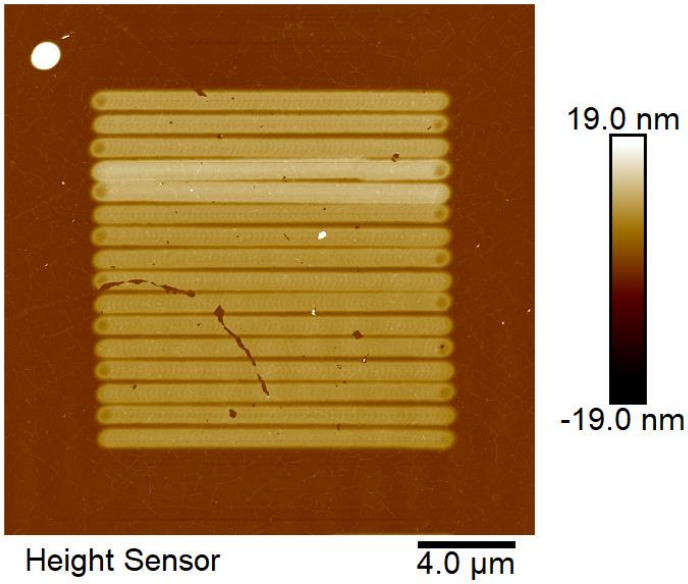

Figure 1. AFM image of line pattern in square 2B.

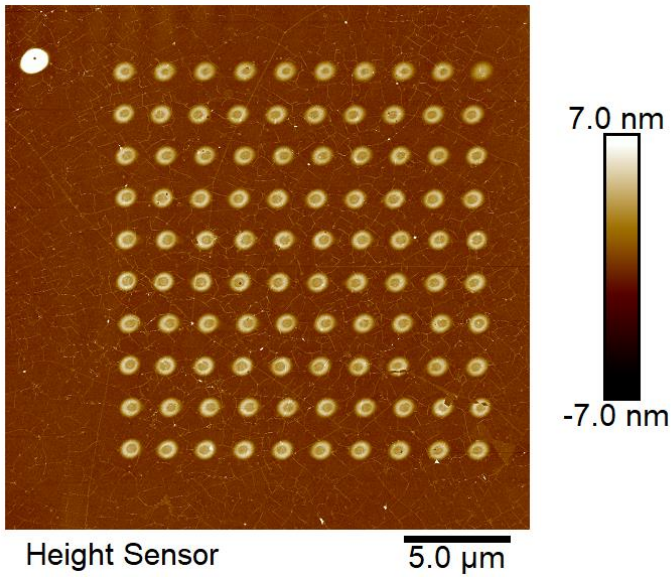

Figure 2**.** AFM image of 10 s blister matrix in square 2B.

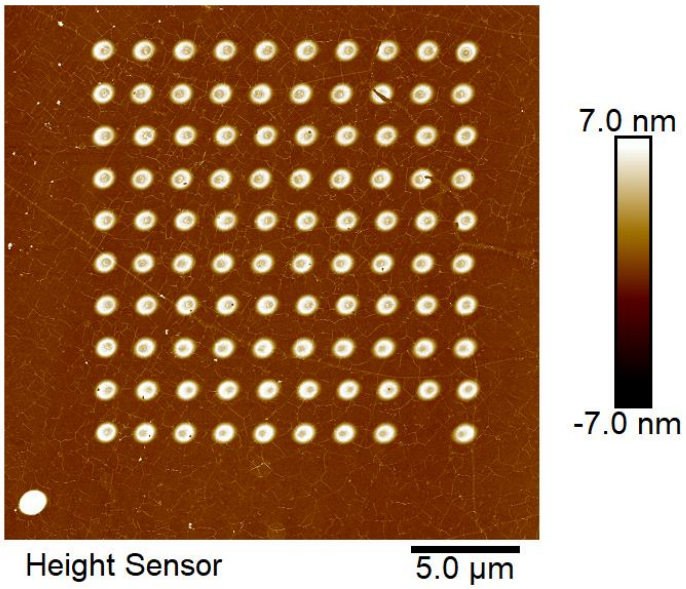

Figure 3**.** AFM image of 30 s blister matrix in square 2B.

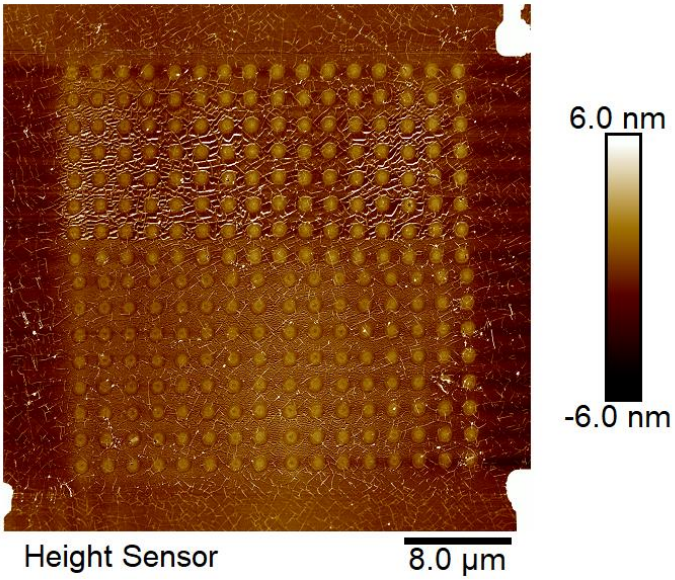

Figure 4. AFM image of blister matrix in square 3F.

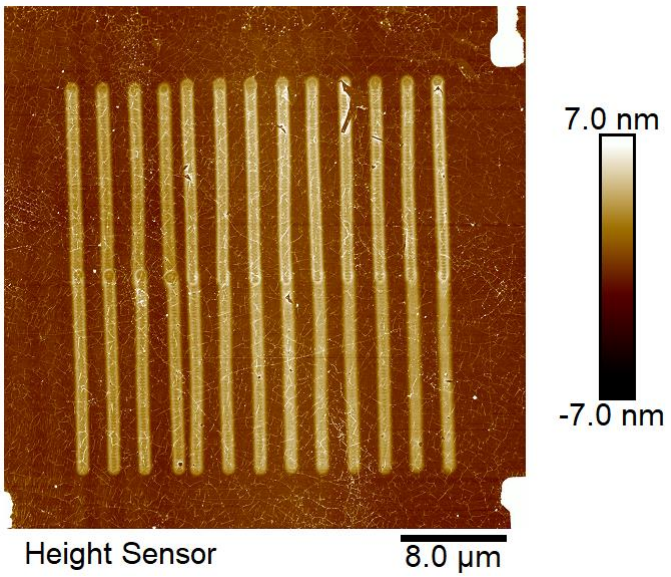

Figure 5. AFM image of lines in square 4E.

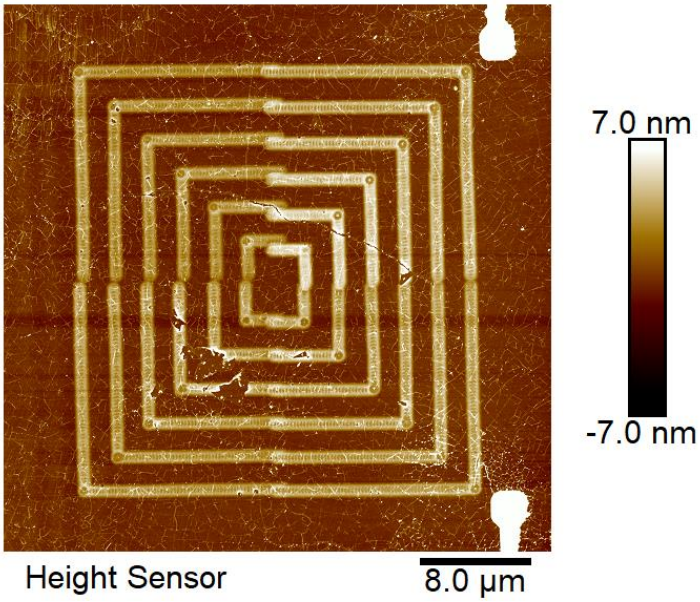

Figure 6. AFM image of frames in square 4.

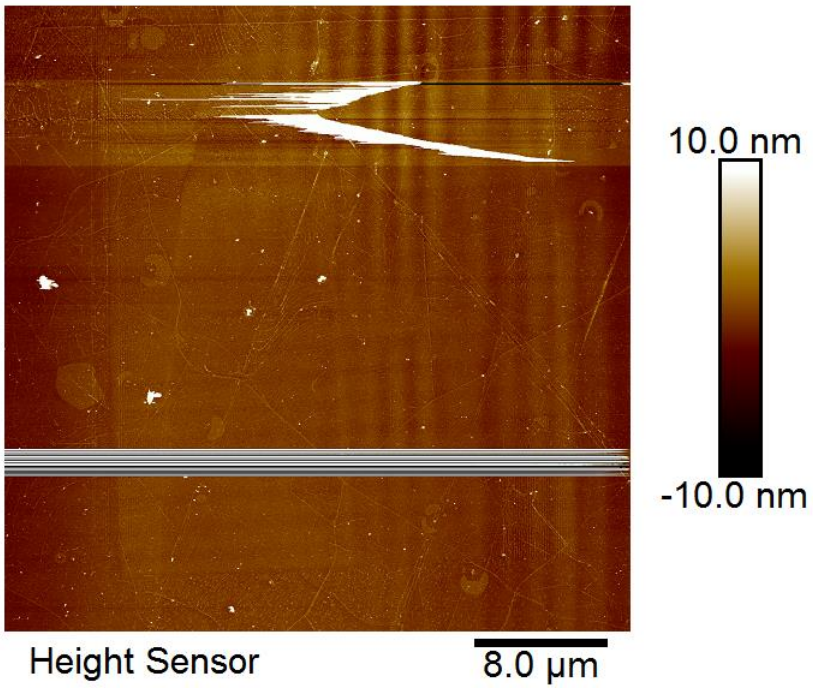

Figure 1. AFM image of oxidized area with irradiation time 0.3 s/spot.

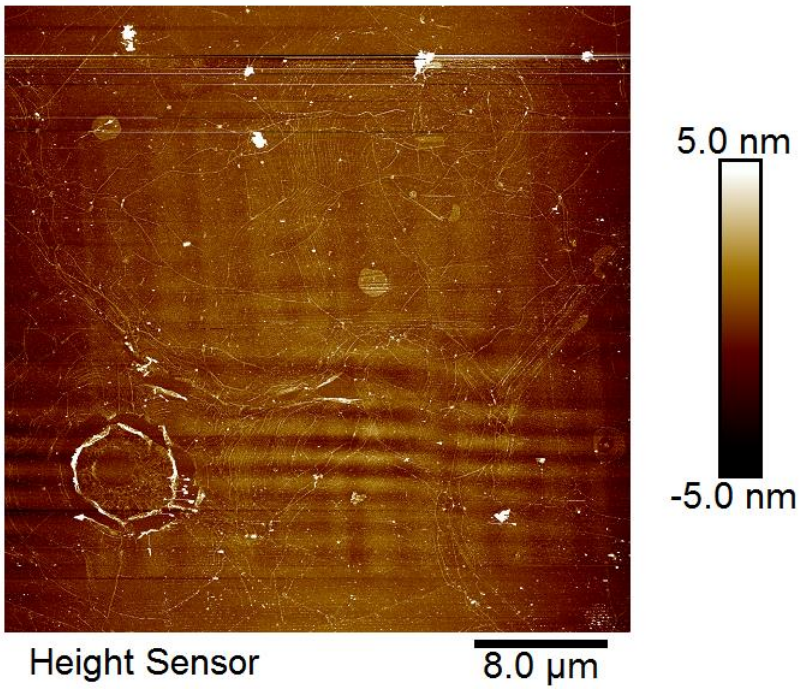

Figure 2. AFM image of oxidized area with irradiation time 0.2 s/spot.

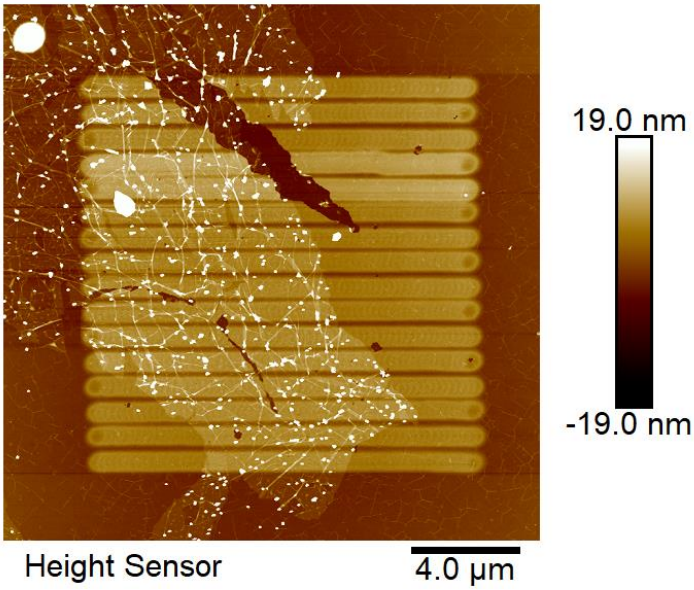

Figure 1. AFM image of square 2B line-grid after GNP deposition.

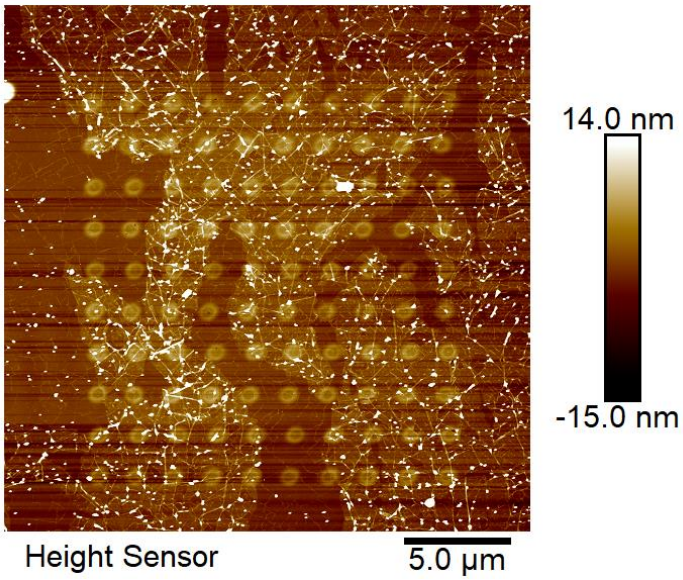

Figure 2. AFM image of square 2B 10 s blister matrix after GNP deposition.

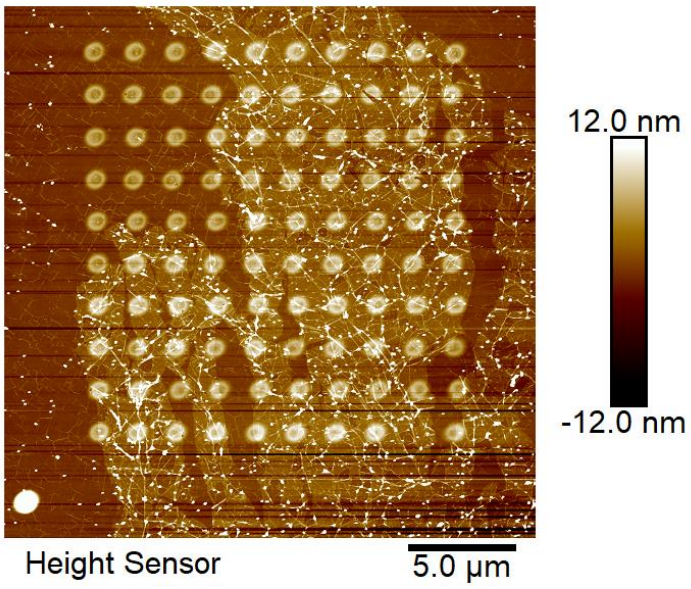

Figure 3. AFM image of square 3B 30 s blister matrix after GNP deposition.

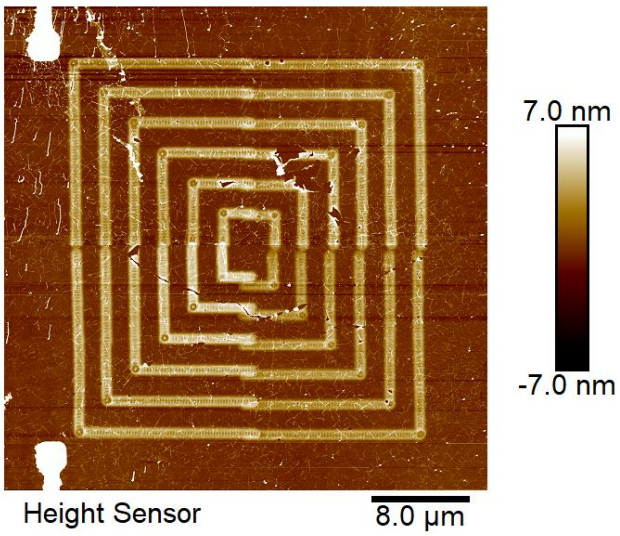

Figure 4. AFM image of square 3F frames after GNP deposition

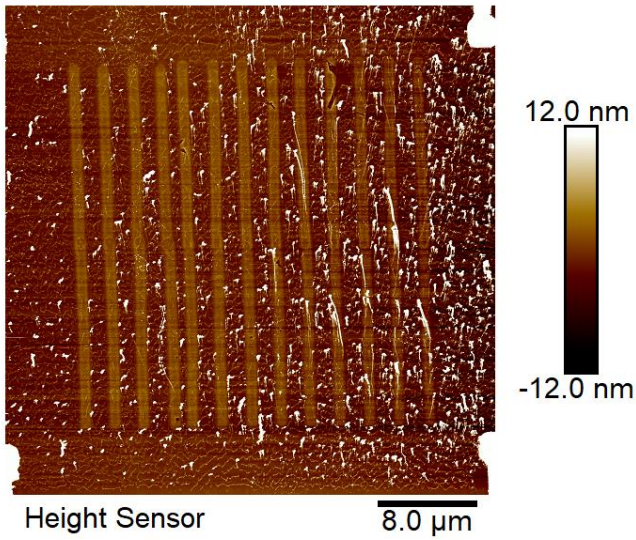

Figure 5. AFM image of square 4E frames after GNP deposition

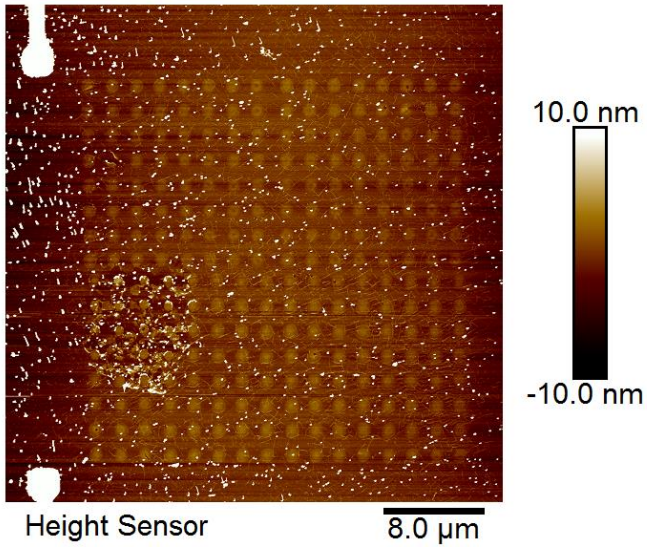

Figure 6. AFM image of square 3F blisters after GNP deposition.

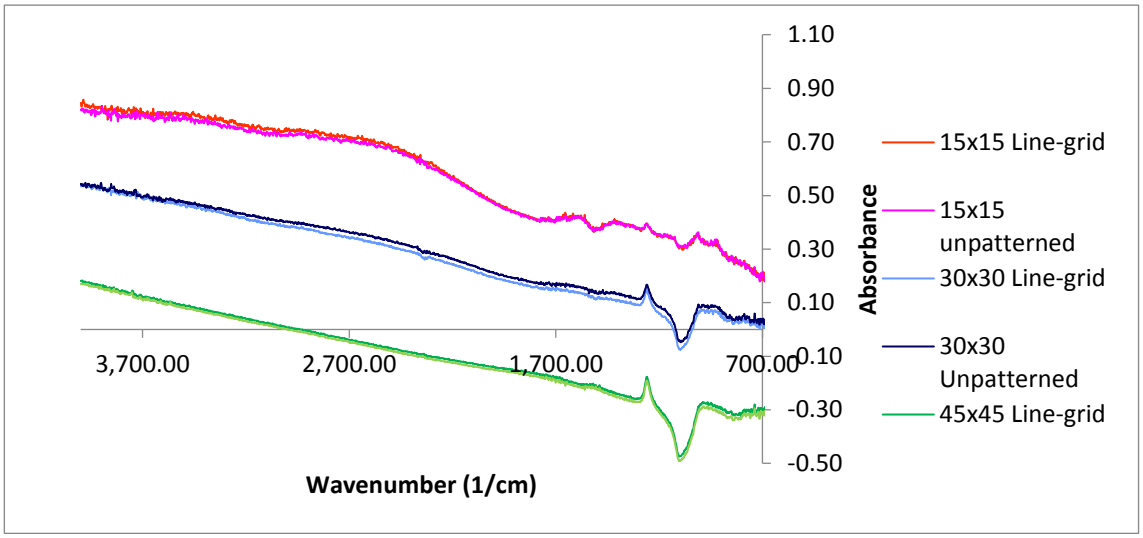

Figure 1. IR absorbance with different aperture sizes for line-grid and unpatterned area in square 2B.

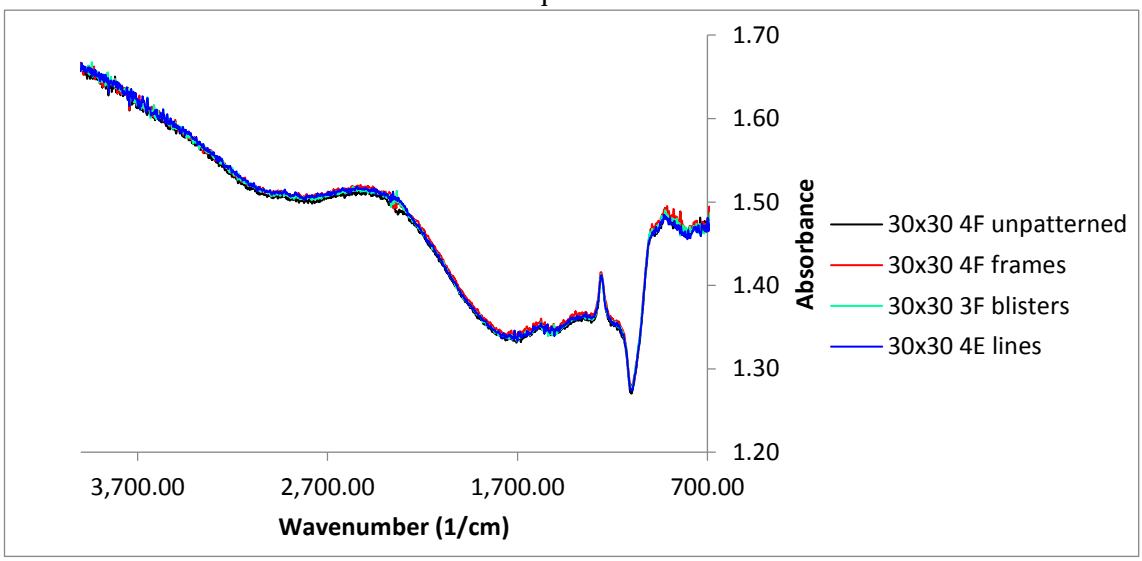

Figure 2. IR absorbance with aperture size 30x30 for patterns in squares 3F, 4E and 4F and for unpatterned area in square 4F.

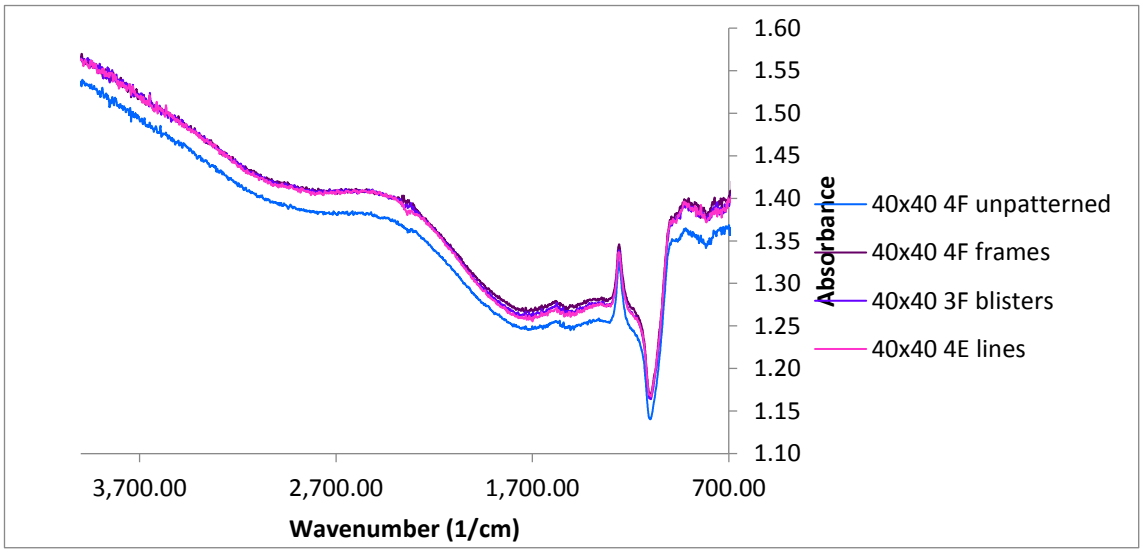

Figure 3. IR absorbance with aperture size 40x40 for patterns in squares 3F, 4E and 4F and for unpatterned area in square 4F.

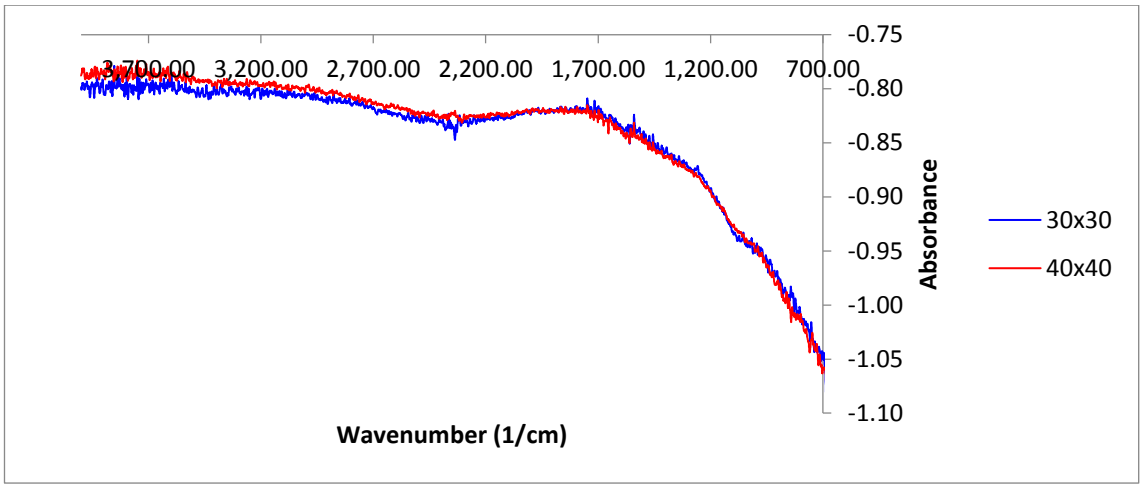

Figure 1. Subtraction of square 4E line-grid IR absorbance with aperture sizes 30x30 and 40x40 before GNP deposition from after GNP deposition ($Spectra_{after}$-$Spectra_{before}$).

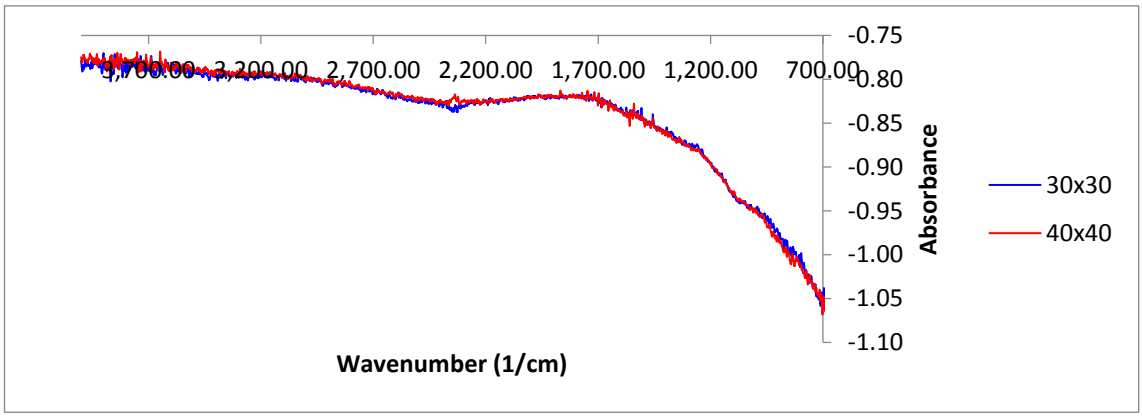

Figure 2. Subtraction of square 4E frames IR absorbance with aperture sizes 30x30 and 40x40 before GNP deposition from after GNP deposition ($Spectra_{after}$-$Spectra_{before}$).

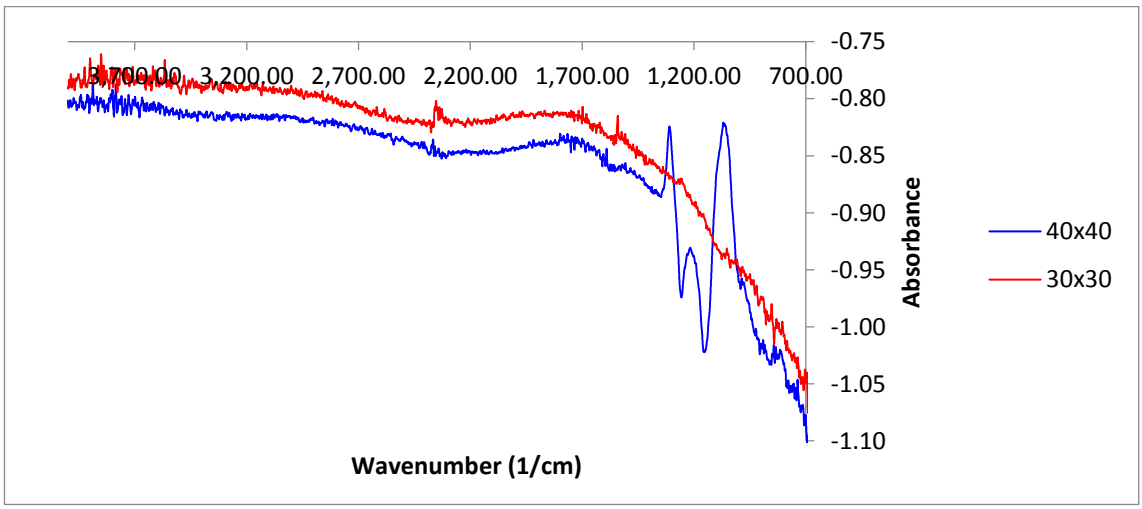

Figure 3. Subtraction of square 3F blister matrix IR absorbance with aperture sizes 30x30 and 40x40 before GNP deposition from after GNP deposition ($Spectra_{after}$-$Spectra_{before}$).

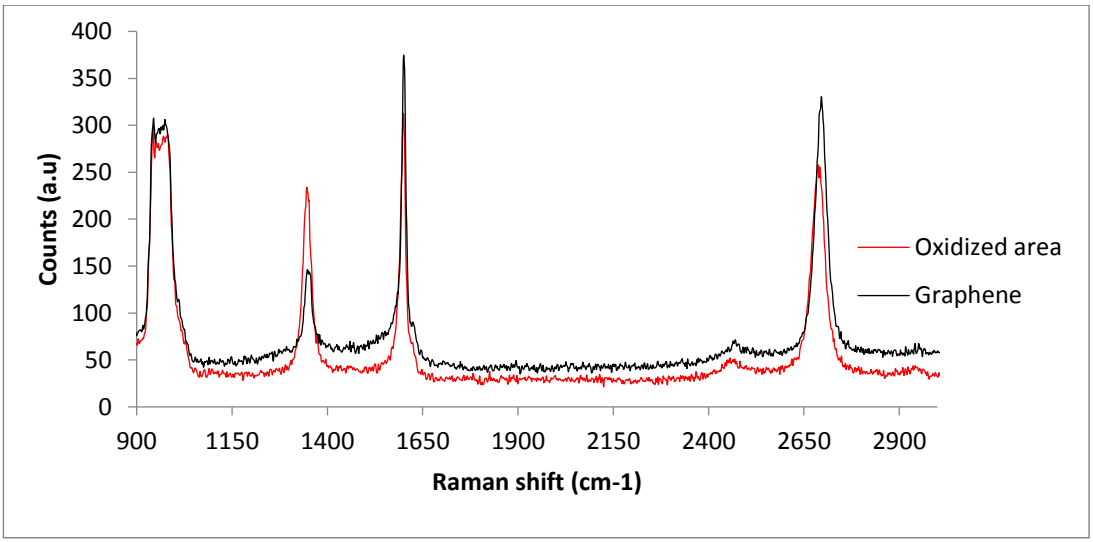

Figure 1. Raman spectra of oxidized and unoxidized areas in 0.3 s/spot pattern.

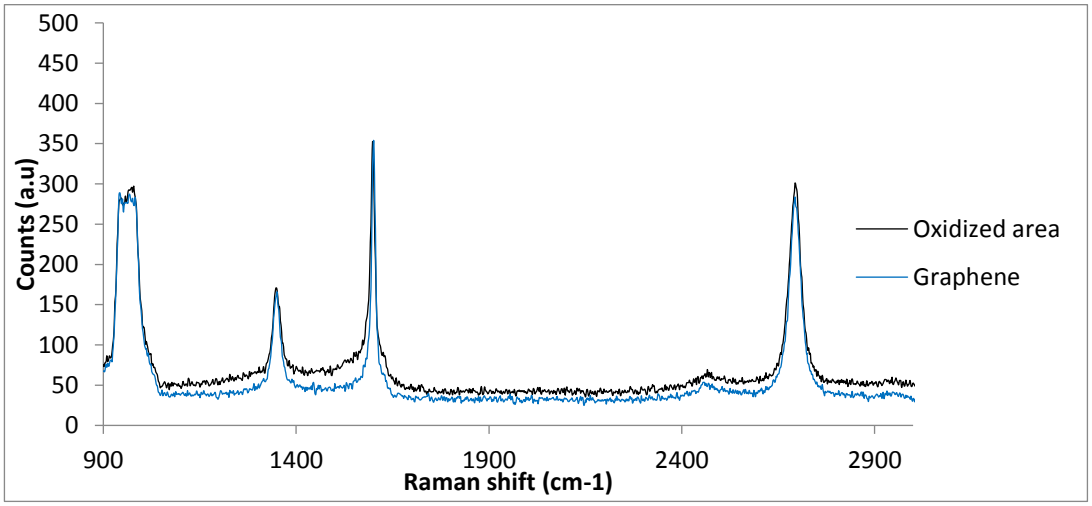

Figure 2. Raman spectra of oxidized and unoxidized areas in 0.2 s/spot pattern.

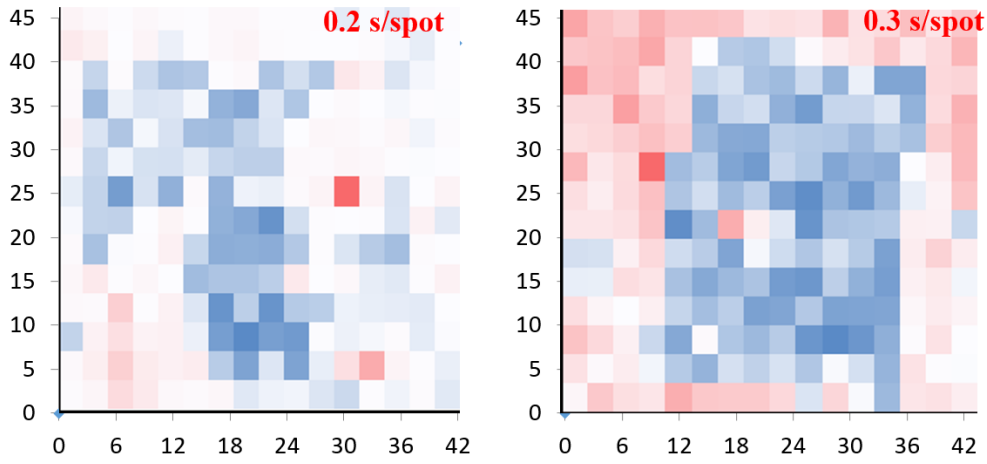

Figure 3. Heat maps of Raman spectra integrated over D-band for each pixel in the measured area.